Chair of Nonferrous Metallurgy

Doctoral Thesis

Al-Mg-Si-Fe crossover alloys – Control of microstructure and mechanical properties through Fe-rich primary phases

Dipl.-Ing. Bernhard Trink, BSc

October 2024

AFFIDAVIT

I declare on oath that I wrote this thesis independently, did not use any sources and aids other than those specified, have fully and truthfully reported the use of generative methods and models of artificial intelligence, and did not otherwise use any other unauthorized aids.

I declare that I have read, understood and complied with the "Preamble on Integrity in Academic Study, Teaching, and Research Operations" of the Montanuniversität Leoben.

Furthermore, I declare that the electronic and printed versions of the submitted thesis are identical in form and content.

Date 08.Okt.2024

Bernhard Trink

(The original signature is kept at the university)

ACKNOWLEDGEMENTS

First and foremost, I would like to express my sincere gratitude to Univ.-Prof. Dipl.-Ing. Dr.mont. Stefan Pogatscher and Univ.-Prof. Dipl.-Ing. Dr.mont. Helmut Antrekowitsch for the great opportunity to conduct my doctoral research within the Christian Doppler Laboratory for Advanced Aluminum Alloys at the Chair of Nonferrous Metallurgy. I am deeply thankful for their mentorship and the many opportunities they provided, allowing me to gain invaluable experience in this field of research.

Furthermore, I am profoundly grateful for the extensive scientific support I received from Univ.-Prof. Dipl.-Ing. Dr. mont. Peter Uggowitzer and Dipl.-Ing. Dr. mont. Irmgard Weißensteiner with their consistent willingness to help, and for all the inspiring discussions we had. I would also like to thank my industrial advisor at AMAG Rolling GmbH, Dr. Katharina Strobel, for giving me a good insight into industrial processing.

Many thanks to all my colleagues for their friendship and assistance. I really appreciate my work at the Chair of Nonferrous Metallurgy and will look back fondly on my time as a Ph.D. student.

I would like to extend my heartfelt gratitude to my family, especially my mother Roswitha, for giving me the initial opportunity to pursue my academic career. I am very thankful to my wife, Martha, for her unwavering support and tireless encouragement.

ABSTRACT

Over the past few decades, the rapid advancement of the traffic and transportation sector has led to significant changes in the global climate due to increasing CO_2 emissions. Despite heightened political awareness and growing economic imperatives driving research and development in this sector, current technologies remain insufficient to fully address this challenge.

An important way to increase energy savings and reduce harmful emissions is to optimize vehicle design, which is closely linked to the choice of materials. The use of lightweight materials such as aluminum alloys to replace high-density steel is a well-established strategy for reducing greenhouse gas emissions. Unfortunately, there are many challenges associated with the production of aluminum, such as the need for enormous amounts of electrical energy, which is again linked to greenhouse gas emissions, and the formation of tons of residue (red mud), which is a serious environmental concern.

One way to address this problem is through recycling, which significantly reduces the amount of energy required by remelting scrap without producing red mud as a by-product. However, recycling of Al-alloys faces challenges due to the diverse composition of aluminum scrap. During the recycling process, impurities are introduced into the alloys, which can have a significant impact on their mechanical properties. Iron, considered a tramp element, is particularly undesirable in aluminum alloys because it is responsible for the deterioration of ductility and forming properties. In Al alloys it tends to form coarse and brittle intermetallic phases, which can cause internal damage during forming and lead to premature material failure.

This research focuses on the development of a highly Fe-tolerant alloy concept based on Al-Mg-Si alloys capable of providing high ductility and formability. To avoid the negative effects of Fe and to effectively utilize the otherwise detrimental Fe-rich primary phases during microstructure evolution, a crossover approach is being pursued. Crossovers combine the beneficial material properties of existing aluminum alloys.

By applying the crossover approach, the age-hardening capability of the 6xxx series and the microstructure control using primary phases in Fe-rich 8xxx (foil stock) alloys have been merged. By morphologically transforming the as-cast structure of Fe-rich primary phases into fine particles during thermomechanical treatment, significant grain refinement and uniform texture were achieved. In addition, the high density of ~1 μm particles contributes to good ductility, increased strength and work hardening through the formation of additional geometrically necessary dislocations (GNDs). The overall concept has been validated even under industrial production conditions, but further research is needed to fully exploit the potential of the introduced Al-Mg-Si-Fe crossover alloys.

KURZFASSUNG

Die rasante Entwicklung des Verkehrs- und Transportsektors in den letzten Jahrzehnten hat durch den Anstieg der CO_2-Emissionen zu erheblichen Veränderungen des globalen Klimas geführt. Trotz des gestiegenen politischen Bewusstseins und der wachsenden wirtschaftlichen Notwendigkeit, die Forschung und Entwicklung in diesem Sektor voranzutreiben, reichen die derzeitigen Technologien nicht aus, um diese Herausforderung zu bewältigen.

Eine Möglichkeit zur Steigerung der Energieeinsparung, und damit zur Verringerung der Schadstoffemissionen, besteht in der Optimierung der Fahrzeugkonstruktion, die eng mit der Wahl der Werkstoffe verbunden ist. Die Substitution von schwerem Stahl durch leichte Werkstoffe wie Aluminiumlegierungen ist eine bewährte Strategie zur Verringerung der direkten Treibhausgasemissionen. Leider ist die Herstellung von Aluminium mit zahlreichen Problemen verbunden, wie z. B. dem enormen Bedarf an elektrischer Energie, der wiederum mit Treibhausgasemissionen verbunden ist, und der Bildung von tonnenweise Rückständen (Rotschlamm), die ein ernstes Umweltproblem darstellen.

Eine Lösung besteht im Recycling von Aluminiumschrott, das mit einem wesentlich geringeren Energieaufwand verbunden ist und bei dem kein Rotschlamm als Nebenprodukt anfällt. Das Recycling von Al-Legierungen ist jedoch aufgrund der unterschiedlichen Zusammensetzung von Al-Schrotten mit Schwierigkeiten konfrontiert. Beim Recycling werden Verunreinigungen in die Legierungen eingebracht, die die mechanischen Eigenschaften erheblich beeinflussen können. Insbesondere Eisen ist als Verunreinigung in Aluminiumlegierungen unerwünscht, da es in den meisten Fällen für die Verschlechterung der Duktilität und der Umformeigenschaften verantwortlich ist. Eisen in Al-Legierungen neigt zur Bildung grober und spröder intermetallischer Phasen, die zu vorzeitigem Werkstoffversagen bei der Umformung führen.

Diese Forschungsarbeit konzentriert sich auf die Entwicklung eines hoch Fe-toleranten Legierungskonzepts auf Basis von Al-Mg-Si-Legierungen mit hoher Duktilität und Umformbarkeit. Um die negativen Auswirkungen von Fe zu umgehen und Fe-reiche Primärphasen für die Gefügeentwicklung zu nutzen wird ein Crossover zwischen Al-Mg-Si-Legierungen (6xxx) und hoch Fe-haltigen Folienwerkstoffen (8xxx) angestrebt. Eine Veränderung der Gussphasenmorphologie hin zu feinen Partikeln führt in weiterer Folge zu Kornfeinung und schwach ausgeprägter Textur. Die hohe Dichte der ~1 µm großen Partikel verbessert Duktilität, Festigkeit und Kaltverfestigung. Das Konzept wurde unter industriellen Bedingungen validiert, jedoch sind weitere Forschungsarbeiten nötig, um das volle Potenzial auszuschöpfen.

TABLE OF CONTENT

1 INTRODUCTION

Worldwide production of aluminum (Al) is approximately 100 million tons per year, making it the world's second most produced metal [1,2]. Aluminum and its alloys are used in a wide variety of applications due to their excellent chemical-physical properties, including low density (2.7 g/cm^3), high corrosion resistance, formability, conductivity, and strength. Lightweighting by substituting high-density materials such as steel for low-density materials such as aluminum alloys is well established, particularly in the automotive sector. Lightweight design using aluminum alloys improves energy efficiency in transportation, packaging and construction, which in turn reduces the emission of greenhouse gases (GHG), responsible for global warming.

However, the primary production of aluminum presents several challenges, including enormous energy consumption (~13 Exajoule per year) [2], substantial GHG emissions (12-16.5 tons per ton of primary Al produced) [2], and the generation of residues such as red mud (~120 million tons per year) [3], which is stored in large landfills and can be considered environmentally critical due to its high basicity.

A viable solution to the issues associated with primary production is recycling. Recycling of aluminum, which involves remelting of Al-scrap, requires only a fraction (~5%) of the energy used in primary production. Currently, about one-third of the aluminum used is derived from recycled scrap [2]. By 2050, this recycling rate is expected to rise to 50%, further reducing aluminum's energy and carbon footprint, thus enhancing sustainability [2].

Given the diverse applications of aluminum alloys, they are categorized into various alloy groups to meet specific requirements. Consequently, post-consumer scrap from end-of-life products exhibits a wide range of compositions. Understanding the effects of impurities and effectively working with them to integrate recyclability into alloy design are crucial for developing highly recycling-tolerant alloys. Among the various elements, iron (Fe) poses a significant challenge due to its gradual accumulation during the recycling of aluminum scrap and its difficulty in removal through metallurgical processes [4]. The low solubility of Fe in aluminum solid solution leads to the formation of brittle intermetallic primary phases during casting, which in most cases adversely affect formability and mechanical properties [5]. Therefore, strict Fe-limits are set in most Al-systems. The aim of this thesis is to design a highly Fe-tolerant alloy concept based on Al-Mg-Si alloys, offering improved mechanical properties and high formability.

1.1 Concept and visualization

Commercial Al-Mg-Si (i.e. 6xxx) alloys currently account for approximately 60% of the aluminum-based materials market [6] and exhibit medium to high strength, high fracture toughness, good weldability and corrosion resistance, as well as excellent surface quality and bake hardening potential [7]. However, their stretch formability is limited due to their low strain hardening capability, which is significantly worse than that of Al-Mg (5xxx) alloys. Tuning 6xxx alloys for higher in use strength by increasing the Si content [8] or by adding additional alloying elements such as Zn [9] results in significantly impaired performance during forming. Another way to achieve higher strength and strain hardening properties in Al-alloys is to add age-hardening potential to 5xxx alloys via a crossover with 7xxx alloys, i.e. the addition of Zn and Cu [10]. Stemper et.al [10] have already been shown that crossovers between different alloy classes have great potential in terms of combining positive properties (e.g. good formability and high strength were seen for a crossover between 5xxx and 7xxx alloys). With this in mind, we sought a crossover between 6xxx alloys and the Fe-rich 8xxx series. Foil materials (i.e. 8xxx alloys [11]) typically have a very high Fe content, which leads to the formation of brittle primary intermetallic phases, but exhibit good elongation and forming properties. The iron helps to reduce grain size and to maintain formability at low foil thickness.

Figure 1-1 provides an overview of the Al-Mg-Si-Fe crossover alloy concept. By intentionally raising the Fe-content in 6xxx alloys, which conceptually mimics high scrap content, and by applying a thermomechanical treatment, the former coarse Fe-rich phases are modified to form finely dispersed particles. These particles contribute significantly to microstructural control (grain refinement) and improved mechanical properties, such as increased strength and strain hardening (formation of additional geometrically necessary dislocations), indicating improved stretch formability.

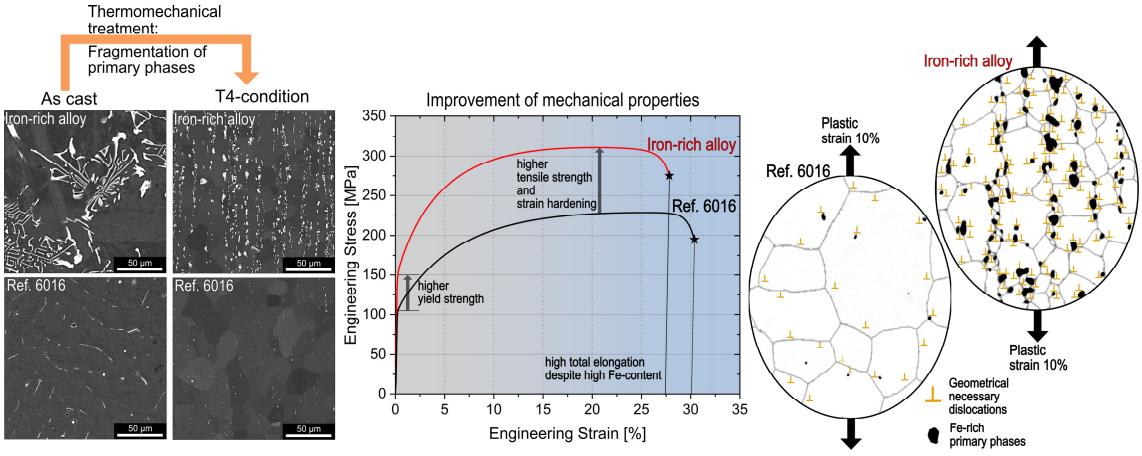

Figure 1-1: Visualization of the Al-Mg-Si-Fe crossover alloy concept[1]

[1] Note that this concept was also presented by the author in: B. Trink et al. (2023): Processing and microstructure–property relations of Al-Mg-Si-Fe crossover alloys, Acta Materialia 257 (2023) 119160.

1.2 Document structure

In order to successfully pursue the crossover approach between 6xxx and high-Fe 8xxx alloys introduced above requires detailed knowledge of the underlying principles and mechanisms of alloy and microstructure design summarized in section 2. This section includes the state-of-the-art research on Fe-rich primary phases and their control in morphology by alloying elements and processing parameters. The basis for the subsequent alloy design in section 3 is derived from the detailed information in section 2. Sections 4 to 6 present the key findings of this thesis, which have been published in peer-reviewed journals. Each section provides a brief description of the individual research results. Section 7 summarizes the scientific results obtained during the course of this thesis and discusses potential future applications and follow-up research.

2 STATE OF THE ART

The following chapter summarizes the essential knowledge of microstructure control, required to follow the proposed alloy design approach. Recrystallization mechanisms responsible for grain refinement are discussed in detail, with emphasis on the effect of Fe-rich particles. In addition, the effect of high iron content in Al alloys and possible techniques to modify the morphology of the resulting primary intermetallics are addressed.

2.1 Principles of microstructure control

The main aspects of microstructure design, i.e. recovery and recrystallisation, texture and texture effects, and the principles of heterostructured materials are discussed in detail below.

2.1.1 Recovery and recrystallisation mechanisms

During plastic deformation, a high density of dislocations is generated. In general, the cold worked state of a metal is not part of the thermodynamic equilibrium as it represents a high energy state. When a metal is annealed, its microstructure and material properties can be partially restored by a process called recovery, in which dislocations are annihilated and rearranged. This rearrangement of dislocations involves the formation of cells or subgrains, which play a major role during primary recrystallisation. The microstructural changes that occur during the recovery process are relatively homogeneous and usually do not affect the boundaries between the deformed grains. Similar recovery process occurs during deformation at high temperatures dynamically and is important in creep and hot working behavior. In contrast to recovery, recrystallisation entails the formations of new grains. [12,13]

Next to dislocations, grain boundaries are also thermodynamically unstable and further annealing results in grain growth, in which larger grains grow in the dispense of the smaller ones. Recovery, recrystallisation and grain growth may occur in two ways: i) As a discontinuous process heterogeneously distributed throughout the material, formally described in terms of nucleation and growth stages and ii) as a continuous process that occurs uniformly so that the microstructures evolve gradually. Therefore, six static annealing phenomena can be distinguished. Continuous phenomena include recovery by subgrain growth, continuous recrystallization, and normal grain growth. Discontinuous phenomena, in contrast, encompass discontinuous subgrain growth, primary recrystallization, and abnormal grain growth. [12]

Recovery and recrystallisation are competing mechanisms as both are driven by the stored energy of deformation i.e. dislocation density (total line-length of dislocations per unit volume). Once

recrystallization has occurred and the deformation substructure has been consumed, no further recovery can occur. Conversely, as recovery lowers the driving force for recrystallisation, a significant amount of prior recovery will in turn influence the nature and kinetics of recrystallisation. However, it should be noted that some recovery, i.e. the rearrangement of dislocations into cells and subgrains, is important for the nucleation of primary recrystallization. [12]

During the recovery process, the changes in the microstructure of a material are subtle and take place on a small scale. As already mentioned, recovery is the annihilation and rearrangement of dislocations, which is achieved by glide, climb and cross-slip of dislocations. The elastic stress fields of the dislocations in the lattice interact and the resulting forces depend on the Burgers vectors and the relative positions of the dislocations. Dislocations with opposite sign on the same glide plane, may annihilate by gliding towards each other. This mechanism can occur even at low temperatures, resulting in a reduction in dislocation density during deformation and facilitating dynamic recovery. Dislocations with opposite Burgers vector on different glide planes can annihilate by a combination of glide and climb. A similar configuration of screw dislocations may be annihilated by cross-slip. Climbing and cross-slip of dislocations require thermal activation and occurs at higher temperatures. It is important to note that in materials such as aluminum, cross-slip may occur at low temperatures due to the high stacking fault energy. Excess dislocations, which are not annihilated will arrange into lower energy configurations in the form of regular arrays or low angle grain boundaries. This is also known as polygonization. The energy of low angle grain boundaries increases with increasing misorientation and the energy per dislocation decreases with increasing misorientation. As recovery proceeds fewer, more highly misoriented boundaries form. In an alloy with a medium or high stacking fault energy, the dislocations of two or more Burgers vectors react to form networks and are typically arranged after deformation in the form of a three-dimensional cell structure. The cell walls consist of complex dislocation tangles. The irregularly shaped cell walls become more regular, forming low angle grain boundaries and the transition from cells to subgrains is complete. The stored energy of a recovered substructure is still much higher than that of a fully recrystallized one, and can be further reduced by subgrain growth. The coarsening of the substructure can occur due to subgrain boundary migration and subgrain rotation and coalescence. [12]

Unlike recovery, which progresses over time with no identifiable beginning or end to the process, recrystallization involves the incubation of recrystallization nuclei and the formation of new grains with subsequent growth to consume the deformed microstructure (migration and formation of high-angle grain boundaries). The driving pressure for recrystallization results from the reduction of stored deformation energy and is provided by the dislocation density. As a new grain grows into the deformed structure, there is also an opposing force derived from the curvature of the high-angle grain boundary of specific energy. Thus, a minimum amount of deformation is required to initiate recrystallization, and to provide the necessary driving force to sustain its growth. [12]

Three criteria must be met for the formation of a stable nuclei. Firstly, a critical nucleation radius must be achieved in order to be thermodynamically stable. Since the nucleation rate due to thermal fluctuation is too small to trigger recrystallization, it can be assumed that supercritical nuclei such as cells or subgrains are already present in the deformed structure. Furthermore, the grain boundary must have a defined direction of movement, which is caused by an inhomogeneous dislocation distribution or by individual larger sub-grains. The last condition to be mentioned is the mobility of the grain boundary surface, which only applies to high-angle grain boundaries. [13]

Recrystallization will begin at inhomogeneities within the deformed microstructure, such as in the vicinity of coarse particles and at existing high-angle grain boundaries. The generation of a recrystallisation nuclei is therefore always associated with a local rearrangement of dislocations - i.e. with recovery processes - which also explains the existence of the incubation period. Recovery and recrystallization compete for the common driving force, the reduction of dislocation density. [13]

The kinetics of primary recrystallization is determined by nucleation and growth, both of which are thermally activated and determine the resulting grain size. For a fine grain, the nucleation rate should be high and the growth rate of the nuclei should be low. As the degree of deformation increases, smaller grains are obtained because the nucleation rate increases more than the nucleus growth rate. A similar effect can be obtained by reducing the grain size prior to deformation or when setting a higher heating rate. When recrystallization occurs during hot working, the process is called dynamic. Dynamic recrystallization (DRX) is of great importance in hot forming processes because it allows the yield stress, and thus the necessary forming forces, to be kept low. In addition, the dynamically recrystallized grain size correlates with the yield stress – finer grains are obtained as the yield stress increases. [13]

The recrystallization behaviour in multiphase alloys is strongly influenced by particles. Coarse particles (around 1 μm) promote the nucleation of new grains due to the surrounding inhomogeneous deformation structure (i.e. increased dislocation density), while fine particles (~100 nm) hinder both the dislocation mobility (recovery) and the grain boundary movement (recrystallization). The interfacial energy is reduced when the grain boundary meets the particle surface. Should the grain boundary be torn away from the particles, it is necessary to reapply energy in order to create a new interface, which results in a force contrary to grain growth (Zener pinning force). Thus, with a sufficiently small spacing of fine particles, it is possible to preserve the deformed/recovered microstructure even at higher temperatures. The effectiveness of the Zener-Pinning force depends on particle size, the distribution of particles [14], the geometry (needles pin better than spheres as needles have a larger surface area for the same volume) and the type of the particle-matrix interface. If a large-angle grain boundary passes through a particle with a coherent interface, the particle loses its coherence to the matrix. However, as an incoherent interface has a higher interfacial energy than a coherent one, energy must be applied during this transformation, resulting in a back-driving force. Coherent particles therefore counteract grain growth more effectively than incoherent particles.

Another way in which coherent particles can react to a moving grain boundary is that they are cut by it and follow the change in orientation. [12]

For many industrial alloys, especially those with higher iron content, particle-stimulated nucleation (PSN) is a very important recrystallization mechanism. Unlike other recrystallisation mechanisms the nucleation sites during PSN are well defined areas in the microstructure and can be altered by alloying and processing. As illustrated in Figure 2-1, particle-stimulated nucleation near large particles (~ 1 μm) originates at a pre-existing subgrain within the deformation zone in close proximity to these particles, but not necessarily at the particle surface. It occurs by rapid sub-boundary migration and as a subgrain grows, it increases its misorientation with neighboring subgrains. After a certain level this misorientation has reached that of a high angle grain boundary (e.g. 10–15°), which represents a recrystallisation nuclei. When the deformation zone is consumed, the newly formed grain may stop growing due to adjacent grains. The dislocation density or misorientation gradient within the deformation zone, together with the particle size and interparticle spacing, determines the formation of new high-angle grain boundaries via PSN and final grain size. The orientations of PSN-generated grains will be different from those produced by other recrystallization mechanisms (discussed in section 2.1.2), allowing texture control through large particles. [12]

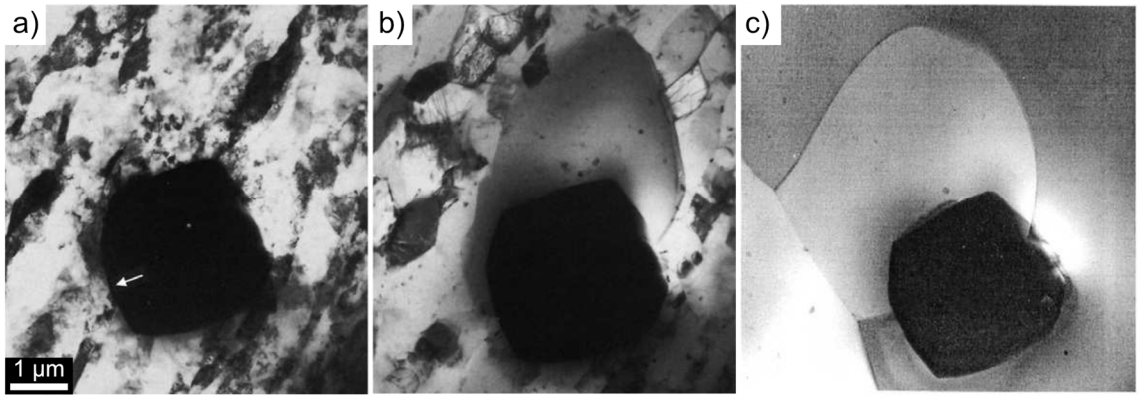

Figure 2-1: In-situ annealing sequence of Al-Si: Very small subgrains can be seen in the deformation zone above the particle. a) Recrystallization starts in the arrowed region of the deformation zone near the particle, b) the new grain has consumed the deformation zone, c) further grain growth is prevented by other grains that originated elsewhere. Adapted from [12]

Solutes usually hinder boundary migration and recrystallisation. The impact of solutes on recrystallization behavior varies depending on the specific solvent/solute combination. Iron, a highly effective solute in aluminum, can raise the recrystallization temperature by about 100°C even at very low concentrations. [12]

2.1.2 Texture components

In general, crystallographic texture is defined as the distribution of grain orientations in a polycrystal. Certain preferred orientations of the individual crystals are formed by hot or cold deformation, as well as during subsequent annealing processes in which the dislocation-rich material recrystallizes. This may lead to plastic anisotropy and influences the material properties.

Rolling of aluminum generate different zones with different dislocation densities. In the middle section of the sheet, the deformation textures Brass, S and Copper are usually formed, which together create the β-fiber. These texture components are highly unstable to heat treatments and transform during recrystallization. In the outer section of the sheet (up to about a quarter of the thickness), also known as the shear deformation zone, the texture components rotated cube and {111} <uvw> are increasingly formed, which show a slightly higher thermal stability. Cube and Goss are further texture components, which are described as metastable during deformation and usually dominate the recrystallization texture. Cold and hot rolling induces different texture components. In addition, an increase in temperature during the rolling process increases the probability of dynamic recrystallization, whereby a large proportion of the rolling texture components can be transformed. Rolling parameters and geometry are important factors influencing the final texture. [15]

When recrystallization occurs, the initial texture is renewed, as the distribution of grain orientations changes. Locations of nucleation for new grains in heavily deformed aluminum alloys are grain boundaries, cube bands, shear bands and the deformation zones around large particles (PSN). PSN typically leads to a rather weak recrystallization texture, with a certain preference for the P orientation {011}<122> and a characteristic rotation of the cube orientation by 20-25 ° around the sheet normal direction in the {001}<310> direction. [16]

Metals with a high stacking fault energy, such as aluminum, often form a cube recrystallization texture. Cube-oriented nuclei arise from band-shaped structures that are already present in the deformed microstructure, the so-called cube bands. These cube bands are either transition bands that have formed by splitting unstable orientations during the previous deformation, or deformed grains that have retained their cube orientation. During subsequent growth, grains with an exact cube orientation prevail, as these have favorable growth conditions due to their high symmetry. [16]

Heavy cold rolling of coarse-grained aluminum, or aluminum alloys with a high content of dissolved copper or magnesium, can lead to the formation of shear bands. If such a material recrystallizes after large degrees of deformation, these shear bands are suitable nucleation sites due to their strong local lattice rotations and local stresses. Recrystallisation at shear bands leads to the formation of two new orientations, the Goss orientation {011}<100> and the Q orientation {013}<231>. During nucleus growth, both Q and Goss-oriented grains are preferred due to a 40 ° <111> orientation relationship to the rolling orientation. Based on the preferred type of nucleation, nuclei form in certain orientations. These recrystallization nuclei then grow in different directions, whereby those that have

favorable growth conditions dominate. An example of this is the grain boundary orientation 40 ° <111>, which enables fast growth of the recrystallization grains. [16]

The cube component {001}<100> emerges from the cube bands and has a high grain boundary mobility, which favors its growth. The exact 40 ° <111> relationship to the S component leads to rapid growth of cube nuclei in neighboring S-oriented grains due to the extremely favorable growth conditions. As the cube component tends to form bands, it is responsible for mostly negative anisotropic effects in aluminum alloys. [17–19]

The R component {124}<211> is formed via nucleation at high angle grain boundaries. It also has a favored orientation relationship to the rolling texture, especially to the symmetrically equivalent S-component. The Goss {011}<100> and Q components {013}<231> form preferentially on shear bands. [16]

The P component {011}<122> and the CubeND component {001}<310> are mainly formed by the effect of particle stimulated nucleation (PSN) at large primary and secondary phases (around 1 µm) [20]. The nucleation at coarse particles leads to a strong weakening of the other recrystallization texture components. [16,21]

2.1.3 Texture effects

The position and orientation of grains have a significant influence on material properties. In particular, the presence of certain texture components significantly changes the forming behavior. An undesirable surface effect, known as roping, leads to roughening of the surface. The surface quality deteriorates to such an extent that the resulting waviness is visible after painting. Roping is based on the banding of texture components (visualized in Figure 2-2) in the rolling direction (RD) and leads to the formation of a roughness profile during deformation in the transverse direction. [22–24]

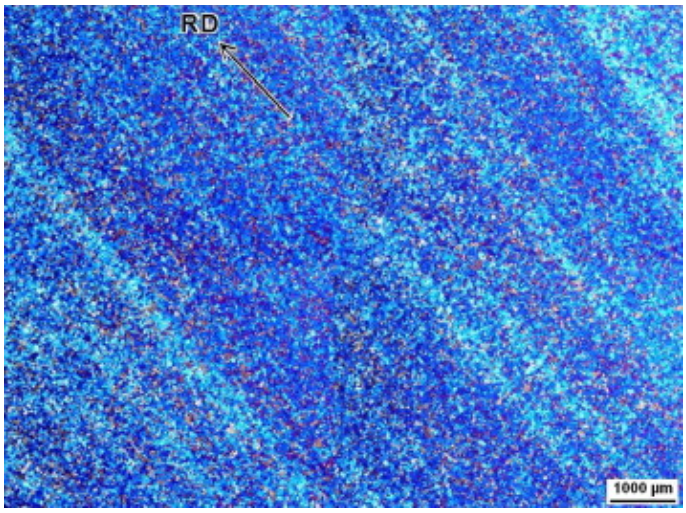

Figure 2-2: Microstructure of an AA 6016 sheet (T4) after anodic oxidation with a strong tendency to roping due to band formation in the rolling direction [25]

By reducing or eliminating the banding of texture components, inhomogeneous flow behavior and roping can be avoided. This can be achieved through alloy design and heat treatments. By alloying with iron, which subsequently forms large phases, the formation of CubeND and P texture components can reduce cube banding and suppress roping by PSN. Thus, surface quality can be improved by favoring PSN in Al-Mg-Si alloys for automotive body applications [26]. However, if Zener drag (small particles) dominates over particle-stimulated nucleation (large particles), banding is to be expected. The size, density and distribution of phases are always critical for the generation of a certain microstructure. Intermediate annealing (between two cold rolling steps) also ensures that cube bands are interrupted, which improves the surface quality of the final sheet material. Therefore, roping can be effectively suppressed by heat treatments. Fast heating as well as a high end-temperature during annealing counteracts the formation Cube-Bands and leads to finer recrystallized grains, as the nucleation rate of new grains during recrystallisation rises. [12,21,27–29]

The individual texture components have different material flow parameters due to differences in the favored slip directions in the crystal lattice relative to the applied stress. The dimensionless R-value is a measure of the anisotropy of plastic deformation. It can be determined from uniaxial tensile tests and describes the ratio of the change in width relative to the change in thickness (Eq. 2-1).

$$R = \frac{\ln\left(\frac{b_1}{b_0}\right)}{\ln\left(\frac{s_1}{s_0}\right)} \qquad \text{(Eq. 2-1)}$$

b_1 Final width [m]

b_0 Initial width [m]

s_1 Final thickness [m]

s_0 Initial thickness [m]

The average R-value (R_{mean}) is used to characterize the flow differences in the various directions (starting from the rolling direction) and is calculated using Eq.2-2. This value describes the flow behavior during deformation and is an important parameter for deep drawing operations.

$$R_{mean} = \frac{R_0 + 2R_{45} + R_{90}}{4} \qquad \text{(Eq. 2-2)}$$

R_0 R-value in 0° to RD [-]

R_{45} R-value in 45° to RD [-]

R_{90} R-value in 90° to RD [-]

A mean anisotropy $R_{mean} < 1$ corresponds to increased flow from the thickness of the material, while a value > 1 corresponds to flow from the width of the sheet. If R_{mean} is exactly 1, isotropic deformation behavior (uniform flow across width and thickness) is expected.

The planar anisotropy ΔR describes the distribution of the R-values across the sheet plane and is calculated by Eq. 2-3. In general, high R_{mean} and low Δ*R* values are advantageous for the deep drawing process. If Δ*R* = 0 there is no tendency for earing, while the tendency to earing increases with higher values [30].

$$\Delta R = \frac{R_0 - 2R_{45} + R_{90}}{2} \qquad \text{(Eq. 2-3)}$$

2.1.4 Heterostructured alloys

Metals that are characterized by high strength usually have low ductility. However, materials with a heterogeneous microstructure can partially avoid the strength-ductility trade-off and exhibit unique mechanical properties. A heterostructure is achieved by a non-uniform microstructure consisting of soft and hard zones. In our case, the hard zone represents an iron-rich primary phase particle, while the soft zone is the aluminum matrix. Unlike a conventional composite (strong but brittle reinforcements in a soft metallic matrix), both the hard and soft zones are plastically deformable to allow effective hetero-deformation induced (HDI) strain hardening for higher ductility. The main reason for the improved mechanical properties is the activation of HDI strengthening and HDI strain hardening due to formation and accumulation of geometrically necessary dislocations (GNDs). HDI strengthening increases the yield strength, while HDI strain hardening is defined as the rate of increase in HDI stress with applied strain, which acts to improve ductility. GNDs represent an additional reservoir for dislocations, which is required to compensate for the lattice curvature that occurs during non-uniform plastic deformation of a heterogeneous material. Figure 4 schematically shows the accumulation of GNDs. As the applied shear stress (τ_a) increases, a Frank-Read dislocation source (the red dot in Figure 4) is first activated in the soft zone to emit dislocations with the same Burgers vector. These dislocations slide on a slip plane towards the zone boundary and pile up against it. Since these dislocations have the same Burgers vector, they will distort and change the orientation of the slip plane. The elastic fields of GNDs superimpose and generate a long-range stress in the soft zone, which acts in the opposite direction to the applied stress (back stress) and strengthens the soft zone against further deformation. The back stress offsets the applied stress so that subsequent GNDs cannot slip forward or be emitted from the Frank-Read source. Plastic strain is generated by the movement of dislocations. The accumulation of GNDs does not result in plastic deformation at the zone boundary, as no dislocation reaches it. whereas the point at the dislocation source should exhibit the highest plastic strain. An accumulation of GNDs is therefore accompanied by the formation of a strain and stress gradient (Figure 2-3 b and c). [31]

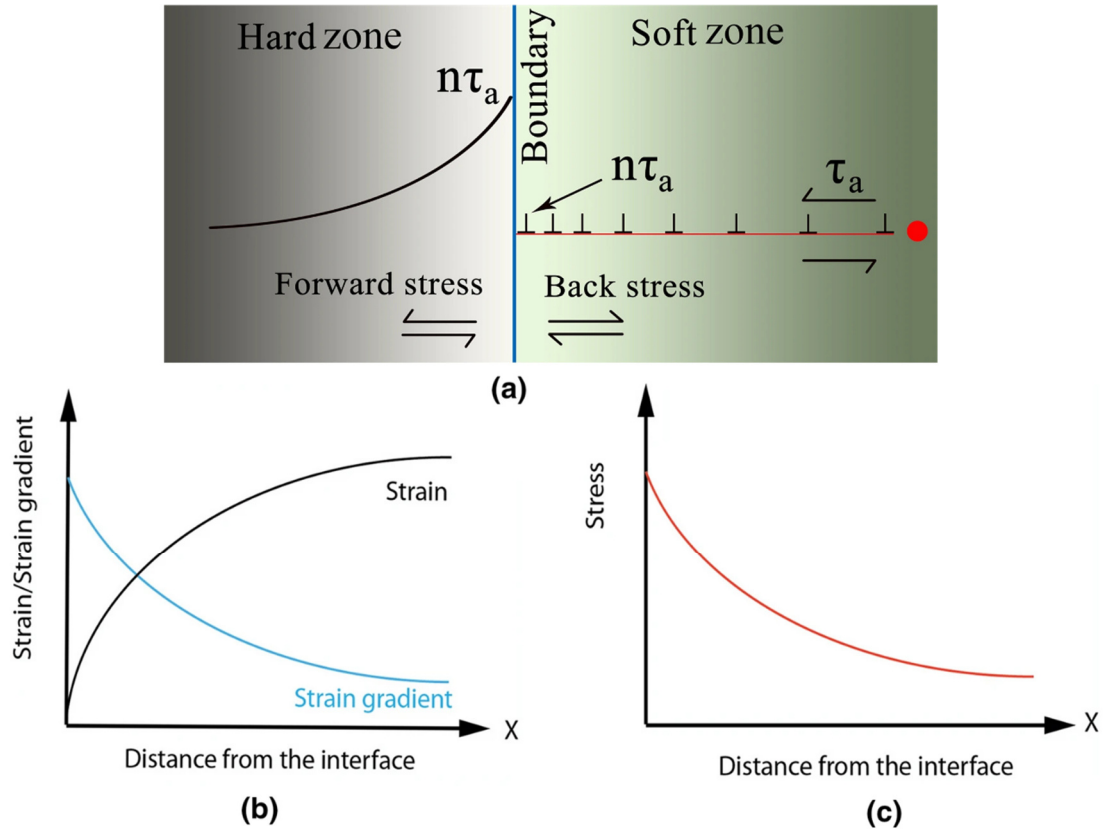

Figure 2-3: (a) Schematic representation of the accumulation of geometrically necessary dislocations (GNDs). The GND piling up generates back stress in the soft zone and forward stress in the hard zone. (b) The plastic strain gradient in the soft zone due to the GND accumulation, assuming these GNDs are from a Frank-Read dislocations source marked as the red dot. (c) Schematic back stress profile in the soft zone. Adapted from [31].

The accumulation of GNDs in Figure 2-3 shows an idealized scenario. The situation in real heterostructured materials can be much more complex. For example, GNDs can also migrate into zone boundaries as well as form small angle grain boundaries, which would not lead to extensive back stress in the soft zone. The actual interactions of the GND pile-up at a zone boundary have not yet been precisely clarified. Theoretically, when the GNDs pile up at a zone boundary, they can be stopped at the boundary, pushed into the boundary, transferred across the boundary, or reflected off the boundary, as well as cross-slip to escape piling up. All these scenarios have an impact on the effectiveness of the generated back stress. [31]

As stated earlier, composites or two-phase materials utilize the aforementioned principle. Composites can be produced by injecting intermetallic particles (Al_3Fe) into the Al melt. These particle reinforced Al-based composites have significant potential for advanced structural applications due to their high stiffness and strength at elevated temperatures [32,33].

2.2 Al-Mg-Si (6xxx) alloys

The Al-Mg-Si system is the basis of many age-hardenable wrought alloys used in a wide range of lightweight applications, mainly as rolled, drawn and extruded products. Overall, this group of aluminum alloys is characterized by medium to high strength, high fracture toughness, good weldability, corrosion resistance and formability. Figure 2-4 provides an overview of the most important Al-Mg-Si alloys as a function of the average Si and Mg content. [7]

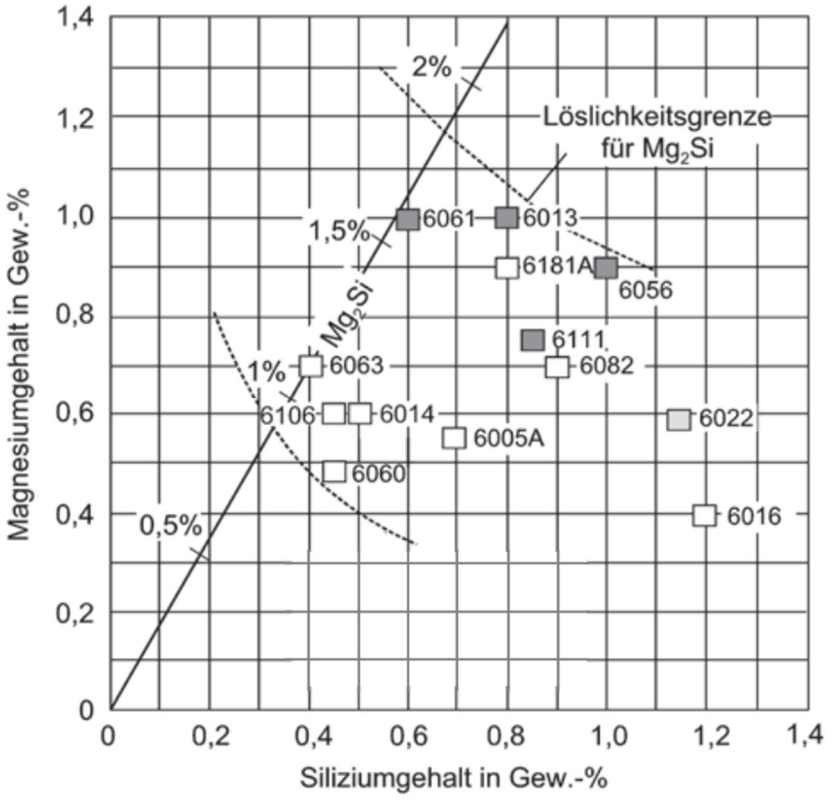

Figure 2-4: Overview of the most important Al-Mg-Si alloys as a function of the average Si and Mg content (white squares indicate Cu-free alloys and dark squares indicate Cu-rich alloys). The position of the average nominal alloy composition compared to the stoichiometric composition Mg_2Si gives the nominal silicon excess. Adapted from [7].

Al-Mg-Si wrought alloys contain around 1 to 2 wt.% of magnesium and silicon. Under equilibrium conditions, high-purity Al-Mg-Si alloys consist of two phases (Al solid solution and Mg_2Si). The intermetallic Mg_2Si phase has a relatively high melting temperature of 1085 °C, a high enthalpy of formation of 6.4 kcal/mol and a maximum solubility of 1.9 wt.% at 583.5 °C. The high melting temperature of the Mg_2Si intermetallic phase indicates a strong bond between Mg and Si, and hence thermal stability of Si/Mg clusters. Metastable precursor phases are responsible for precipitation hardening. [7]

Silicon is commonly added above the stoichiometric composition of Mg_2Si. An excess of Si has little effect on the solubility of Mg_2Si, while an excess of Mg will significantly reduce the solubility of either Si or Mg_2Si [5]. Si-surplus alloys benefit from increased strength after artificial aging more than an

equal percentage excess of Mg or an equal increase in Mg_2Si content [7]. Silicon therefore promotes the formation of fine clusters of higher volume fraction and accelerates the kinetics of natural and artificial aging. With increasing Si content (decreasing Mg/Si ratio), the work-hardening capacity of Al-Mg-Si alloys increases, which is accompanied by an improvement in stretch formability [34]. The decrease of Mg/Si ratio also raises the strain rate sensitivity of the flow stress [34].

The addition of small amounts of copper (Cu) causes a strong increase in strength during artificial ageing, as the metastable precursor phases of the equilibrium Q ($Al_4Mg_8Si_7Cu_2$) phase are additionally formed, which effectively hinder dislocation movement. The strength increase due to Cu during artificial ageing is attributed to a denser dispersion of the needle-shaped, partially coherent metastable Mg_2Si (β"-phase) and the rod-shaped, partially coherent metastable Q'-phase [7]. Additionally, a Cu-content of ~0.3 wt.% slightly reduces the strain rate sensitivity, particularly in alloys with a high Mg/Si ratio, and increases stretch formability due to significant increase in the dislocation storage rate i.e. work hardening rate [34].

Al-Mg-Si alloys contain iron concentrations of 0.05 to 0.5 wt.%, which is considered a tramp element [7]. Even small amounts of iron can contribute significantly to the microstructure evolution through the formation of primary and secondary phases, which will be discussed in sections 2.4 and 2.5.

Manganese and chromium are elements used in Al-Mg-Si alloys as "Fe-correctors" (see section 2.6) and in order to form small thermally stable precipitates (20-200 nm in diameter [35–37]) during homogenization treatment to control recrystallization and final texture [38–40]. Manganese is typically added in quantities of 0.2 to 1.0 wt.% and chromium from 0.05-0.35 wt.% [7]. During ingot homogenization, iron and manganese together produce a much finer and more numerous dispersion than Mn alone, while chromium is particularly effective in combination with a minimum Fe content [7]. The strength benefit of such disperoids is moderate and may even be negative if premature heterogeneous precipitation of supersaturated alloying elements (Si, Mg) occurs on incoherent particles at slow cooling rates after solution annealing. On the other hand, during subsequent slow quenching conditions, dispersoids can bind excess Si and Mg_2Si that would otherwise preferentially precipitate as coarser Si and Mg_2Si particles at grain boundaries, contributing to the low-energy, partially intergranular fracture behavior [7]. Finely dispersed particles also inhibit planar dislocation slip and promote dislocation motion through increased cross-slip. Activation of additional slip systems provides a more homogeneous slip distribution, which improves ductility and reduces or completely prevents intergranular fracture [13].

2.3 Foil stock (1xxx and 8xxx) alloys

Foil materials, i.e. 1xxx and 8xxx alloys, are widely used as packaging materials for goods such as food, dairy products and pharmaceuticals due to their impermeability and barrier properties combined with their high corrosion resistance and high formability. Commercial purity (1xxx) Al-foil

products consist of more than 99 wt.% Al with additions of up to 0.8 wt.% Fe and 0.1-0.3 wt.% Si, which show a rather low strength [11]. Higher strength can be achieved by increasing the Fe content, for example in the 8xxx series alloys such as AA 8079, which contains 0.7-1.3 wt.% iron. [11]

There are two common ways in foil production: Either from a conventional direct chill cast ingot which is hot rolled to a strip of about 2–5 mm, or from a 6–7 mm thick sheet produced by continuous casting routes [11,41,42]. Further process steps include cold rolling to an intermediate gauge, followed by intermediate annealing and cold rolling to the final foil thickness. Closed-gap rolling is used to produce thin foils below 100 μm. Most foil products are supplied in the soft annealed condition. The final annealing process recrystallizes the material and removes the rolling lubricant from the foil. [11]

Grain size in foil material has a relatively small effect on strength, but largely impact ductility (higher ductility is associated with smaller grain size) [11]. As described in Section 2.1.1, the final grain size is influenced by the size, density and distribution of the primary phases and dispersoids, as well as the solute concentrations of the alloying elements (Fe). The phases found in foil alloys (i.e. in the Al-Fe and Al-Fe-Si systems) are described in detail in section 2.4. Since the only alloying elements found in foil materials are Fe and small amounts of Si, it is essential to modify the as-cast phases through process steps such as annealing and rolling to effectively utilize the PSN effect, which is discussed in Section 2.7.

2.4 Iron-rich phases in Al-alloys

Since the solubility of iron in Al solid solution is less than 0.05 wt.% at the equilibrium condition at room temperature, almost the entire Fe content is precipitated in the form of primary or secondary phases. Depending on the respective material system and the formation conditions, different phases can be expected. This chapter deals with the formation of stable and metastable Fe-rich phases in the Al-Fe and Al-Si-Fe system.

The binary Al-Fe phase diagram shows the formation of the thermodynamically stable $Al_{13}Fe_4$ (also donated as Al_3Fe or θ-phase), which forms a eutectic with Al at ~655 °C and ~1.8 wt% Fe. Commonly this phase is reported to grow as relatively large angular needle-shaped precipitates during casting, reducing formability and fatigue resistance [43]. Large undercooling is required to nucleate and/or grow the Al-$Al_{13}Fe_4$ eutectic. Non-equilibrium solidification conditions, which are relevant in industrial casting operations (higher cooling rates), lead to the formation of thermodynamically metastable Al-Fe eutectic phases. These phases, which require lower undercooling for nucleation and growth, are summarized in Table 2-1 [43]. Figure 2-5 shows the composition ranges of some of the metastable Al-Fe and Al-Fe-Si eutectics.

Table 2-1: Al-Fe phases identified in the Al-Fe system.

Fe-rich intermetallic phase	**Crystal structure**	**Reference**
θ-$Al_{13}Fe_4$ or θ-Al_3Fe	c-Centered monoclinic	[44,45]
Al_6Fe	c-Centered orthorhombic	[46,47]
Al_xFe (x ≈ 4.5-5.0)	-	[43,48]
Al_mFe (m ≈ 4.0-4.4)	Body centered tetragonal	[43,48,49]
Al_9Fe_2	Monoclinic	[43,50]
Al_pFe (p ≈ 4.5)	Body centered cubic	[43,51]

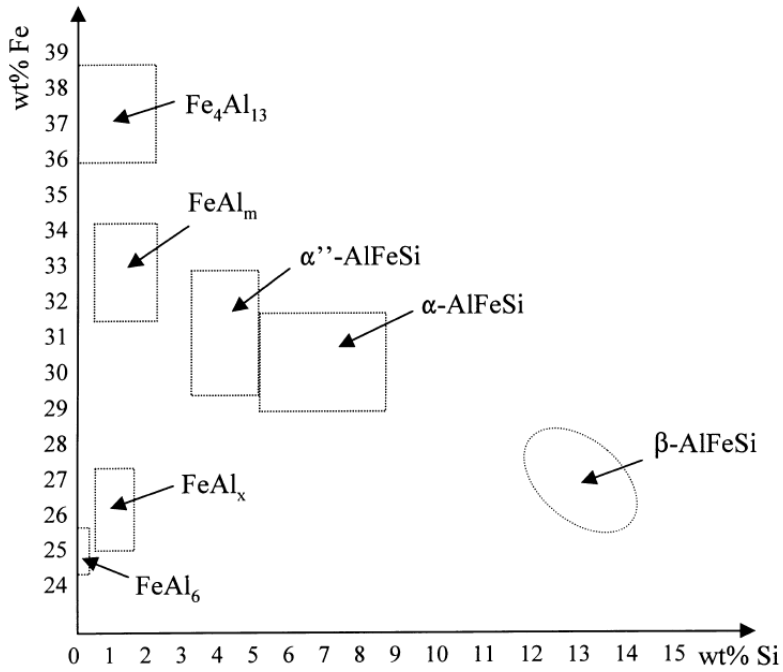

Figure 2-5: Compositions of the common binary and ternary Fe-rich intermetallic phases in Al-Fe and Al-Fe-Si alloys [43].

Al_6Fe is reported to form at a eutectic temperature of ~ 653 °C, with a eutectic composition of ~3 wt% Fe and is often observed in direct chill (DC) cast ingots and billets [52]. It is important to note that (in Mn containing alloys) Al_6Fe and Al_6Mn are isomorphous and Mn can substitute freely for Fe in the Al_6Fe lattice, which raises the thermodynamic stability of the Al_6Fe phase [43].

The metastable Al-Al_mFe eutectic appears at higher cooling rates (e.g. >10 Ks^{-1} of Al-0.6 wt% Fe), than those at which $Al_{13}Fe_4$ and Al_6Fe form and has been observed in the more rapidly cooled zones of DC cast billets [43,52].

The ternary Al-Fe-Si phases form at higher bulk concentrations of Si (>0.1 % Si in ≤0.2 wt% Fe and >0.2 % Si in ≤0.3-0.4 wt% Fe containing alloys) [43,53]. Silicon can be dissolved into the "binary" Fe aluminides. Due to the different degrees of Si solubility, the occurrence of Al_6Fe, which can only

accommodate up to 0.5 wt% Si in its lattice, is limited in Al-Fe-Si alloys and replaced by intermetallic phases capable of accommodating more Si, such as $Al_{13}Fe_4$ or Al_mFe [43].

With a sufficiently high Si content, three ternary phases can form in Al-Fe-Si alloys under equilibrium solidification conditions below the liquid → Al+$Al_{13}Fe_4$ eutectic temperature. The three equilibrium ternary phases originate by either two ternary peritectic reactions followed by a ternary eutectic reaction:

- Liquid + $Al_{13}Fe_4$ → Al + Al_8Fe_2Si (α-phase)
- Liquid + Al_8Fe_2Si → Al + Al_5FeSi (β-phase)
- Liquid → Al + Si + Al_5FeSi

Non equilibrium solidification conditions lead to an enrichment in Si (partitioning of the Si to the interdendritic liquid), resulting in a greater tendency for the formation of ternary phases [43]. Several metastable structural variants of the α and β phases are commonly observed in commercial DC casting alloys, as summarized in Table 2-2 [43].

Table 2-2: Common Al-Fe-Si phases observed in commercial DC casting alloys.

Fe-rich intermetallic phases	**Crystal structure**	**Reference**
α_1	Cubic	[5,54–57]
α_2	Hexagonal	[5,58]
q_1	c-Centered orthorhombic	[46,51]
q_2	Monoclinic	[51]
α_v	Monoclinic	[46,59]
α_T	c-Centered monoclinic	[60]
β	Monoclinic	[5,61,62]
β’	Monoclinic	[43,52]

The most prominent Fe-rich phases in Al wrought alloys containing Si are the α-phase and the β-phase. Cooper et.al [54] and Skjerpe et.al [55] confirmed the body-centered cubic crystal structure of the α-phase, while in other references [5,58] a hexagonal structure is mentioned. Since the hexagonal form of α-AlFeSi is only stable in high purity Al-Fe-Si alloys [5] and trace elements such as V, Cr, Mn, Cu, Mo and W tend to promote a body-centered cubic structure for α-AlFeSi, the cubic lattice is most commonly observed in commercial alloys [43]. It should be noted that the cubic structure is isostructural with α-AlMnSi and only 0.1 % Mn is required to stabilize the cubic lattice during solidification at a cooling rate of 0.75 $Kmin^{-1}$ [43]. As depicted in Figure 2-6, the α-phase is characterized by its compact (star like or polygon) and Chinese script or branched morphology in contrast to the platelet β-phase [4].

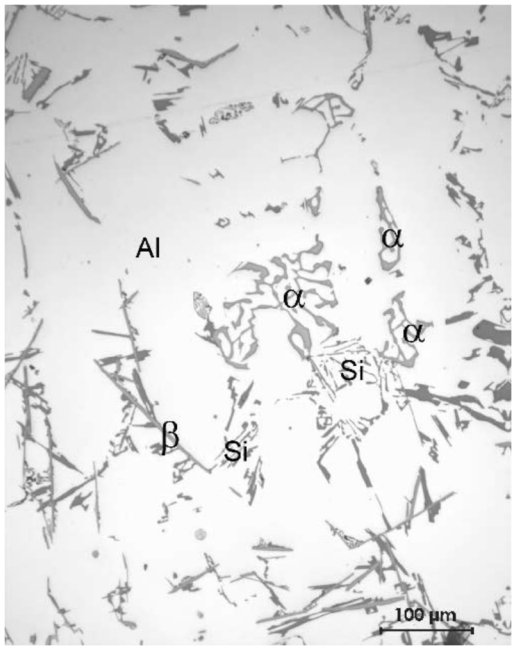

Figure 2-6: Typical morphology of the α- and β-phase [63].

Figure 2-7 shows the a) as cast structure of an Al-9%Si-1%Fe-0.5%Mn alloy and the three-dimensional reconstruction of the α-phase [64]. Here the α-phase obtains two distinct morphologies: A blocky, polyhedral structure at the core of the particle and a convoluted three-dimensional branched structure in the outer regions [64]. The polyhedral structure of the α-phase occurs when it forms as a primary phase before the aluminum dendrites begin to solidify, and it grows in a faceted manner, resulting in an approximately hexagonal shape in cross section [5,64]. After the Al dendrites have begun to solidify, Al and α-phase form a coupled eutectic, causing a transition in morphology from the large primary polyhedral crystal to the branched arm structure seen in Figure 7b [64]. Likewise, the Chinese script morphology is associated with coupled growth via a binary eutectic reaction with the α-Al phase [65]. The appearance of the large, faceted crystals is determined by alloy composition (Fe, Mn) and solidification speed i.e. cooling rate during casting.

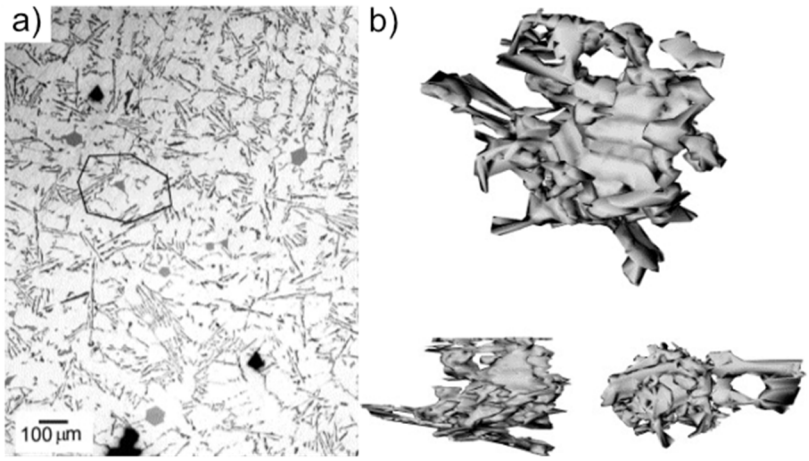

Figure 2-7: a) As cast structure of an Al-9%Si-1%Fe-0.5%Mn alloy and b) three-dimensional reconstruction of the α-phase. A highly convoluted arm structure is observed growing from a polyhedral crystal at the center of the particle [64].

If chemical and crystallographic information is provided, the plate-shaped β-phase is usually described to be monoclinic [61,62], however there are also publications in which an orthorhombic or tetragonal structure of the β-phase is assumed [66]. Figure 2-8 shows the a) as cast structure of an Al-9%Si-1%Fe alloy and b) the three-dimensional reconstruction of the β-phase [64]. The arrowed feature represents a "hole" in which case the intermetallic β-phase has grown around a pre-existing dendrite [64]. A high iron content favors the formation of an Al-Si-Al_5FeSi ternary eutectic. First the large platelets form prior to the ternary eutectic [64]. The smaller platelets are likely to form as part of the ternary eutectic, creating a complex interconnecting network [64]. This network may form by impingement of individual platelets during growth rather than by branching of individual platelets. β-phase platelets grow beyond the point of intersection, even growing around an obstructing platelet, similar to the growth around a dendritic arm seen in Figure 8b [64].

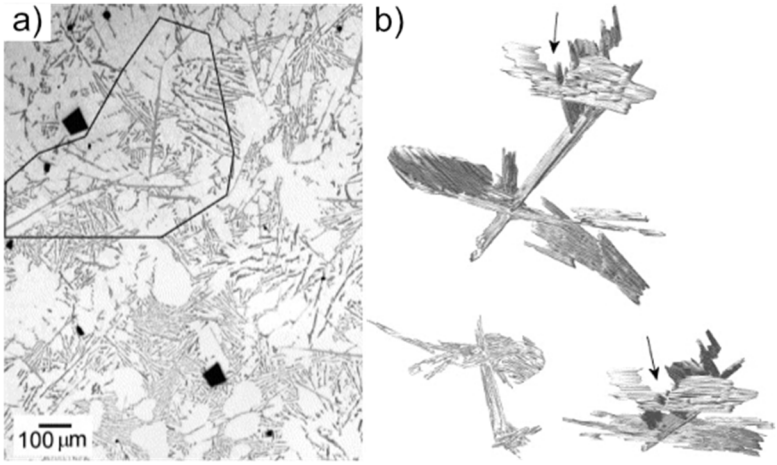

Figure 2-8: a) As cast structure of an Al-9%Si-1%Fe alloy and b) three-dimensional reconstruction of the platelet β-phase. The arrow shows a hole where the intermetallic β-phase has grown around a pre-existing dendrite. [64].

In addition to the phases described above, another Fe-rich phase may form in the Al-Mg-Si-Fe system, which is referred to as the π-$Al_8FeMg_3Si_6$ phase and appear in a script-like morphology in high-Mg cast alloys [67–69]. This phase is usually unwanted in Al-Mg-Si alloys as it binds Mg and Si, both of which are important elements for precipitation hardening.

2.5 Effect of Fe on microstructure and mechanical properties in Al-alloys

The effect of primary iron-rich phases (IMPs) on mechanical properties is widely discussed in the literature. High Fe content is generally considered negative for ductility and formability. The reason for this is the premature initiation of cracks near brittle primary phases. For most foundry alloys the compact Morphology of the α-phase is preferred, as a considerably less detrimental effect on the mechanical properties, in contrast to the plate-like β-phase, can be assumed (fracture resistance

decreases as β-phase formation increases) [4,5,70,71]. In-situ tensile tests on as-cast samples with different Mn contents (to modify the occurring primary phases – formation of α-phase in high Mn and β-phase in low Mn alloy) were performed by Bjurenstedt et.al [72]. Figure 2-9 demonstrates crack formation and propagation in a) low Mn alloy (crack through β-phase) and in b) high Mn alloy (crack through α-phase) [72]: Cracks are initiated by particle fracture at the elongated β-intermetallics oriented parallel to the test direction (indicated with an arrow). A macrocrack was observed to form in connection with the transversely oriented Fe-rich primary β-phase (Figure 2-9a). In the high-Mn alloy (Figure 2-9b) fracture starts at the largest α-phase particles. As the strain increases, the adjacent IMPs fracture and the resulting microcracks begin to interconnect through the Al matrix to form a macroscopic crack. It can be concluded that a high local density of large IMPs is particularly deleterious and that the morphology, size and distribution of brittle IMPs dominate the ductility and forming behavior of Fe-rich alloys. [72]

Similar to foundry alloys, coarse, high aspect ratio IMPs in Al-sheet materials are typical sites for damage initiation, which occurs via microcrack and void formation in the particle or decohesion of the matrix interface with the IMP [72–75]. These voids, which soften the matrix material, contribute significantly to the formation of shear bands, and the resulting localized deformation eventually leads to ultimate failure during forming operations [75–77]. As mentioned above, there are two types of void nucleation. In a soft matrix, void nucleation predominately occurs by particle decohesion, while a hard Al-matrix forces the fracture of second phase particles, inclusions, and precipitates [74]. In the case of ductile transgranular fracture, void growth (high stress triaxiality) and distortion (low stress triaxiality) may take place [74]. Finally, the voids are eventually connected by an instability in the intervoid ligament.

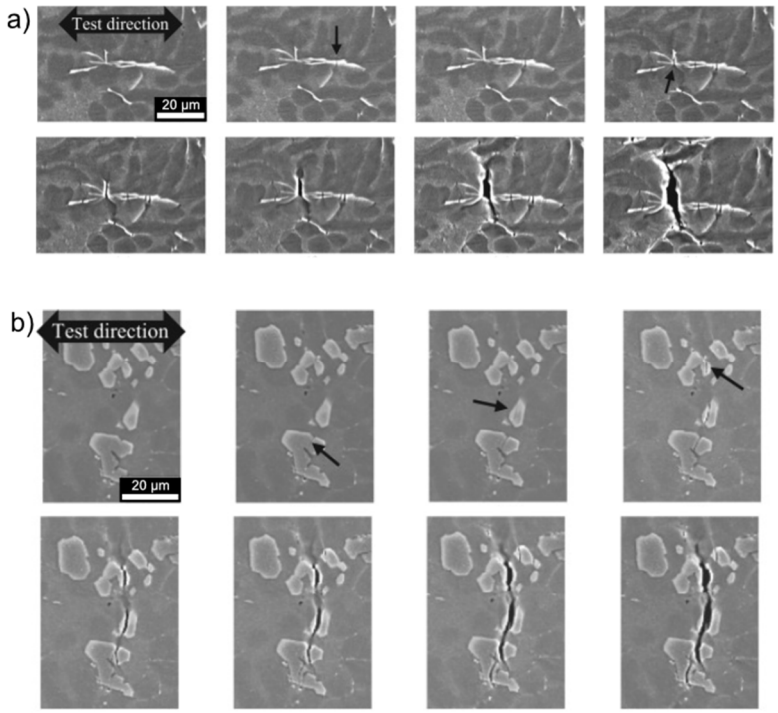

Figure 2-9: Crack formation and progression in a) low-Mn alloy (β-phase is dominant) and b) high Mn-alloy (α-phase is dominant) with increasing elongation adapted from [72].

Nevertheless, elevated Fe levels do not solely exert negative effects. During casting of commercially pure aluminum, iron can serve as a grain refiner. As stated by Zhang et.al [78], the refinement of grains due to iron reached its maximum at a concentration of 0.5%. However, even at lower and very high iron concentrations (0.2% and 1.2%), significantly finer grains were achieved in comparison to the pure aluminum sample, as illustrated in Figure 2-10. The casting temperature was 725 ± 5 °C and it should be noted that no additional grain refining agent, such as titanium boride, was used in this study. The refinement mechanism of the AlFe alloy utilized in this study is attributed to the mutual effect of promoting nucleation of new Al-crystals and the pinning of grain boundaries by the Al_3Fe intermetallic phase. [78]

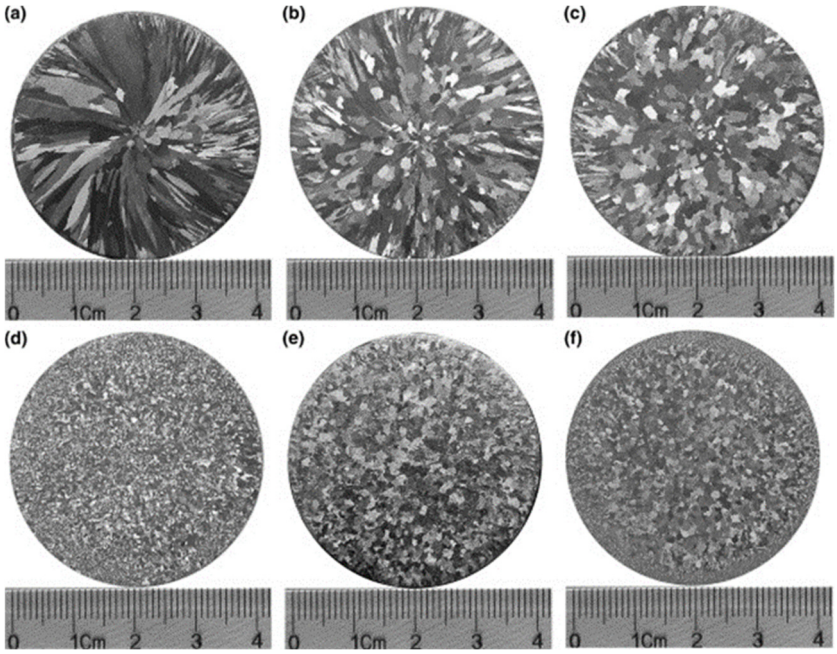

Figure 2-10: Micrographs of (a) pure aluminum, which were refined by the addition of iron (b) 0.2 % Fe (c) 0.3 % Fe (d) 0.5 % Fe (e) 0.8 % Fe and (f) 1.2 % Fe [78].

The literature also reports an refinement in microstructure due to increased Fe content in Al-Mg-Si wrought alloys, which is associated with improved mechanical properties [71,79]. The microstructure can be effectively adjusted by recrystallization via iron-rich primary and secondary phases due to the locally disparate effects of PSN of coarse primary IMPs (>1 μm) and the pinning force of fine particles (< 1 μm) [12,80]. In the presence of multiscale particles, the minimum IMP-size d_{min} to successfully act as a nucleation site for new grains can be approximated by Eq. 2-4 [12,40,80,81].

$$d_{min} = \frac{4 \cdot \gamma_{gb}}{P_D - P_Z} = \frac{4 \cdot \gamma_{gb}}{\frac{\rho \cdot G \cdot b^2}{2} - \frac{3 \cdot f_d \cdot \gamma_d}{d_d}} \qquad \text{(Eq. 2-4)}$$

γ_{gb} High angle grain boundary interfacial energy [J/m²]

P_D Driving pressure for growth resulting from stored deformation energy [J/m]

P_Z Zener pinning pressure [J/m]

ρ Dislocation density [m^{-2}]

b Burgers vector [m]

G Shear modulus [N/m^2]

f_d Volume fraction of dispersoids [-]

γ_d Interfacial energy dispersoid/Al-Matrix [J/m^2]

d_d Dispersoid diameter [N/m^2]

Iron-rich IMPs strongly influence the size, morphology and orientation of the recrystallized grains. The network of the as-cast structure of primary phases can be fragmented into different size categories of IMPs during the rolling process [20,82]. With an increase in the amount of ~1 μm sized Fe-rich particles, the nucleation rate of new grains during recrystallisation (PSN) rises, resulting in a stronger grain refining effect [20,83]. In addition, when PSN dominates the recrystallization process, more random grain orientations are formed, resulting in a rather weak texture with preferential formation of the $Cube_{ND}$ component [20,40,80,84]. By utilizing the PSN effect by alloying with Fe, an increase in the mean vertical anisotropy R_{mean} and a decrease in the planar anisotropy ΔR have been found for Al-Mg-Si [80] and AlZnMgCu [20] alloys, which is helpful for forming operations such as deep drawing.

2.6 Control of Fe-rich phases by alloying elements

As mentioned in Section 2.5, a high iron content in aluminum alloys is most often associated with a decrease in ductility. This is due to brittle primary phases that form in a coarse and unfavorable morphology. If a high content of Fe is present in AlSi alloys, it usually manifests as the thin-platelet β-phase, which can grow up to several millimeters during casting. The main factors that contribute to the formation of the β intermetallic phase are an Fe/Si atomic ratio close to unity (low Si and high Fe content), a low cooling rate ~0.8 °C/s, and low Mn and Cr concentrations [85]. Among the Fe-rich phases, β-AlFeSi causes the most serious loss of ductility, and much effort has been devoted to preventing its formation [86]. Alloying elements can be used to suppress the formation of the long-needle shaped β-phase.

Manganese is the most frequently used element to promote the formation of the α-phase (branched or star-like shapes), whose exact morphology depends also on the solidification rate as well as on the concentration of silicon, iron and manganese [45,79,86,87]. Mn favors the transformation of β–AlFeSi to α-Al(FeMn)Si [79,85]. The crystal structure of the α-phase was found to change with increasing Mn content (body-centered cubic for α-AlFeSi and simple cubic for α-AlMnSi) [87]. The amount of Mn necessary to fully suppress the β-phase at a certain Fe-concentration is difficult to

determine, since the alloys composition as well as process related parameters (see section 2.7: Control of Fe-rich phases by processing), also determine the final morphology of Fe-rich primary phases. In general, however, an Mn:Fe ratio of over 0.5 is desirable if the iron content is beyond 0.45 wt% [4,86]. The replacement of the β-phase by manganese compounds also increases the corrosion resistance at least in the copper-free alloys (reduction in potential between the iron-bearing compounds and the Al-matrix) [45]. It must be noted that an increase in Mn also contributes to an increase in primary phases formed and to an increase in the segregation factor (Eq. 2-5), which eventually leads to sludge formation [45,79].

$$SF = 1 \cdot Fe + 2 \cdot Mn + 3 \cdot Cr \ (wt.\%) \qquad \text{(Eq. 2-5)}$$

In copper-containing aluminum alloys, the acicular Al_7Cu_2Fe phase may form by binding Cu into the Al_3Fe phase, which, similar to the β-AlFeSi phase, leads to a reduction in ductility due to its unfavorable morphology in foundry alloys. Mn also promotes the formation of the Chinese-script morphology and inhibits the formation of needle-shaped Al_7Cu_2Fe particles [4,5,20].

Chromium is even more effective than Mn and a Cr/Fe ratio of 0.33 can prevent the formation of β-AlFeSi, but with a factor of three in Eq. 5, Cr strongly promotes sludge formation at higher concentrations [4]. Similar to Mn, which forms α-Al(Mn,Fe)Si dispersoids, chromium forms α-Al(Cr,Fe)Si dispersoids during homogenization. The distribution of this AlFeSi dispersoids is strongly dependent on the heating rate. At a slow heating rate (< 3 °C/min), many homogeneously distributed β'-Mg_2Si precipitates (not to be mistaken for β-AlFeSi) are formed, which facilitates the heterogeneous nucleation of homogeneously distributed α-AlFeSi dispersoids [36,37,88].

Less effective than manganese or chromium, cobalt (a rather expensive element), is also said to modify the platelet Fe-rich primary phase to globular shape and a Co/Fe ratio of 0.5-1.0 was suggested [4]. Beryllium alters the solidification sequence of Fe-rich phases, as the ternary eutectic reaction to create the β-phase is replaced by a peritectic reaction forming Be-Fe phases in Al-Mg-Si cast alloys [89]. However, due to its highly toxic effect, beryllium is used only in rare instances [90]. Strontium has been added to Al wrought alloys because it promotes the formation of α-AlFeSi, which improves extrusion properties [4]. It has also been reported that the addition of 0.01-0.1 wt.% Sr to AlCuMgZn wrought alloys results in the refinement of intermetallic primary phases [4]. Strontium may also be associated as a surface-active element. It is presumed that Sr can be absorbed on the surface of primary α-AlFeSi to act as a barrier for dissolution, which hinders the peritectic reaction Liquid + Al_8Fe_2Si → Al + Al_5FeSi (β-phase) [4].

2.7 Control of Fe-rich phases by processing

The morphology of the Fe-rich primary phases can be decisively adjusted during the casting process. A pronounced formation of Chinese script α-phase is observed to form at high casting temperatures

(above 800 °C) [4]. However, the disadvantages of high casting temperatures are increased oxidation loss, gas absorption, energy costs and furnace wearing.

Fast solidification (~50 K/s) favors the formation of α-AlFeSi, while at slow (i.e. industrial) cooling rates (<10 K/s) the β-phase is more pronounced [91,92]. The cooling rate during casting determines the speed of the α to β reaction. If the solidification rate is high, the α phase is retained due to rapid cooling before transformation to the β phase. On the other hand, if the cooling rate is slow, there is enough time for the transformation reaction to occur, resulting in a higher relative content of β-AlFeSi. Since high Fe content promotes β-phase formation, higher cooling rates are required to avoid it [4]. In addition, rapid solidification causes a refinement of Fe-rich primary IMPs and aluminum grains and promotes the precipitation of more fine α-dispersoids during homogenization due to a higher supersaturation of the Al matrix with elements such as Mn and Cr [93].

Heat treatments near the solidus temperature can be applied to significantly change the morphology of iron-rich particles. During homogenization at high temperatures IMPs can be partially dissolved, fragmented and transformed into a more roundish shape [94]. Platelet β-particles are transformed into roundish α-particles between 530 °C and 600 °C. This significantly improves the formability in process steps such as extrusion, as the platelet-shaped β phases can lead to local cracking and surface defects. The kinetics of this β-AlFeSi to α-Al(FeMn)Si transformation in Al-Mg-Si alloys depends on temperature, alloying elements (Mn and Si) and the morphology and size of the β-phase itself. Silicon dissolved in solid solution strongly effect the β↔α transformation rate during homogenization annealing. More silicon in solid solution leads to longer transformation times, while higher annealing temperatures and the alloying element manganese tend to strongly accelerate this transformation. Since the α-phase begins to grow on each β-plate during homogenization (as shown in Figure 11), the transformation time increases with increasing β-plate thickness and initial radii. [95,96]

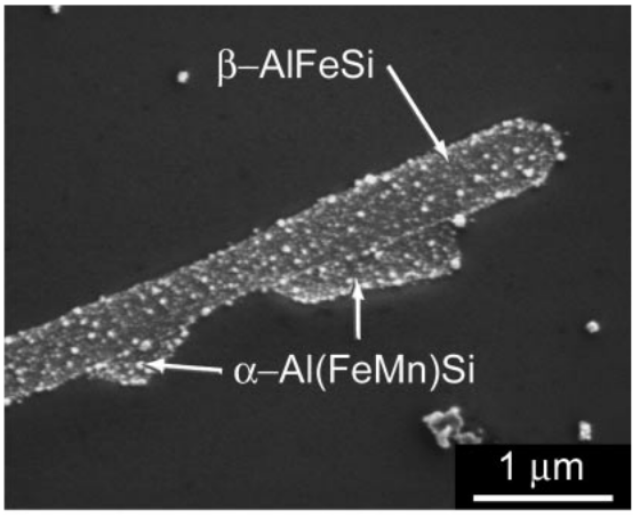

Figure 2: Growth of individual α-phase particles on a platelet β-phase during homogenization [94].

Intermetallic iron-rich phases can also be fragmented by deformation processes, such as rolling of high-Fe alloys (i.e., 8xxx alloys), which reduces their size and increases their number density [82]. The

effectiveness of IMP fragmentation can be influenced by the initial morphology and size of the primary phases in the cast structure. The chemical composition and type of IMPs may also play a role in fragmentation, as they exhibit different degrees of elastic modulus and hardness, as measured by nanoindentation and Vickers hardness tests in [97]. It is also expected that the matrix strength and the degree of deformation will have a major impact on IMP fragmentation (difference between hot and cold rolling).

In alternative processes, such as centrifugal atomization of an Fe-enriched Al melt and subsequent hot extrusion, it was shown that even extreme Fe contents of up to 17 wt.% can be controlled. The resulting microstructure, consisting of the aluminum matrix and very finely dispersed intermetallic phases, led to high thermal stability, hardness and compressive ductility. [98]

High-speed twin-roll strip casting is a method of producing thin strips directly from the melt. The main advantage over conventional casting methods, such as continuous casting, is the very high solidification speed, which results in grain refinement, a higher supersaturation of the relatively insoluble elements and a much more favorable morphology and size of the primary phases. Using this technology Fe-contents up to 3 wt.% form fine IMPs in Al-Mg-Si alloys. [99,100]

2.8 References

[1] M. Bertram, S. Ramkumar, H. Rechberger, G. Rombach, C. Bayliss, K.J. Martchek, D.B. Müller, G. Liu, Resources, Conservation and Recycling 125 (2017) 48–69.

[2] D. Raabe, D. Ponge, P.J. Uggowitzer, M. Roscher, M. Paolantonio, C. Liu, H. Antrekowitsch, E. Kozeschnik, D. Seidmann, B. Gault, F. de Geuser, A. Deschamps, C. Hutchinson, C. Liu, Z. Li, P. Prangnell, J. Robson, P. Shanthraj, S. Vakili, C. Sinclair, L. Bourgeois, S. Pogatscher, Progress in Materials Science 128 (2022) 100947.

[3] N.C.G. Silveira, M.L.F. Martins, A.C.S. Bezerra, F.G.S. Araújo, Sustainability 13 (2021) 12741.

[4] L. Zhang, J. Gao, L.N.W. Damoah, D.G. Robertson, Mineral Processing and Extractive Metallurgy Review 33 (2012) 99–157.

[5] L.F. Mondolfo, Aluminium alloys: Structure and properties, Butterworth, London, Boston, 1979.

[6] D. Raabe, C.C. Tasan, E.A. Olivetti, Nature 575 (2019) 64–74.

[7] F. Ostermann, Anwendungstechnologie Aluminium, 3rd ed., Springer Vieweg, Berlin, 2014.

[8] SA Court, DJ Lloyd, Effects of Si on the aging behaviour and formability of aluminum alloys based on AA6016.

[9] M.X. Guo, G. Sha, L.Y. Cao, W.Q. Liu, J.S. Zhang, L.Z. Zhuang, Materials Chemistry and Physics 162 (2015) 15–19.

[10] L. Stemper, M.A. Tunes, R. Tosone, P.J. Uggowitzer, S. Pogatscher, Progress in Materials Science (2021) 100873.

[11] M. Lentz, G. Laptyeva, O. Engler, Journal of Alloys and Compounds 660 (2016) 276–288.

[12] F.J. Humphreys, M. Hatherly, Recrystallization and related annealing phenomena, 2nd ed., Elsevier, Amsterdam, 2004.

[13] G. Gottstein, Materialwissenschaft und Werkstofftechnik, Springer Berlin Heidelberg, Berlin, Heidelberg, 2014.

[14] A.R. Eivani, S. Valipour, H. Ahmed, J. Zhou, J. Duszczyk, Metall Mater Trans A 42 (2011) 1109–1116.

[15] S. Li, Q. Zhao, Z. Liu, F. Li, J. of Materi Eng and Perform 27 (2018) 3350–3373.

[16] O. Engler, J. Hirsch, International Journal of Materials Research 100 (2009) 564–575.

[17] S. de La Chapelle, Scripta Materialia 45 (2001) 1387–1391.

[18] A.L. Dons, E. Nes, Materials Science and Technology 2 (1986) 8–18.

[19] W. Wang, A.-L. Helbert, T. Baudin, F. Brisset, R. Penelle, Materials Characterization 64 (2012) 1–7.

[20] L. Yuan, M. Guo, K. Yu, J. Zhang, L. Zhuang, Philosophical Magazine 101 (2021) 1417–1442.

[21] T.A. Bennett, R.H. Petrov, L. Kestens, L.-Z. Zhuang, P. de Smet, Scripta Materialia 63 (2010) 461–464.

[22] G.J. Baczynski, R. Guzzo, M.D. Ball, D.J. Lloyd, Acta Materialia 48 (2000) 3361–3376.

[23] T.A. Bennett, R.H. Petrov, L. Kestens, SSP 160 (2010) 197–202.

[24] T.A. Bennett, R.H. Petrov, L. Kestens, Scripta Materialia 61 (2009) 733–736.

[25] O. Engler, C. Schäfer, H.-J. Brinkman, Acta Materialia 60 (2012) 5217–5232.

[26] O. Engler, J. Hirsch, International Journal of Materials Research 100 (2009) 564–575.

[27] T.A. Bennett, J. Sidor, R.H. Petrov, L.A.I. Kestens, Advanced Engineering Materials 12 (2010) 1018–1023.

[28] T.A. Bennett, R.H. Petrov, L. Kestens, Scripta Materialia 62 (2010) 78–81.

[29] Y. Li, Q.-P. Wang, G.-J. Gao, J.-D. Li, Z.-D. Wang, G.-M. Xu, Rare Met. 38 (2019) 937–945.

[30] O. Engler, J. Aegerter, D. Calmer, Materials Science and Engineering: A 775 (2020) 138965.

[31] Y. Zhu, Metall Mater Trans A 52 (2021) 4715–4726.

[32] J.-M. Lee, S.-B. Kang, T. Sato, H. Tezuka, A. Kamio, Mater. Trans. 43 (2002) 2487–2493.

[33] M. Balakrishnan, I. Dinaharan, R. Palanivel, R. Sathiskumar, Journal of Alloys and Compounds 785 (2019) 531–541.

[34] H. Zhong, P.A. Rometsch, L. Cao, Y. Estrin, Materials Science and Engineering: A 651 (2016) 688–697.

[35] A. Arnoldt, L. Semmelrock, D. Soukup, J.A. Österreicher, Materials Characterization 191 (2022) 112138.

[36] L. Lodgaard, N. Ryum, Materials Science and Technology 16 (2000) 599–604.

[37] L. Lodgaard, N. Ryum, Materials Science and Engineering: A 283 (2000) 144–152.

[38] Y.J. Li, A. Muggerud, A. Olsen, T. Furu, Acta Materialia 60 (2012) 1004–1014.

[39] O. Engler, J. Hirsch, Materials Science and Engineering: A 336 (2002) 249–262.

[40] B. Lu, Y. Li, Y. Wang, X. Qian, G. Xu, Z. Wang, Materials Characterization 176 (2021) 111038.

[41] Y. Birol, Journal of Materials Processing Technology 202 (2008) 564–568.

[42] O. Keles, M. Dundar, Journal of Materials Processing Technology 186 (2007) 125–137.

[43] C.M. Allen, K. O'Reilly, B. Cantor, P.V. Evans, Progress in Materials Science 43 (1998) 89–170.

[44] P. Skjerpe, Journal of Microscopy 148 (1987) 33–50.

[45] S.G. Shabestari, Materials Science and Engineering: A 383 (2004) 289–298.

[46] W. Khalifa, F.H. Samuel, J.E. Gruzleski, Metall Mater Trans A 34 (2003) 807–825.

[47] I.R. Hughes, H. Jones, J Mater Sci 11 (1976) 1781–1793.

[48] R. Young, T.W. Clyne, Scripta Metallurgica 15 (1981) 1211–1216.

[49] P. Skjerpe, Acta Crystallographica Section B: Structural Science, 1988.

[50] C.J. Simensen, R. Vellasamy, International Journal of Materials Research 68 (1977) 428–431.

[51] P. Liu, T. Thorvaldsson, G.L. Dunlop, Materials Science and Technology 2 (1986) 1009–1018.

[52] H. Westengen, International Journal of Materials Research 73 (1982) 360–368.

[53] S. Forder, J. Brooks, A. Reeder, P. Evans, Scripta Materialia 40 (1998) 45–48.

[54] M. Cooper, Acta Cryst 23 (1967) 1106–1107.

[55] P. Skjerpe, Metallurgical and Materials Trans A 18 (1987) 189–200.

[56] M.V. Kral, H.R. McIntyre, M.J. Smillie, Scripta Materialia (2004) 215–219.

[57] M.V. Kral, P.N.H. Nakashima, D.R.G. Mitchell, Metallurgical and Materials Trans. A 37 (2006) 1987–1997.

[58] V. Stefániay, Á. Griger, T. Turmezey, J Mater Sci 22 (1987) 539–546.

[59] A.L. Dons, International Journal of Materials Research 77 (1986) 126–130.

[60] C.L. Jensen, R.K. Wyss, Metall Trans A 19 (1988) 893–898.

[61] G. Carpenter, Y. Le Page, Scripta Metallurgica et Materialia 28 (1993) 733–736.

[62] C.M. Fang, Z.P. Que, Z. Fan, Journal of Solid State Chemistry 299 (2021) 122199.

[63] L. Lu, A.K. Dahle, Metall Mater Trans A 36 (2005) 819–835.

[64] C.M. Dinnis, J.A. Taylor, A.K. Dahle, Scripta Materialia 53 (2005) 955–958.

[65] Z. Que, Y. Wang, Z. Fan, Metall Mater Trans A 49 (2018) 2173–2181.

[66] M.V. Kral, Materials Letters 59 (2005) 2271–2276.

[67] M.F. Ibrahim, E. Samuel, A.M. Samuel, A. Al-Ahmari, F.H. Samuel, Materials & Design 32 (2011) 2130–2142.

[68] H. Möller, W.E. Stumpf, P.C. Pistorius, Transactions of Nonferrous Metals Society of China 20 (2010).

[69] B. Johannesson, C.H. Cáceres, International Journal of Cast Metals Research 17 (2004) 94–98.

[70] J.H. Horng, D.S. Jiang, T.S. Lui, L.H. Chen, International Journal of Cast Metals Research 13 (2000) 215–222.

[71] M.S. Remøe, K. Marthinsen, I. Westermann, K. Pedersen, J. Røyset, C. Marioara, Materials Science and Engineering: A 693 (2017) 60–72.

[72] A. Bjurenstedt, E. Ghassemali, S. Seifeddine, A.K. Dahle, Materials Science and Engineering: A 756 (2019) 502–507.

[73] D. Broek, Engineering Fracture Mechanics 5 (1973) 55–66.

[74] A.E. Tekkaya, P.-O. Bouchard, S. Bruschi, C.C. Tasan, CIRP Annals 69 (2020) 600–623.

[75] W.B. Lievers, A.K. Pilkey, D.J. Lloyd, Materials Science and Engineering: A 361 (2003) 312–320.

[76] W.B. Lievers, A.K. Pilkey, M.J. Worswick, Mechanics of Materials 35 (2003) 661–674.

[77] W. Lievers, Effect of void damage and shear band development on the bendability of AA6111 automotive aluminum alloy sheet, Carleton University, 2001.

[78] Y. Zhang, N. Ma, H. Yi, S. Li, H. Wang, Materials & Design 27 (2006) 794–798.

[79] Y. Wang, Y. Deng, Q. Dai, K. Jiang, J. Chen, X. Guo, Materials Science and Engineering: A 803 (2021) 140477.

[80] M.X. Guo, J. Zhu, Y. Zhang, G.J. Li, T. Lin, J.S. Zhang, L.Z. Zhuang, Materials Characterization 132 (2017) 248–259.

[81] T.A. Bennett, R.H. Petrov, L. Kestens, Scripta Materialia 62 (2010) 78–81.

[82] E. Aryshenskii, J. Hirsch, S. Konovalov, Metals 11 (2021) 507.

[83] H. Jin, D.J. Lloyd, Materials Science and Engineering: A 403 (2005) 112–119.

[84] L. Yu, L. Chen, H. Wang, X. Wang, W. Peng, Y. Wang, L. Zhuang, Metall. Res. Technol. 117 (2020) 508.

[85] M.A. Moustafa, Journal of Materials Processing Technology 209 (2009) 605–610.

[86] S. Ji, W. Yang, F. Gao, D. Watson, Z. Fan, Materials Science and Engineering: A 564 (2013) 130–139.

[87] H.Y. Kim, T.Y. Park, S.W. Han, H.M. Lee, Journal of Crystal Growth 291 (2006) 207–211.

[88] N. Bayat, T. Carlberg, M. Cieslar, Journal of Alloys and Compounds 725 (2017) 504–509.

[89] S. Murali, K.S. Raman, K. Murthy, Materials Science and Engineering: A 190 (1995) 165–172.

[90] J.W. Jordan, C.S. Darke, Thorax 13 (1958) 69–73.

[91] H. Tanihata, T. Sugawara, K. Matsuda, S. Ikeno, Journal of Materials Science 34 (1999) 1205–1210.

[92] S. Belmares-Perales, Met. Mater. Int. 14 (2008) 307–314.

[93] D. Wang, H. Zhang, H. Nagaumi, X. Li, J. Cui, Adv. Eng. Mater. 22 (2020) 2000517.

[94] N. Kuijpers, W.H. Kool, P. Koenis, K.E. Nilsen, I. Todd, S. van der Zwaag, Materials Characterization 49 (2002) 409–420.

[95] N. Kuijpers, C. Vuik, F.J. Vermolen, S. van der Zwaag, Mater. Trans. 44 (2003) 1448–1456.

[96] N. Kuijpers, F.J. Vermolen, C. Vuik, P. Koenis, K.E. Nilsen, S. van der Zwaag, Materials Science and Engineering: A 394 (2005) 9–19.

[97] X. Lan, K. Li, J. Wang, Q. Lu, T. Yang, Y. Xiao, Y. Du, Intermetallics 152 (2023) 107771.

[98] F. Průša, V. Kučera, D. Vojtěch, Materials & Design 132 (2017) 459–466.

[99] K. Suzuki, S. Kumai, Y. Saito, T. Haga, Mater. Trans. 46 (2005) 2602–2608.

[100] T. Haga, M. Ikawa, H. Watari, K. Suzuki, S. Kumai, Mater. Trans. 46 (2005) 2596–2601.

3 ALLOY DESIGN

Based on the chosen crossover approach to merge the microstructure-controlling effect of primary intermetallic phases on processing deployed in the context of foil stock with the age-hardening capability seen in Al-Mg-Si alloys, intensive thermodynamic calculations were conducted. EN-AW 6016 provides the basis for this crossover approach since it is a widely used system for automotive body parts and exhibits high formability. A variety of promising alloys have been calculated using FactSage 8.0 and the latest available database (database applied: FTlight2022) by altering the concentration of elements considered critical to the formation of Fe-rich primary phases (Fe, Mn and Si).

3.1 Approach

To study the effect of different amounts of Fe-rich intermetallics in the wrought Al alloy EN-AW 6016, iron was alloyed together with manganese and silicon. Iron contributes to the formation of brittle primary phases and its content controls the volume fraction of intermetallics formed. Manganese as an alloying element was used as a "Fe-corrector". This element ensures a preferred α-AlFeSi formation especially when the Mn:Fe ratio exceeds 0.5, which is accompanied by a more compact morphology of the primary IMPs in the as-cast state. In addition, Mn leads to the formation of thermally stable dispersoids that precipitate during homogenization annealing, which also contribute to microstructure evolution. It should be noted that the primary AlFeSi phases formed consume a large amount of Si during their formation. In order to set the same conditions for solution annealing and thus not affect precipitation hardening, the silicon content must be adjusted to match the amount of iron and manganese. Based on calculations and literature information, a total of eight alloy compositions were selected for detailed evaluation. Table 3-1 shows the chemical compositions of the thermodynamically evaluated alloys. Note that the Si-adapted alloys are calculated to contain the same Si concentration in solid solution as the reference alloy 6016 at a solution annealing temperature of 560°C, which should ensure similar precipitation kinetics.

Table 3-1: Thermodynamically evaluated alloy compositions given in wt.%

Alloy	Si [%]	Fe [%]	Mn [%]	Mg [%]	Description
Ref.6016	1.1	0.2	-	0.4	Reference alloy
Si-adapted					
A1	1.4	0.8	-	0.4	↑Fe
A2	1.5	0.8	0.5	0.4	↑Fe ↑Mn
A3	1.8	1.5	-	0.4	↑↑Fe
A4	2.1	1.5	1.1	0.4	↑↑Fe ↑↑Mn
Si constant at 1.1 %					
B1	1.1	0.8	-	0.4	↑Fe
B2	1.1	0.8	0.5	0.4	↑Fe ↑Mn
B3	1.1	1.5	-	0.4	↑↑Fe
B4	1.1	1.5	1.1	0.4	↑↑Fe ↑↑Mn

Figure 3-1 shows the equilibrium phase diagrams of the selected alloy systems. At this point it should be noted that the π-$Al_8FeMg_3Si_6$ phase has been excluded from the calculation as this phase is dominant in the current database. The inclusion of the π-$Al_8FeMg_3Si_6$ phase causes great confusion, as FactSage 8.0 suggests that all the Mg is consumed by it, which in turn means that the hardening potential due to metastable Mg_2Si precursor phases is completely lost, which was not observed.

As already mentioned, an increase in Fe results in an overall increase in primary phase fraction. For alloys without Mn, FactSage 8.0 proposes three possible Fe-rich phases: α-AlFeSi, β-AlFeSi and $Al_{14}Fe_3Si_3$ (stable at higher Si-concentrations and lower temperatures). With the addition of Mn, other types of α-phases (α-AlFeMnSi and α-AlMnSi) can be obtained because Mn can substitute for Fe. As seen in Figure 2-4 in section 2, the base alloy EN-AW 6016 counts to the Si-surplus alloys. If no additional Si is added (B-alloy variants) with increasing IMP content, more and more Si will be bound in AlFeSi phases. In alloy B4, all Si is already consumed either by the Fe-rich phases or by Mg_2Si under equilibrium conditions. Mg_2Si is present to a similar extent in all alloys. For the Mn-rich alloys, FactSage 8.0 also suggests that Al_3Fe and Al_6(Fe,Mn) may form very early during solidification. Alloys with very high Fe and Mn concentrations (A4 and B4) will precipitate Fe-rich phases even before the FCC (aluminum mixed crystal) dendrites solidify, which indicates sludge formation.

The modification of primary IMPs is not determined purely by alloying elements. Rather, it is the processing parameters that sets the microstructure in wrought alloys. Starting with the casting conditions, it is already possible to exert a serious impact on the structure of primary IMPs. The solidification rate takes on a particularly high significance. For the initial evaluation, a high solidification rate was preferred, as this should result in a finer network of IMPs that would be easier to modify in subsequent process steps. As the homogenization treatment affects not only the density and size of the dispersoids but also the morphology of the Fe-rich primary phases, this process step

is of particular importance. The decision was made in favor of an industrially comparable annealing treatment to EN-AW 6016, with long heating period and holding times. This should promote the formation of a high density of dispersoids in Mn-rich alloys and contribute to the possible transformation of IMPs. Rolling parameters and heat treatments have been adapted based on the industrially produced EN-AW 6016 to be feasible on smaller scale laboratory equipment.

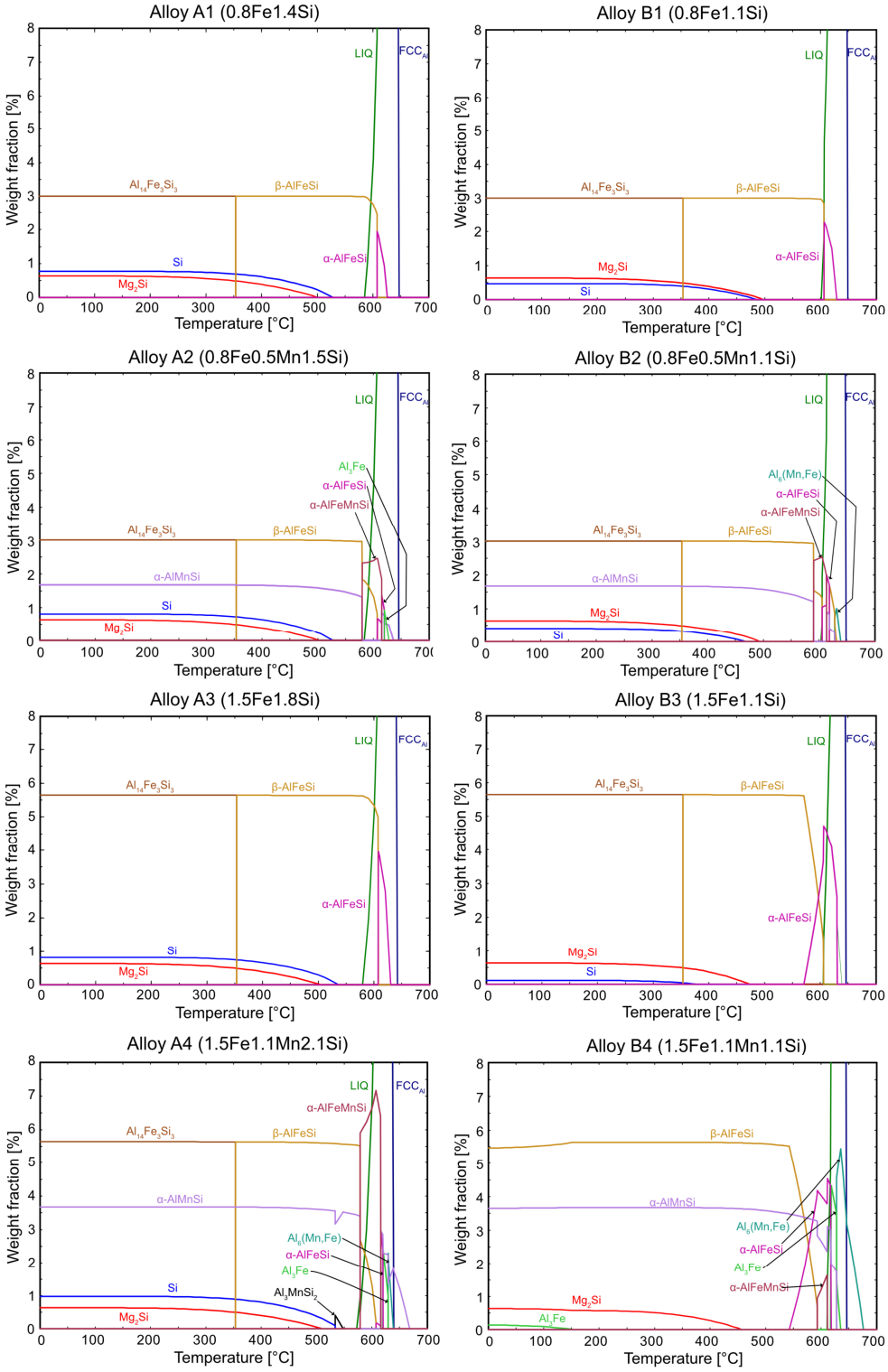

Figure 3-1: Equilibrium phase diagrams of the selected alloy systems (evolution of phase fraction over temperature). Note that π-$Al_8FeMg_3Si_6$ has been excluded from these calculations.

4 IMPROVEMENTS OF MECHANICAL PROPERTIES THROUGH CONTROL OF PRIMARY PHASES

Initial investigations on how to control the morphology of Fe-rich primary phases due to thermomechanical processing and alloy design started in 2021. Alloy 6016 was heavily doped with iron and manganese, resulting in the formation of a network of branched Fe-rich primary phases in the as-cast state, with the Si content adjusted to match the amount of AlFeSi phases formed. Taking into account all the parameters that determine the morphology of IMPs (solidification rate, alloying elements, heat treatments and deformation), these could be transformed into fine particles. Such a high Fe content would normally be associated with a drastic reduction in ductility. However, the test alloy exhibited unique mechanical properties, i.e. higher overall strength, very high strain hardening capability, far more pronounced than in conventional 6xxx series alloys, while maintaining high total elongation values in the uniaxial tensile test.

The goal of this first publication was to describe the mechanisms underlying these improvements in mechanical properties relative to the base material 6016. The main results of this research have been published in the journal "Scripta Materialia" and are shown in the following section.

High Fe content in Al-Mg-Si wrought alloys facilitates excellent mechanical properties [2,3]

Authors contributions

Bernhard Trink:	Conceptualization, Methodology, Investigation, Visualization, Writing – Original Draft.
Irmgard Weißensteiner:	Investigation, Visualization, Writing – Review & Editing.
Katharina Strobel:	Supervision, Writing – Review & Editing.
Peter J. Uggowitzer:	Conceptualization, Writing – Review & Editing.
Stefan Pogatscher:	Project Administration, Conceptualization, Supervision, Writing – Review & Editing.

Acknowledgements

The authors wish to express their sincere thanks to AMAG Rolling for providing the material and for the valuable discussions. This work was funded by the Christian Doppler Research Association within the framework of the Christian Doppler Laboratory for Advanced Aluminum Alloys. Financial support from the Austrian Federal Ministry for Digital and Economic Affairs, the National Foundation for Research, Technology and Development and the Christian Doppler Research Association is gratefully acknowledged.

Abstract

This study investigates the effect of a high volume fraction of Fe-rich intermetallic phases on microstructure evolution and mechanical properties in a cold rolled Al-Mg-Si wrought alloy. A conventional Al-Mg-Si alloy was modified by significantly increasing its Fe and Mn content, while the Si content was adjusted to keep the matrix composition comparable. Subsequent fast solidification and thermomechanical processing generated a dense distribution of fine intermetallic phases, which culminated in significant grain-refinement and uniform texture. The resulting alloy, with almost 10 vol-% Fe-rich intermetallic phase, features an unusually attractive combination of strength and ductility in addition to the substantially increased strain hardening typical of heterostructured materials, and can facilitate a higher usage of scrap input.

[2] B. Trink, I. Weißensteiner, P.J. Uggowitzer, K. Strobel, S. Pogatscher, Scripta Materialia 215 (2022) 114701.

[3] Note that parts of this work were also presented by the author in: B. Trink et al. (2023): AMAG CrossAlloy.68: Excellent mechanical properties at high Fe-content, AluReport 01/2023, AMAG AG.

4.1 Introduction

A major challenge in the recycling of aluminum is the highly diverse composition of aluminum scrap. Among other elements, Fe poses a particular problem as (i) it gradually accumulates through the recycling of secondary aluminum and (ii) it is difficult to remove by metallurgical means [1,2]. Due to the low solubility of Fe in the aluminum solid solution (<0.05 wt.%), it tends to form primary phases during the casting process [3]. The effect of Fe in aluminum casting alloys has already been studied extensively [4–7]. The most important Fe-rich primary intermetallic phases (hereafter "IMPs") in aluminum alloys containing Si are α-AlFeSi and β-AlFeSi [5]. The α-phase is characterized by a much more compact morphology than that of the plate-like β phase [8,9]. For this reason, because of its influence on mechanical properties, α-AlFeSi is preferred [1]. Most of the Fe-rich primary IMPs are known to reduce ductility and to negatively affect formability [3]. Modifying their structure and morphology (e.g by adding Mn [10–12]) might reduce their negative effects. In addition, fast solidification (>10 K/s) is known to promote beneficial formation of refined α-AlFeSi instead of β-AlFeSi [1,13], with a higher solidification rate required at higher Fe content. Iron-rich IMPs can also be fragmented and converted to more rounded shapes by heat treatments [14,15]. Homogenization between 530 °C and 600 °C triggers the transformation of plate-shaped β-particles to globular α-particles, which is known to improve formability and prevent localized cracking and surface defects [10,12,16].

Interestingly, foil materials (i.e. 8xxx alloys [17]) typically have a very high Fe content and exhibit good elongation and forming properties. Recently a study in the context of other Al alloys showed that a crossover between different classes of alloys offers great potential in terms of combining positive properties (i.e. good formability and high strength were seen for a crossover between 5xxx and 7xxx alloys in [18]). Inspired by this, we aimed for a crossover between 6xxx and Fe-rich 8xxx series alloys.

In this study we demonstrate that a purposely generated high volume fraction of hard iron-rich IMPs can be used to positively influence grain size, final material properties, and recyclability. The concept shows hetero-deformation-induced (HDI) strengthening and HDI strain hardening to improve mechanical properties [19,20] of the final sheet characteristics of Al-Mg-Si wrought alloys with high Fe-content.

4.2 Experimental

To synthesize the test alloy with high IMP content, the alloy EN-AW 6016 containing 1.2% Si, 0.4% Mg, 0.2% Fe and 0.1% Mn, which served as a reference, was remelted, and Mn (75% Mn and 25% Al reagent), Fe (75% Fe and 25% Al reagent) and Si (100% Si reagent) were added via master alloys (contents given in wt.%). The chemical composition of the test alloy with high IMP content (6016+IMPs) exhibit the following values: 1.9% Si, 0.4% Mg, 1.4% Fe and 1.1% Mn. In addition to

the increase in Fe and Mn, the Si content was deliberately increased to account for its incorporation into IMPs and to enable a similar amount of dissolved Mg and Si at the solution treatment temperature (calculated by FactSage 8.0 database FTlite). The alloys were subjected to similar processing procedures: remelting and alloying of the elements in an induction furnace; casting into a rectangular copper mold as described in [21] (cooling rate ≈ 60 °C/s, capacity of 100 g); homogenization treatment at 560 °C with a heating period of 8h, followed by a holding time of 11h; hot-rolling with a laboratory rolling mill from 12 mm to 7.3 mm and cold rolling to 1.2 mm sheet thickness, with intermediate annealing at 560 °C for 25 minutes at 3.1 mm; and finally solution heat treatment at 560 °C for 2 minutes in a contact press, with subsequent quenching in water at RT.

Tensile tests were performed directly after solution heat treatment and after 16 days of natural aging at room temperature using a Zwick/Roell Z 100 model tensile testing machine with a gauge length for the samples of 45 mm and a crosshead speed of 0.0032 mm/s in the rolling direction. For microstructural analysis the cross-section planes of the sheet material (rolling and normal direction) were prepared by standard metallographic procedures. Microstructural analysis was performed on a scanning electron microscope (SEM) type JEOL-7200F. The evaluation of the IMPs was carried out using the software package ImageJ. Electron backscattered diffraction (EBSD) was performed using a Symmetry S2 detector from Oxford Instruments. For data analysis, the software package Aztec Crystal and the mtex toolbox were utilized [22]. The orientation distribution functions were evaluated as described in [23].

4.3 Results and discussion

The results of the microstructural evaluation are shown in Figure 4-1 for both alloys, 6016 (a-c) and 6016+IMPs (d-f). In the as-cast condition (central area), the IMPs in the reference 6016 alloy (Figure 4-1 a) are mostly fine and elongated in shape, while homogenization (Figure 4-1 b) entails a certain degree of curvature (darker structures seen in the insert of Figure 4-1 b are artefacts from metallographic preparation). In alloy 6016+IMPs (Figure 4-1 d), the morphology resembles that of an Al-α-AlFeSi eutectic with a twisted arm structure. This "Chinese script" morphology forms by coupled growth via a binary eutectic reaction with the α-Al phase [5]. The EBSD analyses reveal a cubic structure. This crystal structure, together with the twisted arm morphology, are strong indications for the α-AlFeSi phase [1]. Thermodynamic simulations with the FactSage 8.0 software package and EDS measurements also support the evidence of α-Al(Fe,Mn)Si phases. For both, 6016 and 6016+IMPs, primary silicon was not detected in as cast condition. The homogenization treatment induces distinct changes in the morphology of the primary phases (Figure 4-1 e). Besides a coarsening of the previously fine lamellar structure, a fragmentation into individual particles is evident. After rolling and solution annealing (Figure 4-1 f), the IMPs in 6016+IMPs feature a refined shape with rounded edges. On average, the area fraction of the IMPs in 6016+IMPs is 9.1% and the calculated mean equivalent circular diameter is 780±495 nm (note: to avoid including fine secondarily

precipitated particles and dispersoids in the evaluation of IMPs, only particles with an equivalent circular diameter >200 nm were used for the calculation of the mean equivalent circular diameter). In comparison, the area fraction of reference alloy 6016 (Figure 4-1 c) is less than 0.5 %. As expected, the rolling process aligned the IMPs in the rolling direction.

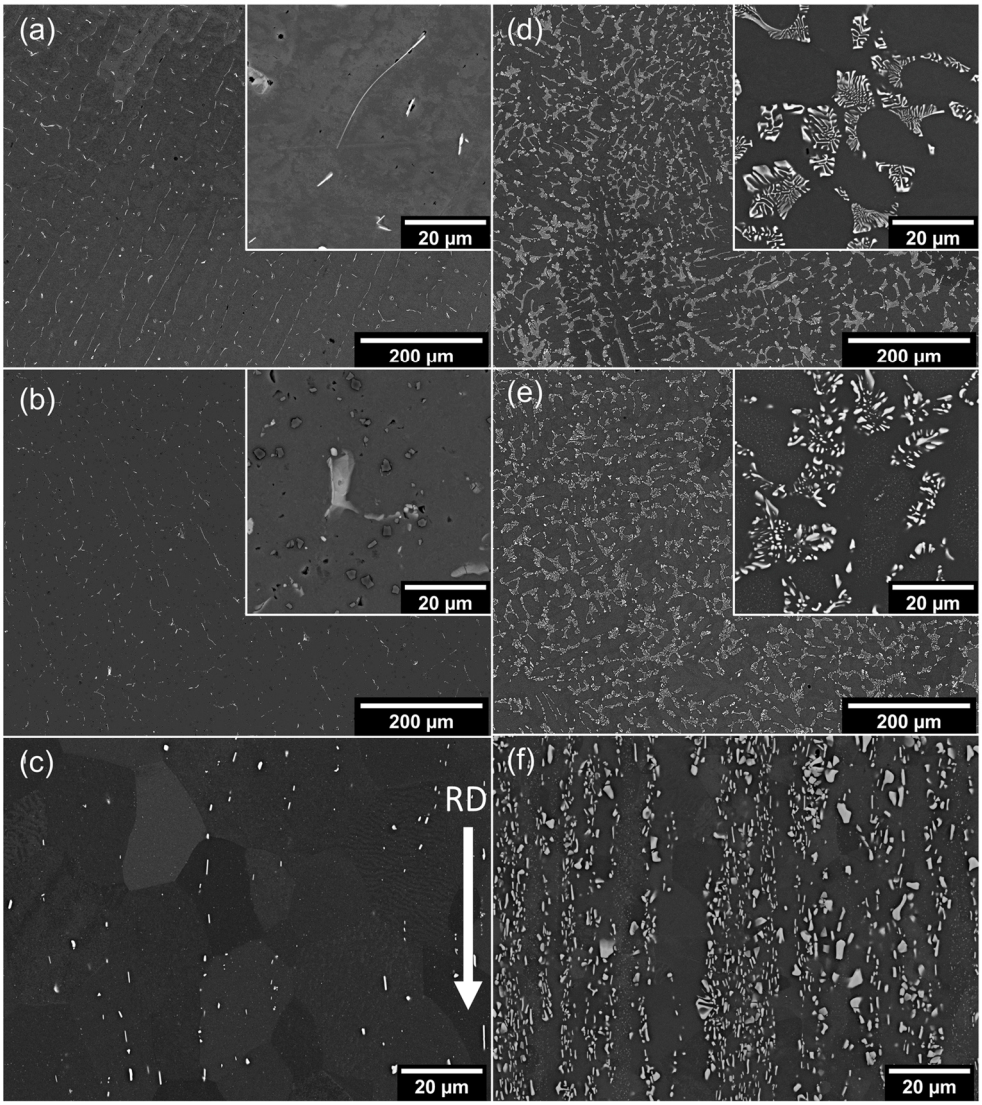

Figure 4-1: BSE micrographs of reference alloy 6016 (a-c) and alloy 6016+IMPs (d-f) in the conditions as-cast (a,d), homogenized (b,e) and solution annealed (c,f).

The secondary dispersoids after solution annealing exhibit a globular morphology with a size of about 112±48 nm (equivalent circular diameter) in alloy 6016+IMPs and 96±41 nm in reference alloy 6016. The high standard deviation results from the fact that the primary phases are fragmented to very different sizes as shown in Figure 4-1. The quantity of dispersoids in the experimental alloy 6016+IMPs is also much higher than in the standard 6016 alloy, because Mn also contributes to their formation [11,24]. Table 4-1 summarizes the most important microstructural features.

Table 4-1: Microstructural characteristics of reference alloy 6016 and the alloy 6016+IMPs after solution annealing.

IMPs	6016	6016+IMPs
Area fraction [%]	0.5	9.1
Mean equivalent circular diameter [nm]	650 ± 360	780 ± 495
Number of analysed particles [-]	817	10150
Dispersoids		
Area fraction [%]	0.02	0.10
Mean equivalent circular diameter [nm]	96 ± 41	112 ± 48
Number of analysed particles [-]	77	281
Grain size		
Average equivalent diameter [µm]	22.5 ± 10.4	6.9 ± 3.5
Mean aspect ratio [-]	1.76 ± 0.54	1.62 ± 0.45

Figure 4-2 illustrates the pronounced difference in microstructure between 6016 and 6016+IMPs. By means of EBSD, the crystal orientations were determined and plotted as inverse pole figure maps. Both alloys are completely recrystallized after the solution heat treatment. We attribute the refinement of the microstructure in the 6016+IMP variant to enhanced nucleation rate during recrystallization via particle stimulated nucleation (PSN) [15,25,26]. In the neighbourhood of IMPs an increased dislocation density is formed during rolling, creating favourable sites for the formation of recrystallization nuclei [15]. In parallel, the large number of interfaces (originating from both the IMPs and the dispersoids) hinders coarsening of the newly formed grains [25–29]. Consequently, the finest grains, with sizes below 5 µm, are found in areas of high particle density. New grains generated by particle stimulated nucleation have certain orientations, which are independent for each individual particle [25]. If PSN dominates the recrystallization process it induces more random orientations, which lead to a rather weak texture on the macroscale [25]. Both alloys exhibit a weak texture (6016, J-Index: 1.3536 and 6016+IMPs, J index: 1.3006); the only visible increase in orientation densities is the cube orientation rotated 45° around the normal direction (Euler angles 0°-45°-0° in Bunge convention). In 6016+IMPs this orientation is more pronounced. Figure 4-2 (b) (6016) and (d) (6016+IMPs) show the respective orientation distribution functions in the axis-angle space. In both cases, orientations of well over 3000 grains were evaluated.

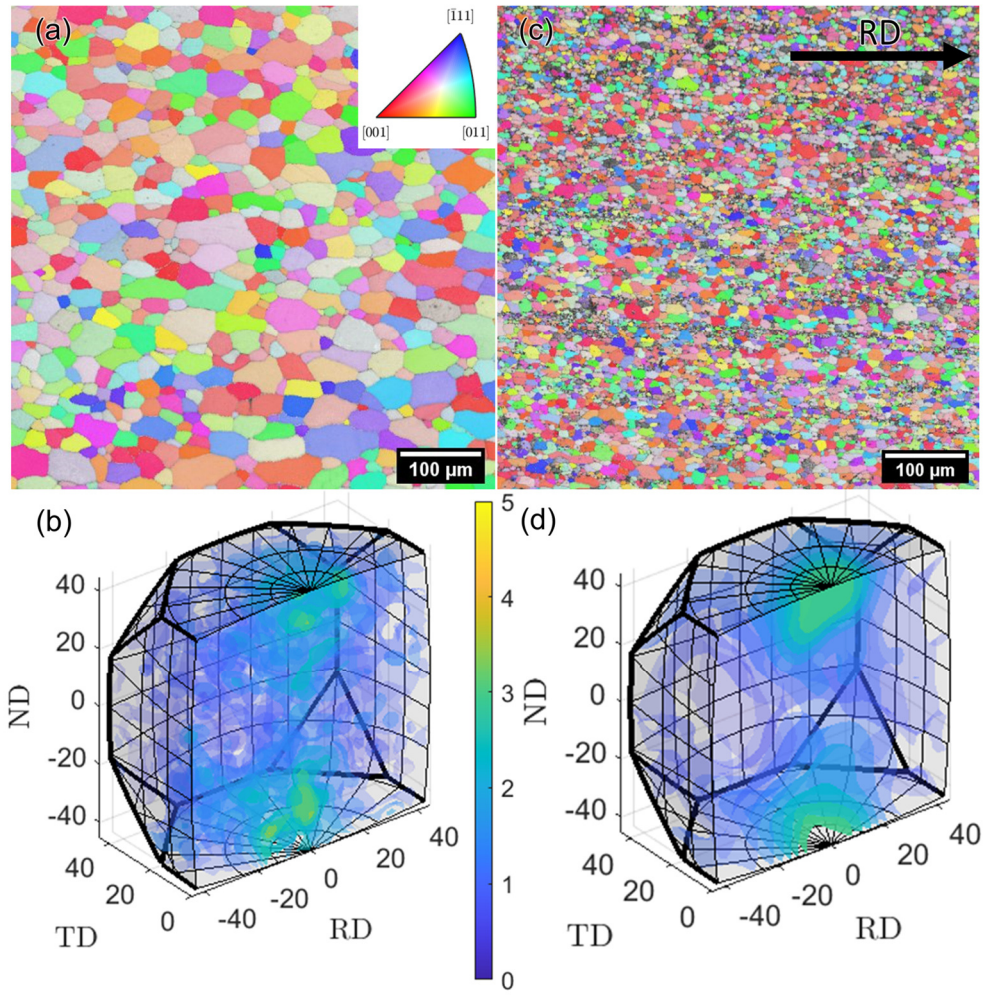

Figure 4-2: IPFZ maps (a, c) of the solution treated alloy sheets transverse to the rolling direction (RD) and the ODFs (b, d) of reference alloy 6016 (a, b) and alloy 6016+IMPs (c, d) in the axis/angle space.

Figure 4-3 presents the technical stress-strain curves from tensile tests of the 6016 and 6016+IMPs (values are given in Table 4-2). Two unique features are particularly striking: on the one hand the significantly higher strength values of alloy 6016+IMPs, and on the other its simultaneous surprisingly high total elongation of ≈ 25%.

We will first assess the higher strength values of alloy 6016+IMPs in both SHT and T4. Comparing the increase in yield strength from the solution-annealed condition (SHT) with T4, we notice that natural aging is about 11 MPa greater in alloy 6016+IMPs. Although the matrix composition upon solution treatment was adjusted via FactSage this may come about due to slight deviations in Mg and Si arising from the melting process or uncertainties in the FactSage simulation. The increase in yield strength of alloy 6016+IMPs of ≈ 38 MPa in SHT condition can be attributed to the interaction of multiple mechanisms. Increased solid solution hardening may have a small influence, but the contributions to strength increase result primarily from increased grain boundary hardening and the formation of geometrically necessary dislocations (GNDs), which can be assigned to hetero-deformation-induced (HDI) strengthening [19].

The increase in boundary hardening is quite obvious. For the refined grains in alloy 6016+IMPs (the grain size of 6.9 µm is significantly smaller than that of alloy 6016 with 22.5 µm), a yield strength increase of about 13.6 MPa is calculated according to Hall-Petch with a k_y of 80 MPa$\sqrt{\mu m}$ [30].

The HDI strengthening via the formation of GND is attributed to two key issues. Firstly, the difference in thermal expansion between the Al matrix and the IMPs, and secondly, the fact that the IMPs do not deform plastically. In both cases we apply Ashby's concept [31] and determine the number of dislocation loops, *n*, necessary to compensate for the geometric mismatch between matrix and IMPs.

We first consider the situation when quenching from the solution heat treatment temperature. With an IMP size of *d* and a difference in the coefficient of thermal expansion Δa between the Al matrix and the IMPs, we obtain the number of GNDs formed upon quenching according to $n = A\frac{\Delta\alpha\Delta T d}{b}$ [30]. With $\Delta a \approx 14\text{x}10^{-6}$ K^{-1} [32], b=0.29 nm (b Burgers vector of Al), A=3 for cube-shaped particles and ΔT= 540 K (quenching from 560°C to RT) one calculates 78 dislocations per intermetallic particle. Assuming a particle size of ≈ 1 µm and a volume fraction of ≈ 10 %, these dislocations are to be assigned to an area of ≈ 10 µm^2, which corresponds to a dislocation density ϱ of 7.8x10^{12} m^{-2}. Using the Taylor equation [33], $\sigma = \alpha G b\sqrt{\rho}$ (G shear modulus, 25.5 GPa; $\alpha \approx 0.6$) an increase in yield strength of approximately 12 MPa is calculated.

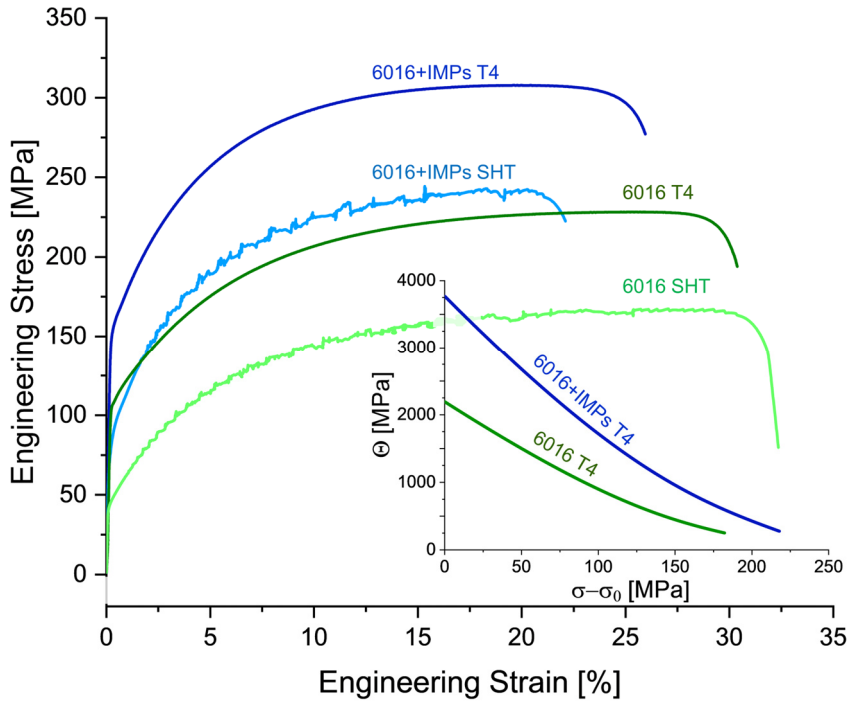

Figure 4-3: Engineering stress-strain curves for alloy 6016+IMP and reference alloy 6016 in as quenched (SHT) and T4 (16 days of natural aging) condition. The insert shows a "Kocks-Mecking plot" of the data [6016 and 6016+IMP], displaying the hardening rate in dependence on the true stress beginning at the yield point.

We now apply the concept of Ashby [31] to assess the stress increase caused by the presence of IMPs that do not deform plastically. First, we estimate the dislocation loops required to compensate for the volume difference resulting from the plastic deformation of the Al matrix compared to the undeformed IMPs. For cubic particles of size *d,* the number of geometrically necessary dislocations loops results in: $n = A\frac{\varepsilon d}{b}$ (ε amount of plastic deformation). Considering the volume fraction f_V of IMPs, the following relationship is obtained for the dislocation density: $\rho = \frac{8\varepsilon f_V}{bd}$. Now we consider that at the measured yield strength, $R_{p0.2}$, the material is 0.2% plastically deformed. With a particle size of 1 μm, a plastic deformation of 0.2% and a volume fraction of 10%, the GND density is calculated as ≈ 5.5×10^{12} m^{-2}. Using the Taylor equation, the corresponding increase in yield strength calculates to ≈10 MPa. Thus, all the individual contributions to the yield strength increase add up to a value of approximately 35.5 MPa, which is in good agreement with the measured values.

At this point we must note, that the formation of GNDs around rigid IMPs and the associated hardening is equivalent to increased strain hardening in the regime of plastic deformation. As shown in the insert to Figure 4-3 ("Kocks-Mecking plot"), the strain hardening is much more pronounced in 6016+IMPs. This can be illustrated by a simple example: A plastic deformation of 2% results in an additional flow stress increase in 6016+IMPs in T4 of approximately 30 MPa compared to 6016 (note the different slope of the σ–ε plot in Figure 4-3). Now we calculate the above example for increasing GND density caused by plastic deformation again, but now for 2% deformation. The result is a value of ≈ 5.5×10^{13} m^{-2}, which corresponds to a strength increase of 33 MPa. This increased strain hardening agrees quite well with the measured stress increase of 30 MPa. We thus conclude, in agreement with the literature [19,20], that the heterogeneous microstructure of alloy 6016+IMPs positively affects strength properties.

Table 4-2: Mechanical properties of alloys 6016 and 6016+IMP in the conditions T4 and SHT.

	6016 (SHT)	**6016 (T4)**	**6016+IMP (SHT)**	**6016+IMP (T4)**
$R_{p0,2}$ [MPa]	48 ± 1	110 ± 1	86 ± 1	159 ± 1
R_m [MPa]	167 ± 1	229 ± 1	246 ± 2	308 ± 1
A_g [%]	24.1 ±2.9	24.3 ± 1.1	17.6 ± 2.1	19.0 ± 0.6
A [%] *	32.2 ± 2.8	30.1 ± 1	21.8 ± 2.2	24.7 ± 1

We will now assess possible explanations for the remarkably good ductility, demonstrated by the appearance of necking strain and an elongation to fracture of approx. 25%. For this purpose, we first consider the kernel average misorientation (KAM, 1st order, step size 80 nm, threshold 5°) of the Al-matrix after applying a tensile strain of 25% for the 6016 and 6016+IMPs in T4 condition in Figure 4-4 (note: for 6016+IMPs this is close to the elongation to fracture). The KAM values can be seen as a measure of GND density or local misorientation. In graphical visualization the color range is

spanned between 0° and 1.2°; higher misorientation values are indicated with the brightest color. The areas detected as intermetallic particles are colored in red. If we compare the two structures, more lattice deformation (caused by GNDs) is observable in alloy 6016+IMPs, and it is preferentially concentrated around primary phases to accommodate the global strain. The KAM histograms also show that in line with the increased strain hardening discussed above, the distribution is broader and shifted to higher KAM values for alloy 6016+IMPs. It is also interesting to note that no zones of local deformation in the form of narrow shear bands are visible. Non-uniform deformation within such zones would lead to premature fracture due to the growth and coalescence of cavities [34]. Such cavities are generally caused by the cracking of coarse second-phase particles, especially Fe-rich IMPs with high aspect ratios [35], or the decohesion of the matrix from second-phase particles due to dislocation pile-up stresses at the particle-matrix interface [36]. In each of the possible cases, the small size and spherical morphology of the IMPs, as well as the small matrix grain size and the GND forest surrounding the particles, help to prevent the early formation of pores and thus failure.

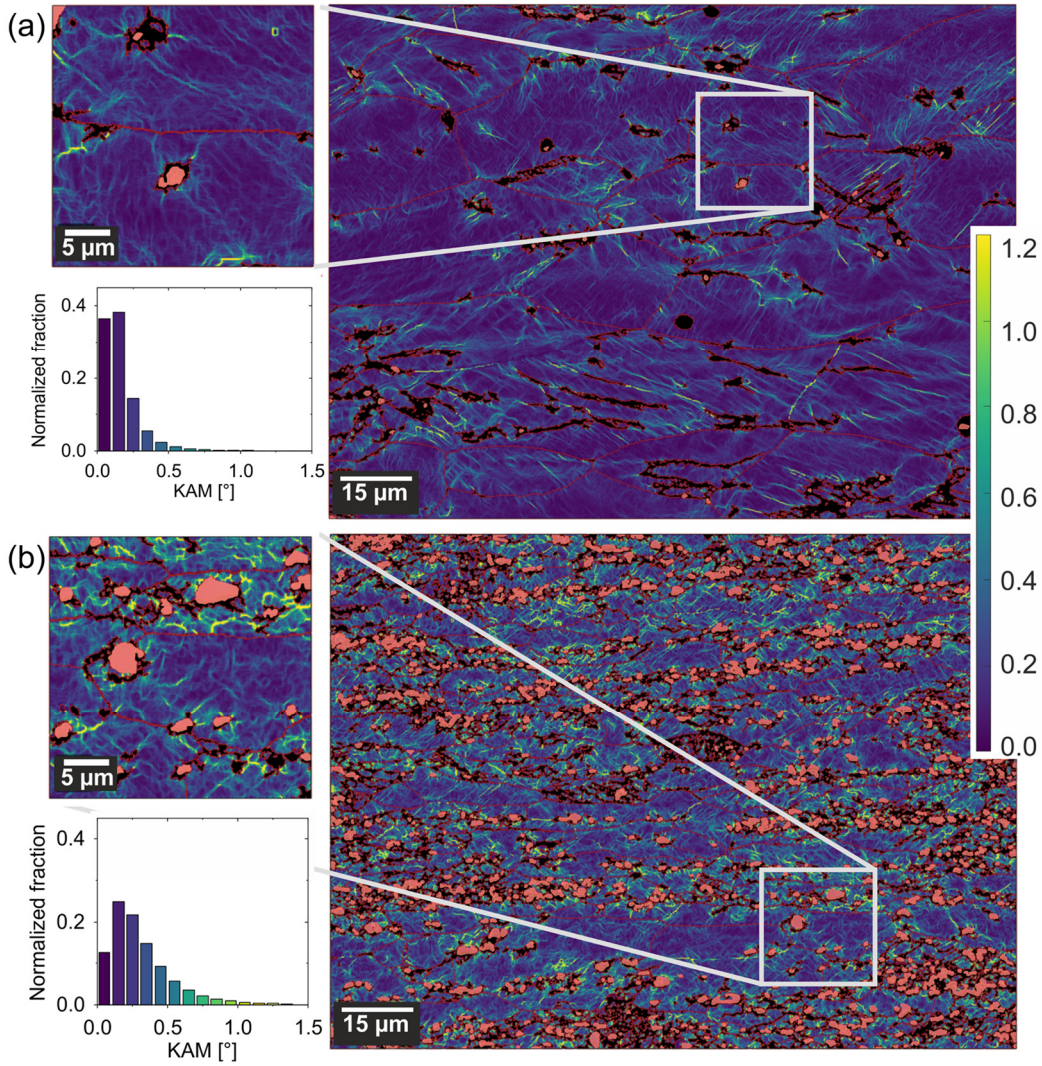

Figure 4-4: EBSD kernel average misorientation (KAM), grain boundaries >10° (red) and IMPs (red) of (a) alloy 6016 and (b) alloy 6016+IMPs after applying 25% strain. The insert shows a magnified section of the micrograph; the histograms quantify the distribution of the individual KAM values, with a shift to higher KAM for 6016+IMPs (total normalized fraction = 1).

In summary, a new Al-Mg-Si alloy system with a high fraction of Fe-rich primary intermetallic phases was created. We note that new wrought alloys containing tramp elements which exceed current standards have considerable potential. The positive effects of the emerging heterostructure comprise significantly smaller grains than those of reference alloy 6016, plus higher strength and higher strain hardening generated by the formation of geometrically necessary dislocations. The surprisingly high total elongation in tensile tests can be attributed to the effects of IMP refinement and morphology, grain refinement and a more uniform deformation. However, the morphological control of Fe-rich primary intermetallic phases through appropriate processing is crucial for the success of such a strategy.

4.4 References

[1] L. Zhang, J. Gao, L.N.W. Damoah, D.G. Robertson, Mineral Processing and Extractive Metallurgy Review 33 (2012) 99–157.

[2] J.A.S. Green, Aluminum Recycling and Processing for Engergy Conservation and Sustainability, A S M International, Materials Park, 2007.

[3] L.F. Mondolfo, Aluminium alloys: Structure and properties, Butterworth, London, Boston, 1979.

[4] S. Ji, W. Yang, F. Gao, D. Watson, Z. Fan, Materials Science and Engineering: A 564 (2013) 130–139.

[5] Z. Que, Y. Wang, Z. Fan, Metall Mater Trans A 49 (2018) 2173–2181.

[6] D. Wang, H. Zhang, H. Nagaumi, X. Li, J. Cui, Adv. Eng. Mater. 22 (2020) 2000517.

[7] M.A. Moustafa, Journal of Materials Processing Technology 209 (2009) 605–610.

[8] C.M. Dinnis, J.A. Taylor, A.K. Dahle, Scripta Materialia 53 (2005) 955–958.

[9] L. Lu, A.K. Dahle, Metall Mater Trans A 36 (2005) 819–835.

[10] N. Kuijpers, F.J. Vermolen, C. Vuik, P. Koenis, K.E. Nilsen, S. van der Zwaag, Materials Science and Engineering: A 394 (2005) 9–19.

[11] M.S. Remøe, K. Marthinsen, I. Westermann, K. Pedersen, J. Røyset, C. Marioara, Materials Science and Engineering: A 693 (2017) 60–72.

[12] S. Zajac, B. Hutchinson, A. Johansson, L.-O. Gullman, Materials Science and Technology 10 (1994) 323–333.

[13] S. Belmares-Perales, Met. Mater. Int. 14 (2008) 307–314.

[14] J. Grasserbauer, I. Weißensteiner, G. Falkinger, T.M. Kremmer, P.J. Uggowitzer, S. Pogatscher, Materials (Basel, Switzerland) 14 (2021) 3204.

[15] E. Aryshenskii, J. Hirsch, S. Konovalov, Metals 11 (2021) 507.

[16] N. Kuijpers, W.H. Kool, P. Koenis, K.E. Nilsen, I. Todd, S. van der Zwaag, Materials Characterization 49 (2002) 409–420.

[17] M. Lentz, G. Laptyeva, O. Engler, Journal of Alloys and Compounds 660 (2016) 276–288.

[18] L. Stemper, M.A. Tunes, R. Tosone, P.J. Uggowitzer, S. Pogatscher, Progress in Materials Science (2021) 100873.

[19] Y. Zhu, Metall Mater Trans A 52 (2021) 4715–4726.

[20] L. Lu, X. Wu, I.J. Beyerlein, Scripta Materialia 187 (2020) 307–308.

[21] F. Schmid, L. Stemper, T. Ebner, W. Leitner, S. Pogatscher, Proceedings of the EMC (2019) 639-652.

[22] R. Hielscher, H. Schaeben, J Appl Crystallogr 41 (2008) 1024–1037.

[23] J. Grasserbauer, I. Weißensteiner, G. Falkinger, S. Mitsche, P.J. Uggowitzer, S. Pogatscher, Materials (Basel, Switzerland) 13 (2020).

[24] Y. Wang, Y. Deng, Q. Dai, K. Jiang, J. Chen, X. Guo, Materials Science and Engineering: A 803 (2021) 140477.

[25] F.J. Humphreys, Acta Metallurgica 25 (1977) 1323–1344.

[26] O. Engler, J. Hirsch, Materials Science and Engineering: A 336 (2002) 249–262.

[27] M.X. Guo, J. Zhu, Y. Zhang, G.J. Li, T. Lin, J.S. Zhang, L.Z. Zhuang, Materials Characterization 132 (2017) 248–259.

[28] L. Yu, L. Chen, H. Wang, X. Wang, W. Peng, Y. Wang, L. Zhuang, Metall. Res. Technol. 117 (2020) 508.

[29] L. Yuan, M. Guo, K. Yu, J. Zhang, L. Zhuang, Philosophical Magazine 101 (2021) 1417–1442.

[30] P. Ebenberger, P.J. Uggowitzer, S. Kirnstötter, B. Gerold, S. Zaefferer, S. Pogatscher, Scripta Materialia 166 (2019) 64–67.

[31] M.F. Ashby, The Philosophical Magazine: A Journal of Theoretical Experimental and Applied Physics 21 (1970) 399–424.

[32] D. Ma, Journal of Applied Physics 124 (2018) 85109.

[33] G. Taylor, Proc. R. Soc. Lond. A 145 (1934) 362–387.

[34] H. Yamamoto, Conditions for shear localization in the ductile fracture of void-containing materials, Office of Scientific and Technical Information (OSTI), 1977.

[35] A. Bjurenstedt, E. Ghassemali, S. Seifeddine, A.K. Dahle, Materials Science and Engineering: A 756 (2019) 502–507.

[36] D. Broek, Engineering Fracture Mechanics 5 (1973) 55–66.

5 ASSESSMENT OF INDUSTRIAL APPLICABILITY BY APPLYING NEAR-INDUSTRIAL SOLIDIFICATION CONDITIONS

Previously, it has been shown that iron-rich IMPs can be effectively deployed to control the microstructure evolution by applying near-rapid solidification conditions and thermomechanical treatment. This resulted in improved mechanical properties observed for the high-Fe Al-Mg-Si alloy. The promising results obtained for the chosen alloy concept led to the creation of an alloy matrix to further evaluate the effects of the main elements (Fe, Si and Mn) that may influence the formation and morphology of primary IMPs. Since fast solidification conditions are subject to limitations in large-scale industrial application, it was necessary to prove the concept of industrial applicability by applying slower solidification conditions.

Even coarse IMPs formed during slow solidification upon direct chill casting can be sufficiently modified by conventional rolling and heat treatments. Similar to fast solidification conditions Fe-rich IMPs can be effectively deployed to positively influence grain size and final material properties. This section demonstrates that the underlying mechanisms are feasible in today's large-scale industrial processes. The results of the following research provide important insights into process-relevant factors and have been published in "Acta Materialia".

Processing and microstructure–property relations of Al-Mg-Si-Fe crossover alloys [4,5]

Authors' contributions

Bernhard Trink:	Conceptualization, Methodology, Investigation, Visualization, Writing – Original Draft.
Irmgard Weißensteiner:	Investigation, Visualization, Writing – Review & Editing.
Katharina Strobel:	Supervision, Writing – Review & Editing.
Anna Hofer-Roblyek:	Investigation, Writing – Review & Editing
Peter J. Uggowitzer:	Conceptualization, Writing – Review & Editing.
Stefan Pogatscher:	Project Administration, Conceptualization, Supervision, Writing – Review & Editing.

Acknowledgements

The authors wish to express their sincere thanks to AMAG Rolling for providing the material and for valuable discussions. This work was funded by the Christian Doppler Research Association within the framework of the Christian Doppler Laboratory for Advanced Aluminum Alloys. Financial support from the Austrian Federal Ministry for Digital and Economic Affairs, the National Foundation for Research, Technology and Development and the Christian Doppler Research Association is gratefully acknowledged.

Abstract

This study introduces new alloys, which combine the age-hardening capability of Al-Mg-Si alloys with the microstructure-controlling effect on processing of primary Fe-rich intermetallic phases used in foil stock. In detail, the processing and microstructure–property relations in new crossover aluminum alloys derived from 6xxx and 8xxx foil stock alloys, is shown. A highly Fe-rich intermetallic phase content was deployed to conceptually mimic high scrap content. Fast and slow solidification rates were applied to represent thin strip and direct chill casting, respectively. The effects of adding Fe and Mn to alloy 6016 were examined, while the Si consumed in primary phases was partly adjusted to maintain age-hardening potential. It was shown that upon thermomechanical processing, primary intermetallic phases in the new alloys are finely fragmented and well dispersed, resulting in strong grain refinement and a uniform texture. Attractive combinations of strength and ductility were

[4] B. Trink, I. Weißensteiner, P.J. Uggowitzer, K. Strobel, A. Hofer-Roblyek, S. Pogatscher, Acta Materialia 257 (2023) 119160.

[5] Note that parts of this work were also presented by the author in: B. Trink et al. (2023): Is there room for a little more?: How AMAG CrossAlloy.68 squeezes additional strength from 6xxx alloys and improves recycling, AluReport 03/2023, AMAG AG.

revealed, also in material processed under direct chill casting conditions. The new alloys' high elongation values of up to 30%, and their age-hardening response, were similar to those seen in commercial alloy 6016, while their strain hardening capacity was significantly greater. This can be attributed mainly to the formation of geometrically necessary dislocations near primary Fe-rich intermetallic phases. The study discusses microstructure refinement on the basis of particle stimulated nucleation. It uses a simple model to describe the individual contributions to yield strength, including the effect of primary phases. It also models the effect of these particles on increased strain hardening and ductility.

5.1 Introduction

Al-Mg-Si alloys (i.e. 6xxx alloys) form the basis of numerous age-hardenable wrought alloys and are used in a wide variety of product applications (rolled, extruded, forged and drawn). This is due to their excellent physical and chemical properties (medium to high strength, high fracture toughness, good weldability, corrosion resistance and formability) [1]. Over the last two decades these alloys have become increasingly important, particularly in the automotive industry, e.g. as body panels [2]. Formability and age-hardening upon paint baking are of great importance in 6xxx sheets [3]. One drawback of Al-Mg-Si alloys, however, is their low strain hardening capability, which is significantly worse than that of non-age-hardenable Al-Mg (5xxx) alloys and limits stretch formability [4,5]. One way to address this is to add age-hardening potential to 5xxx alloys via a crossover with 7xxx alloys [6].

It was recently shown to be possible in principle to increase the strain hardening of 6xxx series alloys by augmenting them with large amounts of Fe and by deploying near rapid solidification processing [7] (which, however, is subject to limitations in large-scale industrial application). High Fe content is typical of 8xxx foil stock alloys, which consist mainly of pure Al and large amounts of Fe (0.7-1.3 wt.% Fe for alloy AA 8079) [8]. An important function of Fe in 8xxx alloys is grain refinement, which is very important in foils to maintain formability at low foil thickness [8–10]. In contrast to the above-mentioned crossover approach involving 5xxx and 7xxx alloys [6], the aim here is to combine the positive properties of 6xxx alloy age hardening and 8xxx alloy microstructure control via primary intermetallic phases (hereinafter "IMPs") to achieve high strength and good formability. To ensure good formability, premature fracture due to the formation of microvoids must be avoided. In most cases, fracture of coarse, brittle intermetallic phases (Fe-phases) can deteriorate performance in forming processes such as bending [11,12]. However, even at very high Fe contents (up to 3 wt%), good bending performance in Al-Mg-Si alloys can still be achieved due to special processing [13]. A high proportion of iron-rich phases, which are more noble than the aluminum matrix, would be associated with a more pronounced corrosion phenomenon. However, since Al-Fe alloys exhibit satisfactory corrosion resistance [8,14], we do not expect major disadvantages in corrosion behavior for the crossover design due to high content of Fe-rich IMPs.

IMPs formed at low solidification rates, however, have also been reported to reduce ductility and negatively affect formability in wrought alloys [1,15–17]. In that context the highly diverse composition of aluminum scrap and consequently the introduction of IMPs makes recycling challenging. Fe poses a particular problem as it accumulates through the recycling of secondary aluminum and it is difficult to remove by metallurgical means [16,18]. An understanding of the impact of impurities, but also the capability to effectively work with impure elements to incorporate recyclability directly into alloy design, would be important assets in the effort to produce highly recycling-tolerant alloys. Coarse and rigid IMPs with a high aspect ratio are typical sites for damage initiation, which occurs via microcrack formation in the particle or decohesion of the matrix interface with the IMP [19,20]. The most important Fe-rich phases in aluminum alloys containing Si are α-AlFeSi and β-AlFeSi [16]. The α-phase, as a primary phase, can form a coupled Al-α-AlFeSi eutectic with a convoluted arm structure or a blocky polyhedral crystal, producing a roughly hexagonal shape in cross-section [21] if it forms before the aluminum dendrites begin to solidify [15,21,22]. Cooper [23] and Skjerpe [24] confirmed a cubic crystal structure in the α AlFeSi phase. The β-phase, which exhibits a monoclinic crystal structure [15], is characterized by a platelet morphology [21], which can form a network through the impingement of individual platelets during growth [15,16,21]. With respect to mechanical properties in the as-cast condition, the α-phase is preferred because it features a more favourable morphology [16,25].

Several strategies are deployed to control the morphology of iron-rich IMPs. Alloying elements can be used to supress the formation of the long-needle shaped β-phase and promote the development of fine-branched α-AlFeSi [16,25]. Manganese is the most frequently used alloying element acting as an "Fe-corrector" [16,25–29]. Fast solidification (> 10 K/s) also promotes the beneficial formation of refined α AlFeSi instead of β AlFeSi, with a higher solidification rate needed at greater Fe-content [16,30,31]. Casting processes featuring fast solidification, i.e. twin roll casting technology [13], can therefore also be deployed to prevent the formation of coarse intermetallic particles which allow a high Fe-content. Fe-rich IMPs can also be partially dissolved [32], fragmented [31,33] and converted into rounder shapes [8] using heat treatments. Homogenization in a temperature range between 530°C and 600°C triggers the transformation of plate-shaped β particles into globular α-particles [8,26,33,34].

This study shows that upon thermomechanical processing Fe-rich IMPs can be effectively deployed to positively influence grain size and final material properties, and that they can serve as a demonstration example for improved recyclability. Even coarse IMPs, which form during slow solidification upon direct chill casting, can be fragmented to a sufficient extent by conventional rolling mainly depending on the forming degree and used to control the microstructure evolution in an Al-Mg-Si-Fe crossover alloy. This significantly increases the strain hardening capability of these alloys, while keeping their age-hardening potential high.

5.2 Experimental

To synthesize the alloys used in this study, the alloy EN-AW 6016, which served as a reference, was remelted, and Mn (75% Mn and 25% Al reagent), Fe (75% Fe and 25% Al reagent) and Si (100% Si reagent) were added via master alloys (contents in wt.%). Table 5-1 provides the chemical compositions of the experimental alloys determined by optical emission spectrometry.

Table 5-1: Chemical compositions of the test alloys (contents in wt.%).

Alloy	Si [%]	Fe [%]	Mn [%]	Mg [%]	Description
Ref.6016	1.09	0.19	0.06	0.33	Reference alloy
Si-adapted					
0.8Fe0.1Mn1.5Si	1.47	0.86	0.07	0.32	↑Fe
0.8Fe0.5Mn1.6Si	1.60	0.87	0.52	0.34	↑Fe ↑Mn
1.5Fe0.1Mn2.0Si	1.98	1.55	0.10	0.31	↑↑Fe
1.7Fe1.2Mn2.3Si	2.28	1.70	1.25	0.34	↑↑Fe ↑↑Mn
Si constant at 1.1 %					
0.8Fe0.1Mn1.1Si	1.11	0.80	0.07	0.33	↑Fe
0.8Fe0.5Mn1.1Si	1.14	0.82	0.52	0.32	↑Fe ↑Mn
1.5Fe0.1Mn1.1Si	1.16	1.52	0.10	0.33	↑↑Fe
1.7Fe1.2Mn1.1Si	1.11	1.63	1.20	0.33	↑↑Fe ↑↑Mn

In addition to the increase in Fe and Mn, Si content was intentionally increased to account for its incorporation into the IMPs and to allow an equal amount of dissolved Mg and Si in each alloy at the solution treatment temperature (calculated using FactSage 8.0 database FTlite 2022). All alloys, including the reference, were subjected to the same process conditions. The reference alloy 6016 experienced only fast solidification.

As described in [35], to simulate the industrial solidification rate in a continuous casting process, a resistance heated tilting furnace (Nabertherm K20/13/S) was charged with clean EN-AW 6016 scrap material of known composition and the elements Si, Fe and Mn were added. After the addition of AlTi5B1 as an inoculant to improve the solidification condition, Ar-degassing was carried out to get rid of dissolved gases and solid particles. At a casting temperature of 760°C the melt was poured into a pre-heated steel mould (pre-heated to ~ 250°C) to produce ingots weighing approximately 8 kg. An ionic liquid served as a cooling medium, using a heat exchanger. This resulted in a cooling rate of ≈ 3°C/s, which is comparable to the cooling rate of a continuous casting process. To achieve a fast solidification rate, an induction furnace (INDUTHERM MC100V) was deployed to remelt the previously synthesized alloys, after which they were cast into a rectangular copper mould at room temperature (RT) as defined in [35] (cooling rate ≈ 60°C/s, capacity 100g) at a casting temperature

of 760°C. After the casting process, a homogenization treatment at 560°C with a heating period of 8h was conducted (average heating rate 1.125 °C/h), followed by a holding time of 11h. The rolling process involved hot-rolling with a laboratory rolling mill from 12mm to 7.3mm and subsequent cold-rolling to 1.2mm sheet thickness, with intermediate annealing at 560°C for 25 minutes at 3.1mm. The final alloy sheets were solution annealed at 560°C for 2 minutes using a contact press, with subsequent quenching in water at RT.

To evaluate the mechanical properties of the test alloys, tensile tests were carried out after 14 days of natural aging at RT using a Zwick/Roell Z 100 model tensile testing machine at a strain rate of 0.0032 s-1, with a gauge length of 45 mm in the rolling direction. To analyze the microstructure, cross-section planes of the sheet material, including rolling (RD) and normal (ND) direction, were prepared using standard metallographic procedures and examined under a scanning electron microscope (SEM) of type JEOL-7200F. The IMPs were assessed as to size and distribution using the ImageJ software package. Electron backscatter diffraction (EBSD) was carried out with a Symmetry S2 detector from Oxford Instruments. The data generated were analyzed using the Aztec Crystal software package and the mtex toolbox [36]. X-ray diffraction (XRD) was performed with a Bruker-AXS D8 Advance diffractometer, operated with CuKα radiation. The measurements were made using Bragg-Brentano geometry in a range between 20-120° with a step size of 0.02°.

5.3 Results

5.3.1 Microstructure evolution during thermomechanical treatment

Figure 5-1 depicts backscattered electron (BSE) micrographs of the test alloys in as-cast condition for both solidification rates. Significant differences in the morphology of primary phases can be seen. At fast solidification rates the IMPs show a fine lamellar structure in all test alloys which resembles that of an Al-α-AlFeSi eutectic network (Figure 5-1 fast cooling rate). This fine-branched morphology arises from a coupled growth mechanism initiated by a eutectic reaction with the α-Al-phase [21,37]. The lamellar morphology indicates the α-Al(Fe,Mn)Si-phase [16,21,38]. Alloying with Mn resulted in more fine lamellae, while an increase in Fe content produced a coarser morphology and a higher volume fraction of IMPs (Figure 5-1 fast cooling rate, alloy 1.5Fe0.1Mn2.0Si). Primary Si or Mg2Si could not be detected in any of the alloys.

At slow solidification rates the primary IMPs formed are much larger in size and show lamellar and elongated structures (Figure 5-1 slow cooling rate), indicating α-AlFeSi- and β-AlFeSi-phase [21,37], which are located interdendritically. Another large IMP shape can be seen only in alloys with simultaneously high Fe and Mn content, i.e. 1.7Fe1.2Mn2.3Si and 1.7Fe1.2Mn1.1Si, which feature

compact, facetted polyhedral morphologies with diameters of ≈ 75±25 µm (Figure 5-1 slow cooling rate, alloy 1.7Fe1.2Mn2.3Si).

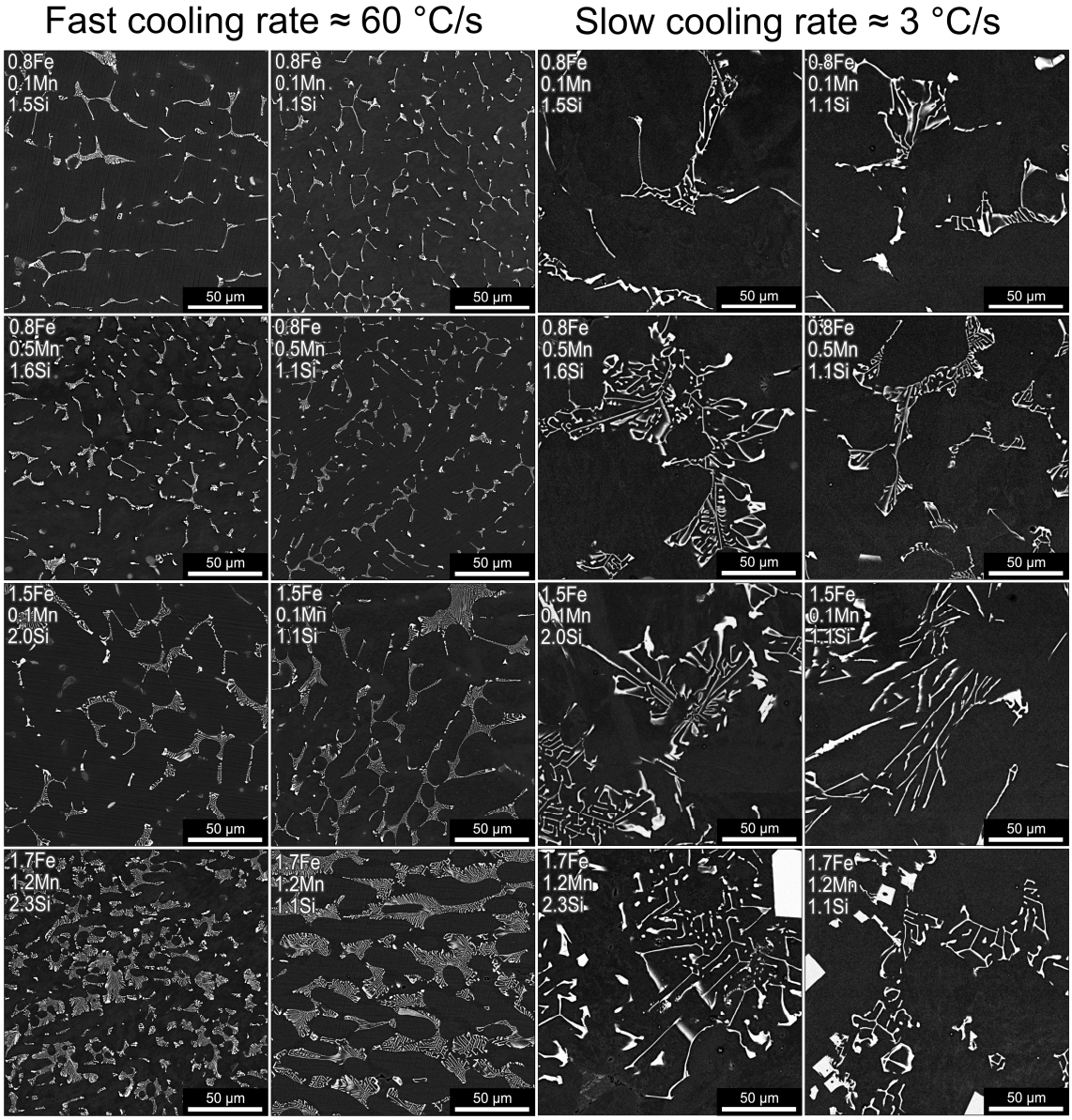

Figure 5-1: BSE micrographs of the test alloys at fast (≈ 60°C/s) and slow (≈ 3°C/s) cooling rates in as-cast condition (directional solidification, central ingot area).

The primary phases are very strongly modified by thermomechanical processing, as the depiction of alloy 1.7Fe1.2Mn2.3Si at both solidification rates in Figure 5-2 shows. The homogenization treatment, followed by hot rolling of the fast solidified alloys, produced a morphological modification of the previously fine lamellar structures. In addition to slight coarsening of the intermetallic phases, fragmentation into individual particles took place; this was also demonstrated in our previous work [7]. Elongated primary phases broke into individual particles and plate-like iron-rich phases assumed a more spherical morphology. A comparable morphological modification was also achieved in the slowly solidified variants after homogenization and hot rolling. Only the compact, faceted particles (sludge) of alloys 1.7Fe1.2Mn2.3Si and 1.7Fe1.2Mn1.1Si showed no significant changes in

morphology. Cold rolling induced further distinct changes in the morphology of primary IMPs. The iron-rich intermetallic phases underwent drastic fragmentation, which is apparent at both solidification rates. Thus, the actual comminution of the iron-rich phases by the deformation process takes place during cold rolling. Even the coarse faceted AlFeSi-phases are partially fractured by the rolling process, as can be seen in Figure 5-2 after cold rolling. At the end of the rolling program, a finely distributed structure of primary phase particles is present. Exceptions here are, again, alloys 1.7Fe1.2Mn2.3Si and 1.7Fe1.2Mn1.1Si at slow solidification rates, in which many of the polyhedral particles could not be crushed entirely.

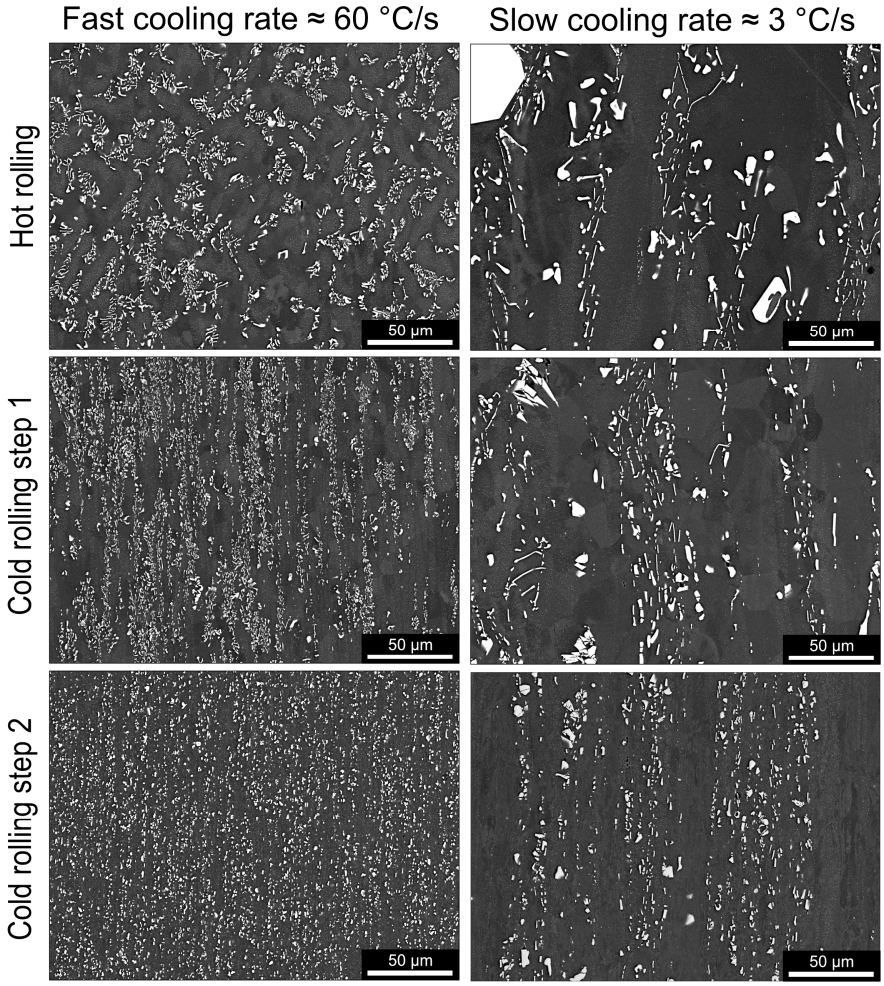

Figure 5-2: Morphological transformation of iron-rich intermetallic phases during the rolling process shown using alloy 1.7Fe1.2Mn2.3Si at fast (≈ 60°C/s) and slow (≈ 3°C/s) cooling rates (cross-section planes including RD- and normal ND-direction, central sheet area).

Figure 5-3 illustrates the morphology of primary phases after solution heat treatment. For all alloys and solidification rates (except for alloys 1.7Fe1.2Mn2.3Si and 1.7Fe1.2Mn1.1Si at slow solidification rates) a thorough fragmentation of IMPs into fine particles was achieved. During the deformation process the particles arrange themselves in the rolling direction, forming chain-like structures. When fast solidified, alloy 1.7Fe1.2Mn2.3Si showed an impressive homogeneous distribution, high area fraction and roundish morphology on the part of IMPs. This already indicates interesting mechanical properties similar to those revealed in our previous work [7]. Because Mn has already generated a

finer as-cast primary phase structure, the same thermomechanical treatment results in smaller comminuted IMP sizes in the final sheet condition. XRD analysis was performed on the slowly solidified alloys in T4 condition. While β-AlFeSi peaks are still found in the XRD diffractogram of the low-Mn variants (see Figure 5-4), based on morphological considerations, it is likely that branched α-Al(Fe,Mn)Si is the main iron-rich phase in the high-Mn alloys.

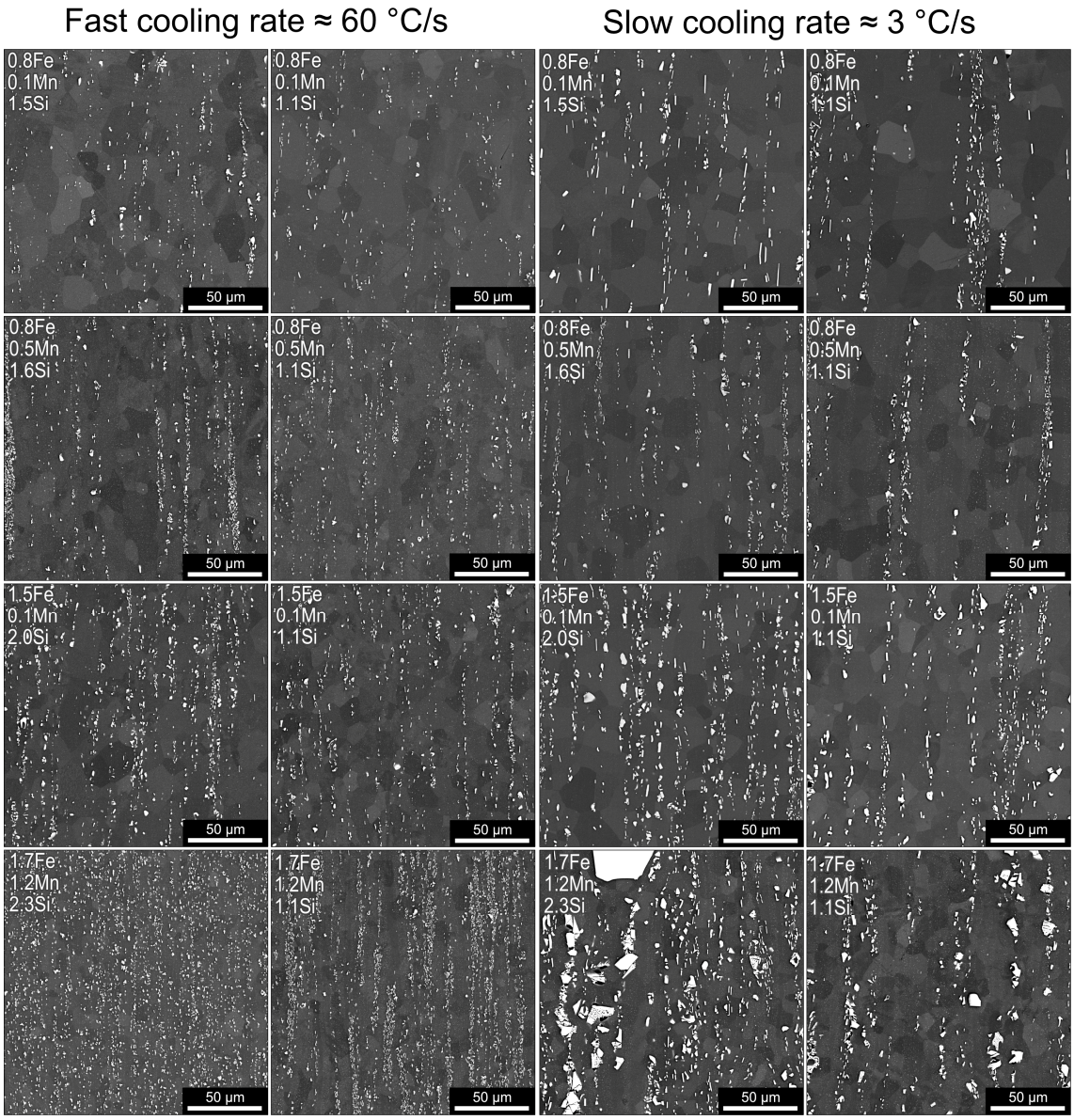

Figure 5-3: BSE micrographs of the test alloys (cross-section planes including RD- and normal ND-direction, central sheet area) at fast (≈ 60°C/s) and slow (≈ 3°C/s) cooling rates in T4 condition (after solution annealing and 14 days of natural aging).

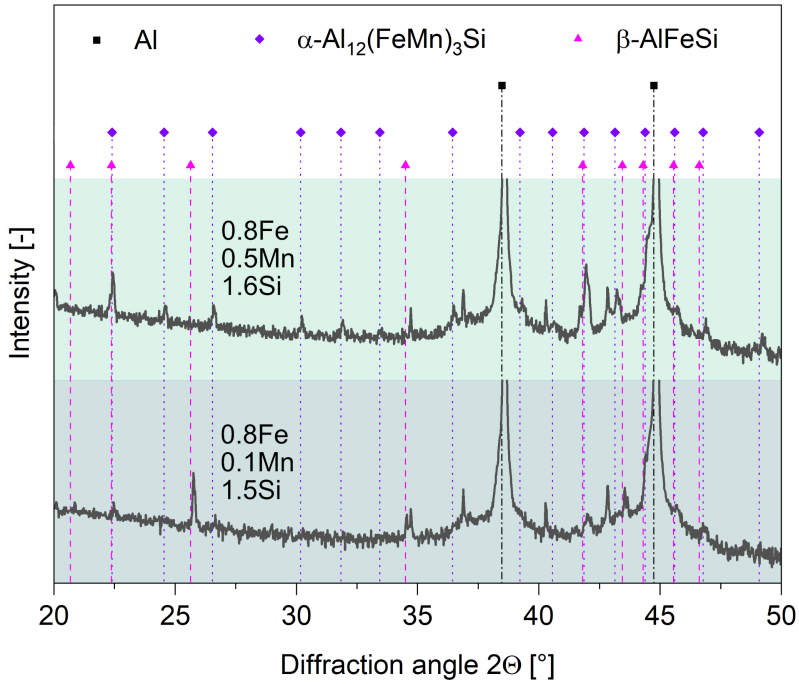

Figure 5-4: XRD diffractogram of slowly solidified 0.8Fe0.1Mn1.5Si and 0.8Fe0.5Mn1.6Si in T4 condition. The peak positions of α-Al12(FeMn)3Si and β-AlFeSi (measured values) were obtained from [39].

Figure 5-5 shows the size distribution and area fraction of the primary phases for a) fast and b) slow solidification rates. Fast solidification generates finer primary phases, which fragment into even smaller particles during thermomechanical treatment. The size distribution of IMPs is narrower for the alloys solidified at a high rate. Nevertheless, after thermomechanical processing the morphology of the slowly solidified IMPs is also surprisingly fine. They exhibit an average size of 1–2µm, compared to a size of slightly below 1µm for fast solidification. The area fraction, f_A, of IMPs of the alloys studied in this work is, at $2 < f_A\,[\%] < 9$, much larger than the reference 6016 ($f_A \approx 0.5\%$) and increases with increasing Fe- and Mn-content. The high standard deviation of the area fraction of alloys 1.7Fe1.2Mn2.3Si and 1.7Fe1.2Mn1.1Si results from the inhomogeneous distribution of coarse IMPs (sludge), which are not crushed completely during the rolling process.

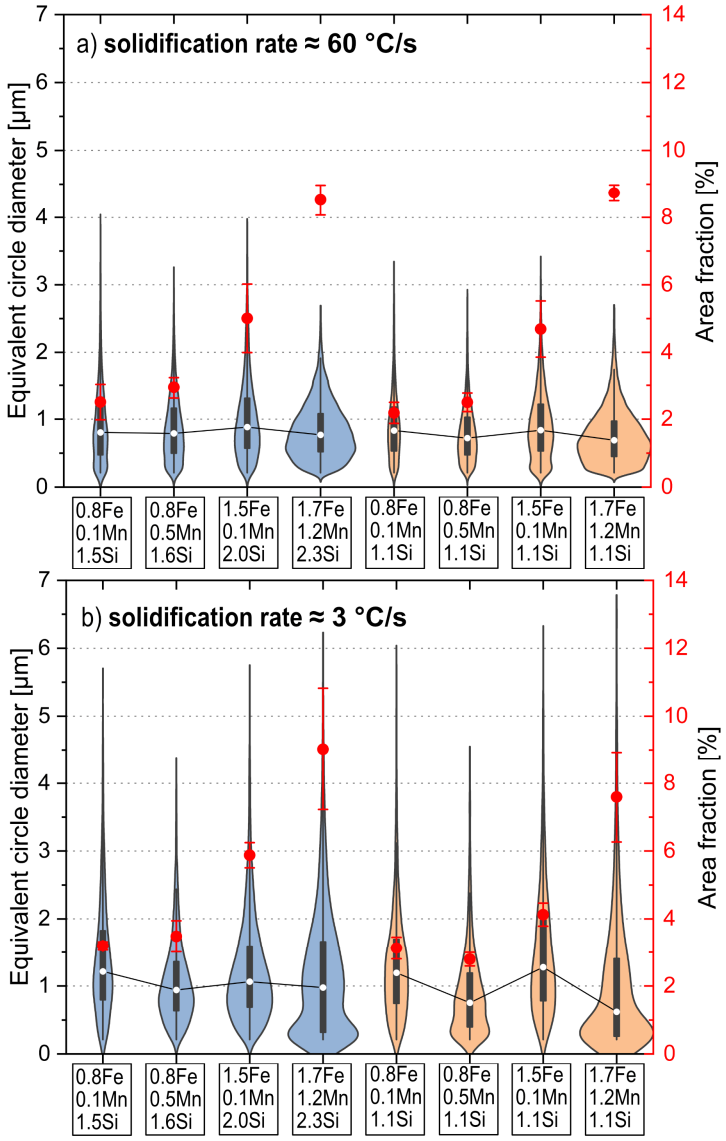

Figure 5-5: Particle size distribution and area fractions of the iron-rich intermetallic phases of the test alloys at a) fast (≈ 60°C/s) and b) slow (≈ 3°C/s) cooling rates in T4 condition (area surveyed ~0.2 mm²)

During homogenization annealing dispersoids are precipitated secondarily [40]. Figure 5-6 shows BSE micrographs of these AlFeSi-dispersoids in alloy 0.8Fe0.5Mn1.6Si under both solidification conditions. The difference in solidification rate should not cause significant changes in distribution, morphology or volume fraction, because these attributes are controlled largely by the homogenization treatment [41–44]. Nonetheless, a higher alloying element content would be expected to generate a higher dispersoid density during fast solidification; this was also reported in [45] for another Al system. Manganese as an alloying element generates an increase in the area fraction, as well as coarser dispersoids [1,44]. A reduction in the Si-content dissolved in solid solution (alloys with 1.1 wt.% Si) seems to reduce the sizes of the dispersoids formed. To avoid the inclusion of finely fragmented primary phases, which are still larger [7], in the evaluation of the dispersoids, only particles with equivalent circular diameters <200 nm were analyzed (most AlFeSi-dispersoids have sizes of 50–200 nm [46]). Dispersoid evaluation results are summarized in Table 5-2.

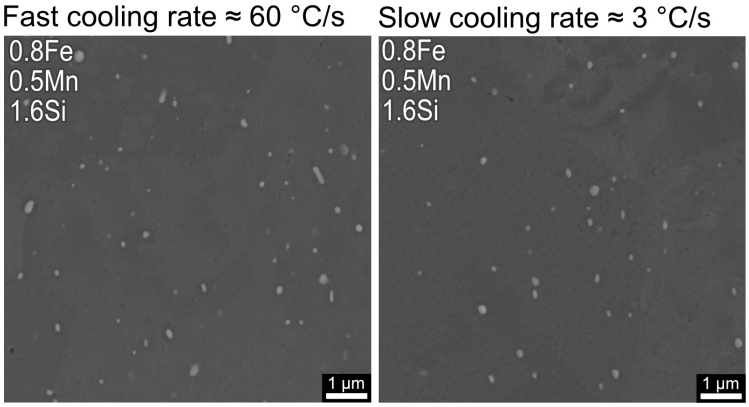

Figure 5-6: Comparing dispersoids for alloy 0.8Fe0.5Mn1.6Si at fast (≈ 60°C/s) and slow (≈ 3°C/s) cooling rates in T4 condition.

Table 5-2: Evaluation of the dispersoids of the alloys for fast solidification (area surveyed ~ 325 µm²).

Alloy	**Mean equivalent circular diameter, d_d [nm]**	**Area fraction, f_d [%]**
EN-AW 6016	98±44	0.2
0.8Fe0.1Mn1.5Si	103±46	0.26
0.8Fe0.5Mn1.6Si	105±45	0.64
1.5Fe0.1Mn2.0Si	95±38	0.21
1.7Fe1.2Mn2.3Si	115±49	1.02
0.8Fe0.1Mn1.1Si	81±40	0.31
0.8Fe0.5Mn1.1Si	95±44	0.74
1.5Fe0.1Mn1.1Si	71±33	0.33
1.7Fe1.2Mn1.1Si	89±40	0.82

Figure 5-7 shows the microstructure of the test alloys after solution annealing, as obtained by combined EBSD and EDX analysis. The grain colors represent the equivalent circle diameter (ECD) [47]; brighter colors (yellowish) indicate a greater ECD. By superimposing the EDX signal, the fragmented IMPs are shown in red. All alloys are completely recrystallized after solution annealing. Since the rate of solidification influences the size of the IMPs formed and thus the final size of fragmented IMPs, there is also a dependence on the final grain size. The alloys which experienced a slow solidification rate show bigger grains overall compared to the fast solidified variants. A higher iron-rich intermetallic phase content generates smaller grains, the finest of which (< 5µm) are formed in the high-particle-density environment. Multiple fine equiaxed grains in areas of high IMP density and adjacent coarser grains can also be observed.

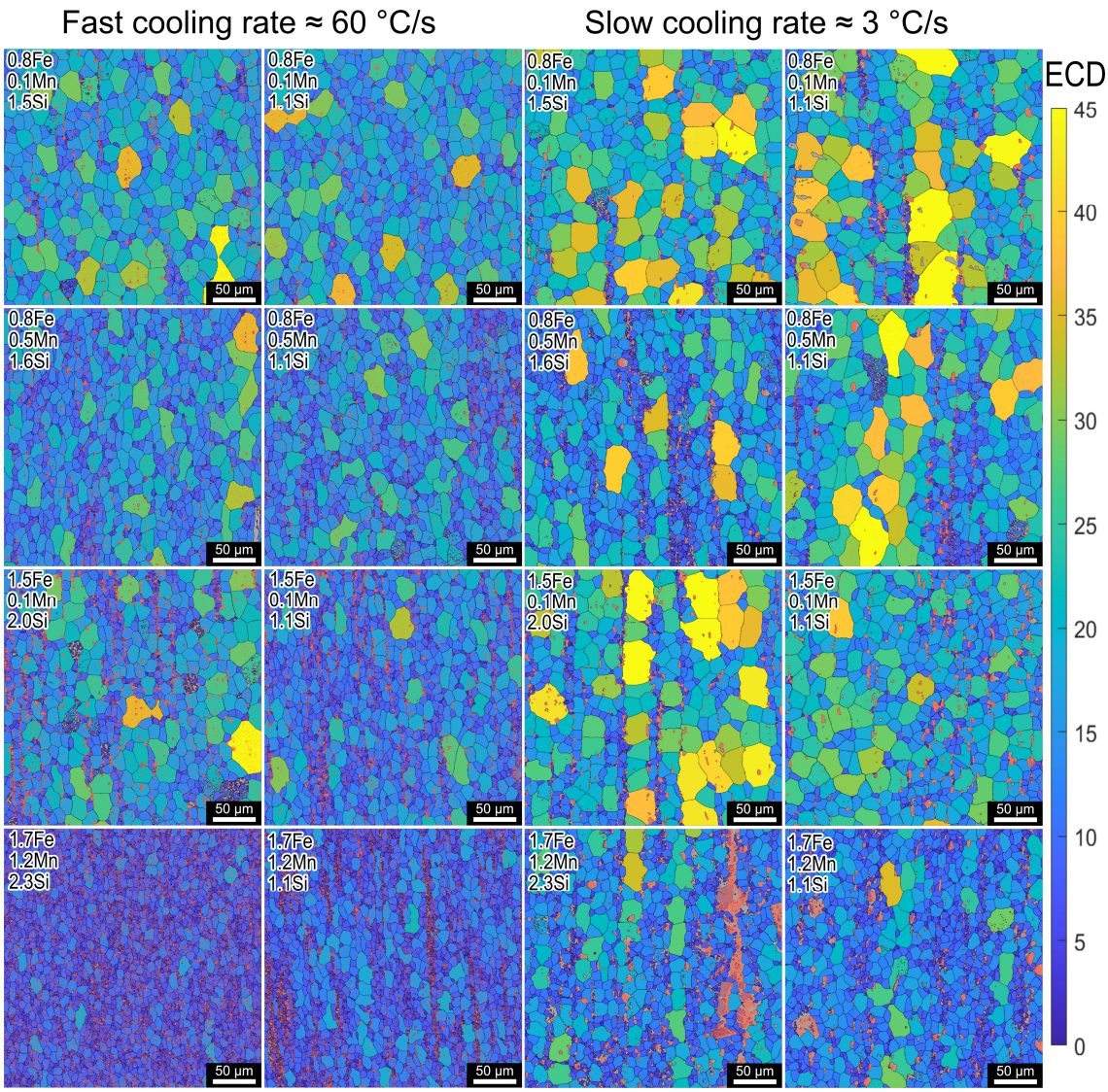

Figure 5-7: EBSD-ECD maps of the new alloys (cross-section planes including RD- and normal ND-direction, central sheet area) at fast (≈ 60°C/s) and slow (≈ 3°C/s) cooling rates in T4 condition.

Figure 5-8 shows the evaluation of grain sizes via the maximum length of the grains in x (=RD) and y (=ND) directions (step size 0.8µm, grain boundary misorientation mid. 5°, min. pixel criterion 3, excluding primary phase particles). At greater IMP content, the grains reduce in size. The smallest grains form in areas of the highest particle density, and the alloys with the highest volume fraction of iron-rich phases benefit most from the grain refining effect. Alloy 1.7Fe1.2Mn2.3Si, fast solidified, features the finest grains, with an average ECD of 5.4µm. This represents refinement by a factor of 4 compared to reference alloy 6016 (average ECD of 23.8µm).

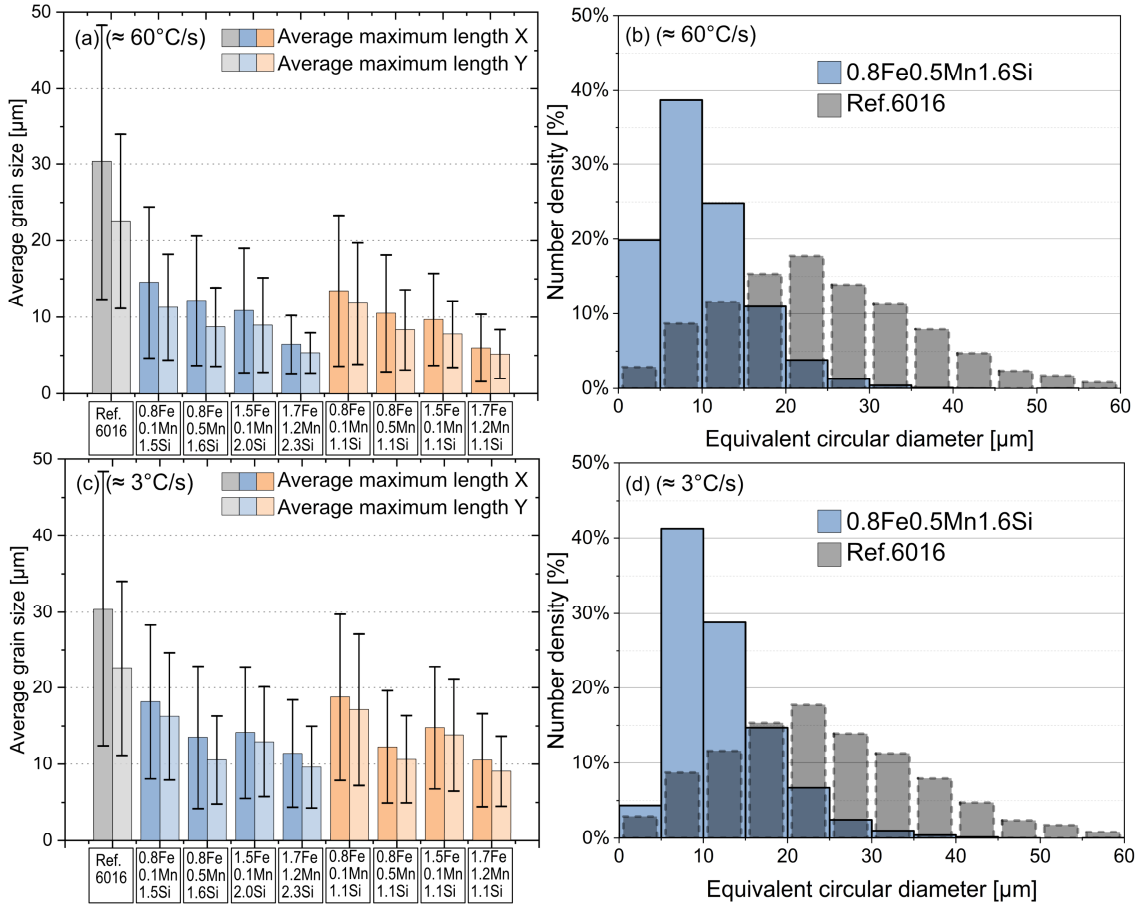

Figure 5-8: Average grain sizes of the test alloys in comparison with reference alloy EN-AW 6016 at (a,b) fast (≈ 60°C/s) and (c,d) slow (≈ 3°C/s) cooling rates in T4 condition

The processing of the material (including intermediate annealing) and the increased amount of primary and secondary particles produce a generally weak texture in the alloys analyzed (ODF maps are presented in Figure 5-13 of the appendix). The J-index of the calculated ODFs (determined as in [48], kernel halfwidth = 7°) are below 1.32 in all cases. In the slowly cooled alloys the texture is weaker in alloys lacking additional Si, but the characteristics remain similar.

The dominant texture component (within the weak textures) is the rotated Cube (45° in ND, {001]<110>), because the grains seem to grow easiest in this orientation. As mentioned earlier, the 0.8Fe0.1Mn1.5Si and 0.8Fe0.1Mn1.1Si alloys exhibit the largest grain sizes due to the lowest grain-growth inhibition of intermetallic particles. An orientation-dependent grain size analysis revealed the largest relative grain size in the rotated cube orientation, especially in those alloys that show a more bimodal grain size distribution. In all alloys, the rotated Cube orientation shows the highest relative number of grains (assessment from EBSD data; criterion for min. grain size = 0.64µm²). One exception to the orientation distribution is the fast cooled 1.7Fe1.2Mn1.1Si alloy (see also Figure 5-13 of the appendix). Here an increased number of (large) grains are oriented in the Cube orientation.

5.3.2 Mechanical properties

Figure 5-9 shows the results of tensile tests on all experimental alloys after 14 days of natural aging (T4). Upon fast solidification, all alloys with adjusted Si content show increased strength accompanied by only slightly reduced elongation. Alloy 1.7Fe1.2Mn2.3Si, with the highest IMP content, exhibits the greatest strength, together with surprisingly high total elongation of > 25%. Compared to reference 6016, all Fe-rich alloys also exhibit significantly greater work hardening. Alloys to which no additional Si was added to compensate for the Si trapped in the IMPs showed similar yield and tensile strengths, paired with somewhat lower total elongation with rising IMP content. An exception is alloy 1.7Fe1.2Mn1.1Si, which exhibits a somewhat lower strength level.

Upon slow solidification, alloys with additional Si show a very similar trend towards higher strength with increasing IMP amounts. The alloys exhibit an attractive combination of strength and ductility, as well as increased strain hardening. It is noteworthy that the ductility is not affected by the high iron content, which suggests successful optimization of the microstructure and primary phase fragmentation. Alloys 0.8Fe0.1Mn1.5Si and 0.8Fe0.5Mn1.6Si, in particular, demonstrate extraordinarily high total elongation, similar to the reference alloy 6016, despite the increased strength. Because the stress-strain curves of the fast and slowly solidified variants show no striking differences, it may be concluded that the concept of microstructure control by morphological transformation of Fe-rich IMPs is not restricted to fast solidification. Alloys 1.7Fe1.2Mn2.3Si and 1.7Fe1.2Mn1.1Si after slow solidification are an exception, because the large polyhedral IMPs could not be crushed entirely (see Figure 5-3). It should be mentioned that inhomogeneous distribution of these faceted and coarse primary phases (see Figure 5-1) generate higher scatter of the tensile test data for alloys 1.7Fe1.2Mn2.3Si and 1.7Fe1.2Mn1.1Si after slow solidification (see Table 5-5 for mechanical properties in the appendix).

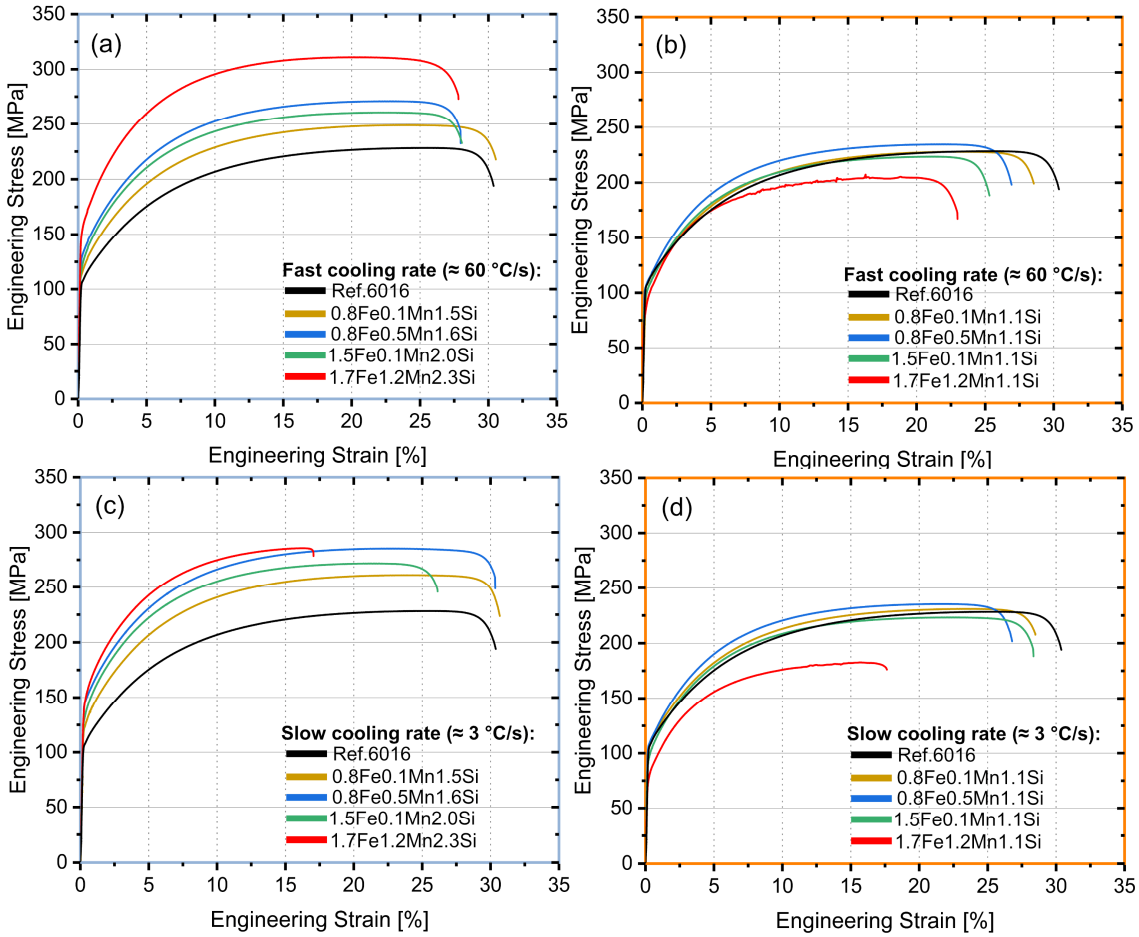

Figure 5-9: Technical stress-strain curves of the test alloys for (a,b) fast and (c,d) slow solidification conditions after 14 days of natural aging.

Because artificial aging is an essential part of alloy design, the test alloys were artificially-aged for 5h at 185°C. This resembles the peak-age condition for reference alloy 6016 [49]. Figure 5-10 displays the engineering stress-strain curves after artificial aging. The age-hardening response does not depend significantly on the solidification conditions. Apart from alloy 1.7Fe1.2Mn1.1Si (weakest increase in yield strength) all alloy systems show a significant increase in strength due to age hardening, which is comparable to that of the reference 6016.

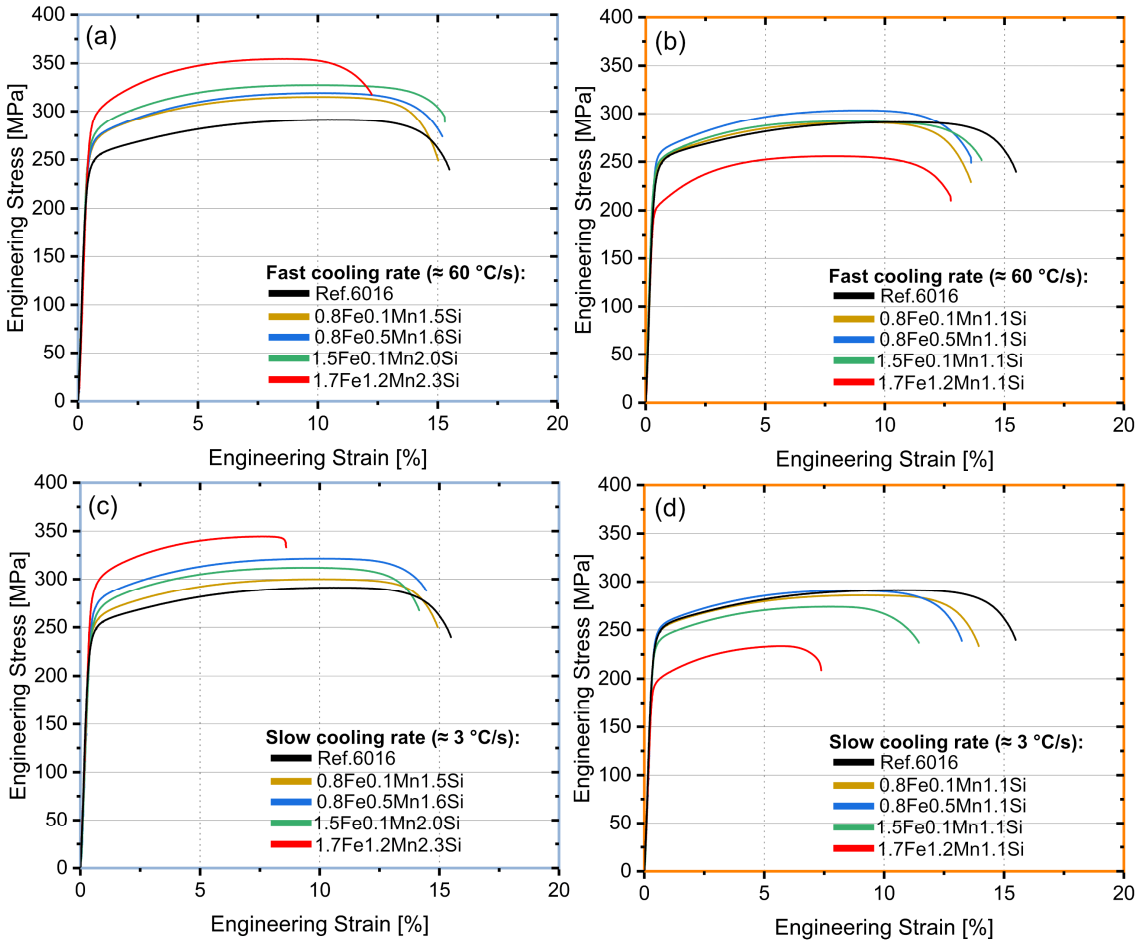

Figure 5-10: Technical stress-strain curves of the test alloys for (a,b) fast and (c,d) slow solidification conditions after artificial aging at 185°C for 5h.

The slowly solidified alloys 0.8Fe0.1Mn1.5Si, 0.8Fe0.5Mn1.6Si and 1.5Fe0.1Mn2.0Si were also subjected to a paint-bake simulation: pre-aging for 5 hours at 100°C → 11 days of natural aging → application 2% of plastic strain → 3 days of natural aging → artificial aging for 20 minutes at 185°C. The results of tensile tests can be seen in Table 5-3. $\Delta R_{p0.2}$ represents the age-hardening response of the paint-bake treatment compared to the condition after 14 days of natural aging (T4). These alloys exhibit a pronounced artificial aging potential and mechanical properties that compare very well with those of the low-Fe reference alloy 6016.

Table 5-3: Results of tensile tests on alloys 0.8Fe0.1Mn1.5Si, 0.8Fe0.5Mn1.6Si and 1.5Fe0.1Mn2.0Si at slow solidification speeds after paint-bake treatment and the corresponding age-hardening response $\Delta R_{p0.2}$

Alloy	Yield strength $R_{p0.2}$ [MPa]	Tensile strength R_m [MPa]	Uniform elongation A_u [%]	Elongation at fracture A_{30} [%]	$\Delta R_{p0.2}$ [MPa]
EN-AW 6016	218±1	276±2	14.6±0.3	19.2±1.2	108
0.8Fe0.1Mn1.5Si	240±1	301±2	14.2±0.2	19.7±2.2	113
0.8Fe0.5Mn1.6Si	254±1	317±1	14.5±0.3	20.0±0.4	106
1.5Fe0.1Mn2.0Si	254±1	313±1	13.3±0.1	18.2±0.1	118

5.4 Discussion

Because Fe is considered to be an impurity element, there are strict Fe limits for Al-alloys [16]. Exceeding these limits is traditionally accompanied by a deterioration in mechanical properties, in particular a reduction in ductility [15]. However, through thermomechanical treatment, Fe-rich primary phases can be modified in size and morphology, contributing to a fine-grained microstructure. In comparison to alloy 6016, the Fe-rich alloys feature improved mechanical properties due to a tuned microstructure. They exhibit higher yield and tensile strength and impressively high elongation values. Simultaneously, strain hardening is more pronounced in alloys featuring high amounts of Fe-rich IMPs, which might indicate good formability in the T4-state. The microstructure evolution and enhanced mechanical properties are discussed in detail below.

5.4.1 Microstructure evolution

In this section the development of the microstructure is discussed with special emphasis on the fragmentation of IMPs during rolling and their grain refining effect.

5.4.1.1 Fragmentation of IMPs via thermomechanical treatment

Modification of the iron-rich IMPs begins during homogenization. At the temperature applied, both platelet and lamellar AlFeSi-phases undergo partitioning into individual particles and show a slight coarsening compared to the as-cast structure. This result agrees well with the literature [8,32,33,50]. However, a decisive modification change must also be attributed to hot forming [51]. Rolling, especially cold rolling in our case (Figure 5-2), causes extensive fragmentation of brittle IMPs into fine particles, which could also be seen in [51,52] for other Al-systems containing Fe-rich intermetallics. According to [53], the morphology of primary phases has a significant effect on mechanical fragmentation. IMPs with high aspect ratios break more easily under deformation stresses than do those with spherical or cubic morphologies [19]. From this perspective, platelet β-AlFeSi can be just as advantageous for the formation of fine particles as branched α-AlFeSi. The comminution of IMPs in the test alloys by thermomechanical treatment is very comparable to what happens to foil materials. Alloys of the 8xxx-series are characterized by high amounts of Fe-rich primary phases, which break up into segments of finely distributed particles, increasing strength properties and creep resistance [9]. Theoretically, microvoids can form during the mechanical comminution of large second-phase particles [19]. Even though such cavities have occasionally been found in slowly solidified alloys 1.7Fe1.2Mn2.3Si and 1.7Fe1.2Mn1.1Si due to the fragmentation of coarse faceted AlFeSi-phases, the crushed particles are able to reconnect well with the matrix during thermomechanical processing. Que [37] and Dinnis [21] found that these primary intermetallic compounds are α-Al(Fe,Mn)Si-phases with a body-centered cubic crystal structure. This evidence is supported by EBSD analysis [38], which revealed a cubic lattice for the giant faceted particles, also known as sludge [54], as seen in Figure 5-1.

Sludge forms when a certain concentration of Fe, Mn, and Cr is exceeded. This can be estimated by the critical segregation factor (SF_{crit} = 3.7 at casting temperature of 760 C) [54,55].

$$SF = 1 \cdot Fe + 2 \cdot Mn + 3 \cdot Cr \ (wt.\%) \quad \text{(Eq. 5-1)}$$

With SF = 4.1, the alloys 1.7Fe1.2Mn2.3Si and 1.7Fe1.2Mn1.1Si exceed SF_{crit}, which leads to the formation of sludge, while the other alloys do not pass the critical value of 3.7. Sedimentation of this coarse phase in alloy 1.7Fe1.2Mn2.3Si at slow solidification is illustrated in Figure 5-14 of the appendix.

5.4.1.2 Grain refinement by IMPs

The grain refinement in alloys featuring high Fe-content can be attributed to an enhanced nucleation rate during recrystallization due to particle stimulated nucleation (PSN) [51,56–58]. Near the interfaces of fragmented iron-rich intermetallic particles, an increased dislocation density forms [59] which acts as a favourable site for recrystallization nuclei [51,56,57]. In parallel, coarsening of the newly formed grains is prevented by the large number of interfaces, which originate from dispersoids and fragmented primary phases [44,52,56,57,60,61]. The chain-like arrangement of the primary phases in the rolling direction generates a grain size distribution with fine grains in high particle density areas and adjacent coarser grains (see Figure 5-7). This was also revealed in other studies on Al-alloys with high Fe-content [52]. A grain size distribution like this can be attributed to the effect of multiscale intermetallic phases, which act as nucleation sites for new grains (fragmented IMPs), but also inhibit grain growth (because of dispersoids) [52,58].

Because fragmentation of brittle iron-rich primary phases by rolling can be very helpful in the effort to achieve small IMP sizes (see Figure 5-3), the occurrence of PSN must be ensured to benefit successfully from the grain refining effect. In considering the net driving force for recrystallization in the presence of multiscale particles, the minimum IMP-size d_{min} to successfully act as a nucleation site for new grains can be approximated by equation [58,62]:

$$d_{min} = \frac{4 \cdot \gamma_{gb}}{P_D - P_Z} = \frac{4 \cdot \gamma_{gb}}{\frac{\rho \cdot G \cdot b^2}{2} - \frac{3 \cdot f_d \cdot \gamma_d}{d_d}} \quad \text{(Eq. 5-2)}$$

with P_D the driving pressure for growth resulting from stored deformation energy, i.e. dislocation density ϱ, G = 25.5 GPa (shear modulus of Al), b = 0.29 nm (Burgers vector of Al) and $\gamma_{gb} \approx$ 324 mJ/m² [63] (high angle grain boundary interfacial energy of Al). The Zener pinning pressure P_Z opposes P_D and consists of γ_d (interfacial energy dispersoid/Al-Matrix), f_d and d_d (volume fraction and diameter of dispersoids). The interfacial energy between the AlFeSi-dispersoids and the Al-Matrix is assumed to be $\gamma_d \approx$ 500 mJ/m² [64]. With an estimated dislocation density of $\varrho \approx 10^{15}$ m^{-2} in the cold rolled state [65], $d_d \approx$ 100 nm and 0.002 < f_d < 0.01 (Table 5-2), a minimum particle size to trigger PSN is calculated to be 1.2 < d_{min} [µm] < 1.4. However, one must consider that $P_D = f(\varrho)$ has a significant impact on d_{min}. Furthermore, because (as described in section 4.5 below) IMPs contribute

significantly to the increase in dislocation density, the estimation according to [65] may be too conservative and a critical particle size of roughly 1 μm may be quite plausible (see Figure 5-5).

As mentioned in section 5.3.1, an increased Cube orientation fraction can be seen in alloy 1.7Fe1.2Mn1.1Si (fast solidification). Inhibition of PSN by a strong Zener drag exerted by a large amount of fine dispersoids (see Table 5-2) [56,62] can be expected. In the more slowly cooled alloys, few nuclei in Cube orientation seem to exist, but they experience low growth restrictions. The P orientation {011}<566>, often interpreted as a typical PSN texture component, is present in all samples with both a very low area fraction and a low number, implying that there is not only growth but also a nucleation constraint.

5.4.2 Mechanical properties

In the following the relationship of yield strength and ductility is analyzed based on the microstructural features formed by the processing of the Al-Mg-Si-Fe crossover alloys. A special focus is the direct effect of IMPs.

5.4.2.1 Effect of microstructure on yield strength

First, the improvement in yield strength in T4 condition is assessed. This improvement is the sum of linked microstructural effects associated with the corresponding strengthening mechanisms in terms of solid solution strengthening, grain refinement, dispersion strengthening, precipitation strengthening and hetero-deformation strengthening induced by the formation of geometrical necessary dislocations (GNDs) caused by fragmented IMPs [66]. The contribution of each strengthening mechanism is discussed, except for that of precipitation hardening, which at balanced Si content can be considered independent of the presence of IMPs.

Grain boundary hardening (GBH) is obvious, as the test alloys feature smaller grain sizes than 6016. The strength increase can be calculated according to Hall-Petch with k_y of 80 MPa$\sqrt{(\mu m)}$ [67]. Depending on the content of Fe-rich IMPs and the solidification conditions, the average grain size of the test alloys ranges between ~5 μm for fast solidified alloy 1.7Fe1.2Mn2.3Si and ~17 μm for slowly solidified alloy 0.8Fe0.1Mn1.1Si ($5 < D\ [\mu m] < 17$). The corresponding strength increase due to grain refinement compared to reference 6016 (ECD ~24 μm) results in $3 < \Delta R_{p0.2}\ [MPa] < 19$.

Dispersion hardening (DH) is linked to the size of intermetallic phases and is only relevant for submicron IMPs precipitated secondarily during homogenization. Fine dispersoids counteract the movement of dislocations and generate an increase in strength, which can be calculated as described in [29,68] in dependence on the size, d_d, and volume fraction, f_d, of dispersoids:

$$\sigma_d = M \frac{2 \cdot G \cdot b}{d_d} \sqrt{\frac{3}{2 \cdot \pi} f_d} \qquad \text{(Eq. 5-3)}$$

with M = 3.1 (Taylor factor). The increase in strength, $\Delta R_{p0.2}$, compared to 6016 using data from Table 5-2 (volume fraction approximated by the average area fraction [69]) is calculated to be between 0 MPa (1.5Fe0.1Mn2.0Si) and 13 MPa (1.7Fe1.2Mn2.3Si).

The strength increase caused by the formation of GNDs (GND hardening, or "GNDH"), hetero-deformation-induced strengthening [66]) around rigid IMPs, is attributed to two key factors: first, the difference in thermal expansion between the Al matrix and the fragmented Fe-rich primary phases; and second, the enhanced deformation of the Al matrix around the non-deformable particles during plastic deformation. In both cases Ashby's concept [70] is used to calculate the number of dislocation loops, *n*, necessary to compensate for the geometric mismatch between the Al matrix and IMPs. As already stated in [7], when quenching from solution heat treatment temperature, the number of additional GNDs originating from the difference in thermal expansion coefficient Δa between the Al matrix and the IMPs can be determined by applying equation (5-4) [67].

$$n = 3 \cdot \Delta\alpha \cdot \Delta T \frac{d}{b} \qquad \text{(Eq. 5-4)}$$

With $\Delta a \approx 14\text{x}10^{-6}$ K^{-1} [71], ΔT=540 K (quenching from 560°C to RT) and an average particle diameter *d* of ≈ 1 μm, approximately 78 dislocations per IMP were obtained. Since we estimate the particle diameter to be 1 μm for all alloys, the dislocation density induced by the difference in the expansion coefficient is simply a function of the volume fraction f_V of IMPs, which was found for the Fe-rich alloys to be $0.02 < f_V < 0.09$ (volume fraction approximated by the average area fraction [69]). Accordingly, this produces a dislocation density ϱ *of* $2.0\text{x}10^{12} < \varrho\ [\text{m}^{-2}] < 8.9\text{x}10^{12}$. With the Taylor equation [72]

$$\sigma_T = M \cdot \alpha \cdot G \cdot b \sqrt{\rho} \qquad \text{(Eq. 5-5)}$$

an increase in yield strength of $11.5 < \Delta R_{p0.2}$ [MPa] < 24.3 is obtained (assuming $M\alpha = 1.1$; since M=3.1 and a≈0.3-0.4 [73]).

Plastic deformation of the Al-matrix by 0.2% up to the yield stress $R_{p0.2}$ requires additional dislocation loops to compensate for the volume difference relative to the undeformed rigid IMPs. According to the Ashby concept [70], the density of GNDs after plastic deformation by ε can be estimated by applying equation 5-6:

$$\rho_{GND} = \frac{\lambda_G}{b} \frac{f_V}{d} \varepsilon \qquad \text{(Eq. 5-6)}$$

where λ_G is a constant that reflects the shape of the IMPs (l_G=8 for cubic particles [70] and estimated to be 6 for spherical particles), *d* their size and f_V their volume fraction. Assuming an average particle size of 1 μm, a volume fraction ranging between $0.02 < f_V < 0.09$ and a plastic deformation of $\varepsilon = 0.2\%$, with $\lambda_G = 6$ an additional GND density of $0.83\text{x}10^{12} < \varrho\ [\text{m}^{-2}] < 3.7\text{x}10^{12}$ is calculated. By applying the Taylor equation (5), one calculates a yield strength increase by $7.4 < \Delta R_{p0,2}$ [MPa] < 16.

Summing up the contributions to the increase in yield strength caused by the Fe-IMPs compared to the reference alloy gives a value of 48 MPa; this is seen for example in the slowly solidified alloy 0.8Fe0.5Mn1.6Si. (GBH: 13 MPa, DH: 10 MPa, GNDH: 15.2+9.8 MPa), which agrees with the experimentally determined yield stress increase of $DR_{p0.2}$(tensile test) = 38 MPa.

Thus, in agreement with the literature [66,74], we can confirm that the heterogeneous microstructure (Al matrix / Fe-rich IMPs) of the test alloys featuring high Fe content positively affects strength properties, at least when the Si content is well balanced to account for its incorporation into Fe-rich IMPs.

In cases where the Si content is not well balanced, the picture is different (see Figure 5-9, right-hand sub-pictures). Here the contribution of Si to solid solution hardening must be taken into account. In alloys with additional Si no effect of IMPs on solid solution hardening can be assumed, because the increased Si-content was incorporated into the primary phases. On the other hand, in alloys with no additional Si we must accept a loss of strength due to reduced solid solution hardening. Because the amount of Mg in solid solution can be assumed to be equal for all alloy systems looked at in this paper, we only need to consider the effect of a lower Si-content compared to 6016. Using FactSage 8.0 database FTlite, we determined the amount of Si in solid solution at solution annealing temperature (560°C) (see Table 5-4) and calculated the corresponding strength loss using equation (7) [75], where c_{Si} is the concentration of Si in solid solution and k_{Si} is the Si scaling factor (k_{Si} = 66.3 MPa (wt.%)$^{-2/3}$) [76].

$$\sigma_{ss} = k_{Si} \cdot c_{Si}^{2/3} \qquad \text{(Eq. 5-7)}$$

Table 5-4: Amount of Si in solid solution at solution annealing temperature and corresponding strength loss due to reduced solid solution strengthening compared to 6016 as a reference.

Alloy	**C_{Si} [wt.%]**	**Strength loss compared to 6016 [MPa]**
EN-AW 6016	1.0	-
0.8Fe0.1Mn1.1Si	0.7	14
0.8Fe0.5Mn1.1Si	0.6	19
1.5Fe0.1Mn1.1Si	0.4	30
1.7Fe1.2Mn1.1Si	0.3	37

At this point it should be noted that the lower Si content in solid solution not only causes less solid solution hardening (not desirable), but also results in less pronounced natural aging (condition T4, desirable). Furthermore, the very low Si-content in solid solution (~0.3 wt.%) of alloy 1.7Fe1.2Mn1.1Si manifests itself in a significant weakening of the precipitation hardening response during artificial aging (not desirable), which can be clearly seen in Figure 5-10.

5.4.2.2 Effect of microstructure on the ductility

In addition to the hardening effect, three features are particularly striking in the stress-strain curves in Figure 5-9. (i) With the exception of the slowly solidified alloy 1.7Fe1.2Mn2.3Si, which contains the coarse sludge phase, no alloy exhibits premature failure, i.e. failure occurs only in the necking region of the samples despite high Fe-IMP content. (ii) Strain hardening is more pronounced in the Fe-rich alloys and increases significantly with increasing IMP volume content. (iii) High elongation values comparable to those of the low-Fe reference alloy were achieved.

The fact that no premature failure occurs was already addressed in our previous work [7]. Kernel average misorientation (KAM) studies have shown that no zones of local deformation in the form of narrow macro-shear bands develop. Non-uniform deformation within such zones would lead to premature fracture due to the growth and coalescence of voids [77]. Such voids are generally caused by the cracking of coarse second-phase particles, especially Fe-rich IMPs with high aspect ratios [19], or by the decohesion between the matrix and the second-phase particles due to dislocation accumulation stresses at the particle–matrix interface [20]. The advantageous spherical morphology and the small size of the IMPs contribute decisively to their avoidance in each of the possible failure initiations. However, we also consider the small grains and the GND forest surrounding the particles responsible for preventing early crack formation.

The formation of coarse IMPs (sludge) observed at high Fe and simultaneously high Mn content, which cannot be fragmented by thermomechanical treatment, obviously leads to premature cracking and can thus be seen as a limitation in alloy design. However, it should be noted that the critical segregation factor depends on the melt temperature [54] and thus its increase can be capable of remedy for alloys with very high Fe and Mn content.

The formation of GNDs around rigid IMPs and the resulting hardening effect discussed above are equivalent to increased strain hardening (hetero-deformation-induced strain hardening [66]) in the regime of plastic deformation. Since the plastic strain hardening of a material is related to statistically stored dislocations (SSD) and geometrically necessary dislocations, the associated yield stress can be calculated as:

$$\sigma = M \cdot \alpha \cdot G \cdot b \sqrt{\rho_{SSD} + \rho_{GND}} \qquad \text{(Eq. 5-8)}$$

The applicability of this analytical relationship is now verified using the technologically interesting example of the slowly solidified alloy 0.8Fe0.5Mn1.6Si. For this purpose, we consider Figure 5-11, which shows the strain hardening compared to the reference in T4-condition.

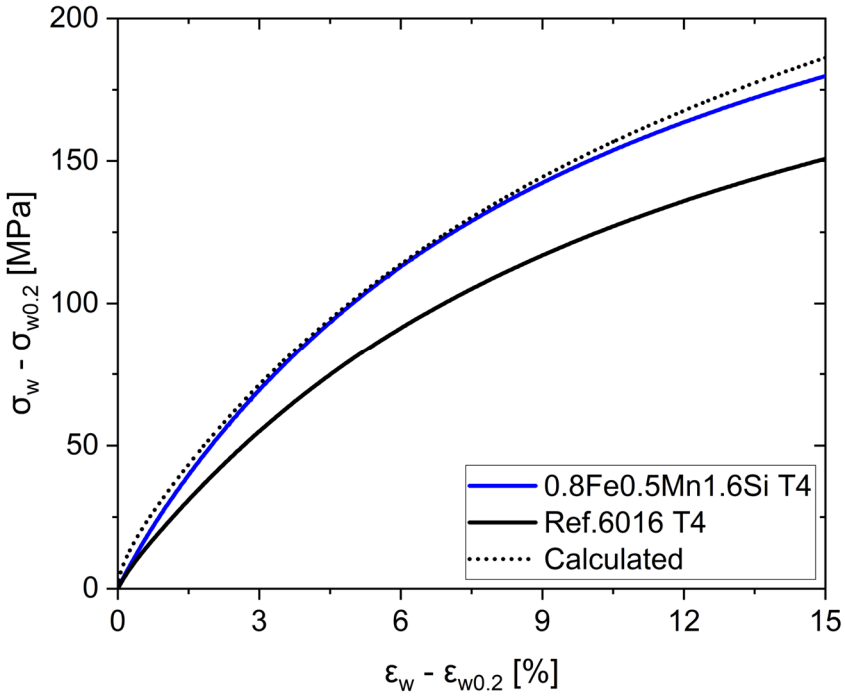

Figure 5-11: True stress plotted against true strain starting at the yield point for alloy 0.8Fe0.5Mn1.6Si and Ref.6016 in T4 condition. The dashed line represents work hardening caused by SSDs, as in alloy 6016, but enhanced by GNDs induced by IMPs present in 0.8Fe0.5Mn1.6Si.

Assuming that only SSDs and no GNDs are produced in reference alloy 6016, the corresponding dislocation density can be calculated using the Taylor equation (5-5). By applying equation (5-6), we estimate the GND dislocation density induced by the IMPs in alloy 0.8Fe0.5Mn1.6Si (note: d= 1µm, $f_V \approx 3.5\%$). Assuming that ρ_{SSD} does not change significantly due to the presence of IMPs, a total dislocation density ($\rho_{SSD} + \rho_{GND}$) can be calculated. By using equation (8) the increase in strength during plastic deformation can be drawn (dotted line in Figure 5-11). The curve calculated on the basis of these considerations clearly matches that of alloy 0.8Fe0.5Mn1.6Si over a wide strain range and confirms the applicability of the Ashby approach.

Considering the contributions of SSD and GND to the total dislocation density, it can be deduced from this analysis that the contribution of IMP-induced GNDs to strength predominates over SSDs in the early stages of strain hardening, when plastic strain is small, but that SSDs predominate in the later stages. This is a finding that was already reported in [78,79].

In the following, to obtain a better picture of the strain-hardening events and the high strain values also achieved in Fe-rich alloys, we consider the Kocks-Mecking (KM) approach for describing the dislocation storage induced by plastic strain [80]. For the low IMP alloy the evolution of the average dislocation density may be expressed as the competition between a storage term and an annihilation term:

$$\frac{d\rho}{d\varepsilon} = \frac{\lambda_S}{b}\sqrt{\rho} - \lambda_A \rho \qquad \text{(Eq. 5-9)}$$

λ_S is a constant which describes the dislocation storage due to the interaction with forest dislocations, and λ_A is a parameter that specifies the dislocation annihilation due to dynamic recovery. As discussed above, in our specific case involving IMP-rich alloys the formation of GNDs around rigid IMPs must be accounted for by an additional term for dislocation accumulation:

$$\frac{d\rho_{GND}}{d\varepsilon} = \frac{\lambda_G}{b}\frac{f_V}{d} \qquad \text{(Eq. 5-10)}$$

Thus the overall balance for dislocation storage and annihilation results in the equation:

$$\frac{d\rho}{d\varepsilon} = \frac{1}{b}\left(\lambda_S\sqrt{\rho} + \lambda_G\frac{f_V}{d}\right) - \lambda_A\rho \qquad \text{(Eq. 5-11)}$$

Linking the dislocation density with the flow stress according to the Taylor equation provides the expression for the strain hardening:

$$\frac{d\sigma}{d\varepsilon} = \frac{\alpha \cdot G \cdot b}{2\sqrt{\rho}}\frac{d\rho}{d\epsilon} \qquad \text{(Eq. 5-12)}$$

A comparison of strain hardening dσ/dε of the IMP-poor reference alloy with IMP-rich alloys can now be made using a KM-plot [81]. The insert to Figure 5-12 shows the comparison of reference alloy 6016 with the above-mentioned alloy 0.8Fe0.5Mn1.6Si in the slowly solidified state. The difference in strain-hardening behavior is clearly visible under both T4 and T6 conditions. The level of stain hardening rate is higher for the Fe-rich variant and is shifted to higher stress levels, as predicted by the considerations above. However, it is important to note that the stress normalized strain hardening rate $\frac{1}{\sigma}\frac{d\sigma}{d\varepsilon}$ shown in Figure 5-12 follows a comparable trend for both alloys and conditions. Consequently, in the tensile test the instability for which the Considère criterion applies, i.e. $\frac{1}{\sigma}\frac{d\sigma}{d\varepsilon} = 1$, is achieved at approximately the same strain value, reflecting roughly the same uniform elongation (see Figures 5-9 and 5-10).

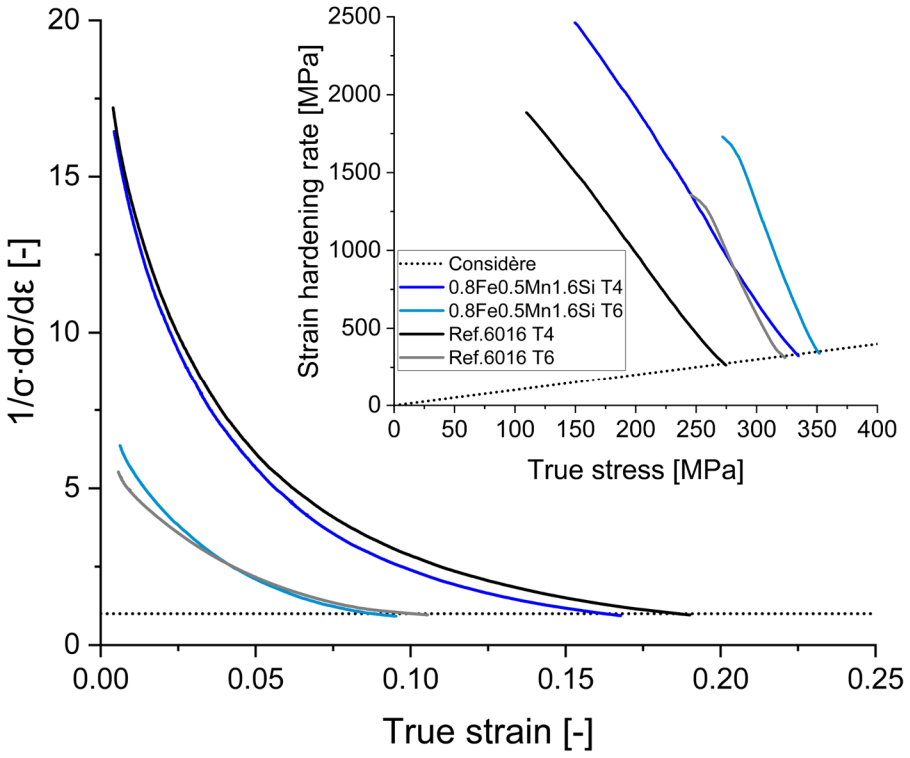

Figure 5-12: Strain hardening rate normalized to the true stress plotted against true strain for alloys 0.8Fe0.5Mn1.6Si (slow solidification rate) and 6016 in T4 and T6 conditions. The insert shows strain hardening rate vs. the true stress (Kocks-Mecking-plot) [81].

Thus it can be stated that Fe-rich IMPs, which have traditionally been thought to have a negative effect on ductility and formability [15], do not necessarily impair the properties of the material. With optimized size and morphology, very attractive levels of strength and ductility can be achieved, even with high IMP volume fractions.

5.5 Conclusions

Two different alloys, EN AW-5182 and EN AW-6082, have been produced via three different ways at different scales, speaking of batch sizes and cooling conditions. Whereas, industrial material is only compared in terms of mechanical parameters, the evaluation of the microstructure shows the following characteristics:

Fe-rich primary intermetallic phases can be controlled effectively in their size and morphology via casting conditions, and – more importantly – by thermomechanical treatments, which further control the microstructure evolution in Al-Mg-Si-Fe crossover alloys. The emerging microstructure, resulting from the large number of primary phases, is reflected in an improvement of material properties.

Several conclusions can be drawn from this study:

(1) Finely branched primary phases (formed by fast solidification rates) and substantially coarser intermetallic AlFeSi-phases (formed by slow solidification rates, comparable to those of an industrial continuous casting process) can both be fragmented into fine particles by thermomechanical

treatment. Cold rolling was found to be the most effective way to form a dense distribution of fine IMPs.

(2) Modification of primary phases generates several positive effects compared to the reference alloy 6016. The test alloys benefit from significantly finer grains, due to the increased nucleation rate of new grains during recrystallization caused by IMPs-induced particle stimulated nucleation. PSN also induces more random grain orientations, generating a rather weak texture, which is desirable [56]. The novel alloys feature higher strain hardening due to the formation of GNDs around the morphologically transformed Fe-rich primary phases. The surprisingly high total elongation can be attributed to the combined effects of IMP refinement and their roundish morphology; refinement of grain sizes; and more uniform deformation [7]. In alloys whose Si-content was adapted to match reference alloy 6016's Si-concentration in solid solution (the formation of AlFeSi-phases consumes Si) and similar Mg content, higher yield and tensile strengths were achieved.

(3) It was found that the artificial age-hardening response of the test alloys featuring increased Si-content is similar to that of reference 6016. Even after paint bake treatment the alloys 0.8Fe0.1Mn1.5Si, 0.8Fe0.5Mn1.6Si and 1.5Fe0.1Mn2.0Si show high precipitation hardening potential. Adjusting Si to account for its incorporation into the Fe-rich primary phases formed, plus correct thermomechanical processing, seem to be key factors in the development of highly Fe-tolerant Al-Mg-Si wrought alloys.

In this study the age-hardening capability of Al-Mg-Si alloys and the microstructure-controlling effect of primary intermetallic phases on processing deployed in the context of foil stock were successfully combined using a crossover approach. This offers significant potential for enlarging the property profile of Al-Mg-Si alloys to include greater strain hardening capability and prospects for recycling.

5.6 Appendix V

Table 5-5: Mechanical properties of the test alloys in T4 and T6 condition (± refers to the standard deviation).

Alloy in T4 (fast solidification)	**$R_{p0.2}$ [Mpa]**	**R_m [Mpa]**	**A_u [%]**	**A_{30} [%]**
0.8Fe0.1Mn1.5Si	118±1	248±0.7	23.5±0.3	28.3±1.9
0.8Fe0.5Mn1.6Si	134±1	269±1.5	21.9±0.2	27.6±0.1
1.5Fe0.1Mn2.0Si	125±1	261±1	21.6±0.3	27.3±1.3
1.7Fe1.2Mn2.3Si	161±1	311±1	19.6±0.2	26.5±1.0
0.8Fe0.1Mn1.1Si	106±1	226±2	21.4±1.0	25.9±1.6
0.8Fe0.5Mn1.1Si	108±1	232±1	21.0±0.8	25.3±1.2
1.5Fe0.1Mn1.1Si	102±1	224±1	20.2±0.4	23.8±0.9
1.7Fe1.2Mn1.1Si	88±1	204±2	17.4±1.1	21.0±1.3
Ref.6016	110±1	229±1	25.1±0.1	30.5±0.4

Alloy in T4 (slow solidification)	**$R_{p0.2}$ [Mpa]**	**R_m [Mpa]**	**A_u [%]**	**A_{30} [%]**
0.8Fe0.1Mn1.5Si	127±2	260±2	23.0±0.3	28.4±1.6
0.8Fe0.5Mn1.6Si	148±1	285±1	21.6±0.6	27.8±1.5
1.5Fe0.1Mn2.0Si	136±1	273±2	20.5±0.4	24.4±1.0
1.7Fe1.2Mn2.3Si	153±5	296±10	14.8±1.6	15.4±1.9
0.8Fe0.1Mn1.1Si	111±2	235±3	23.0±0.5	28.0±0.5
0.8Fe0.5Mn1.1Si	115±3	241±4	20.9±0.3	25.5±0.9
1.5Fe0.1Mn1.1Si	100±3	221±4	21.4±0.5	26.8±1.0
1.7Fe1.2Mn1.1Si	84±3	185±5	14.8±0.6	17.2±0.2

Alloy in T6 (fast solidification)	**$R_{p0.2}$ [Mpa]**	**R_m [Mpa]**	**A_u [%]**	**A_{30} [%]**
0.8Fe0.1Mn1.5Si	263±1	316±1	9.2±0.5	14.2±1.2
0.8Fe0.5Mn1.6Si	268±3	321±2	9.4±0.1	14.0±0.5
1.5Fe0.1Mn2.0Si	268±2	326±2	9.1±0.1	14.0±0.9
1.7Fe1.2Mn2.3Si	292±1	353±1	7.8±0.6	11.0±0.8
0.8Fe0.1Mn1.1Si	247±1	291±1	8.3±0.1	13.5±0.3
0.8Fe0.5Mn1.1Si	257±1	302±1	8.5±0.1	13.8±0.6
1.5Fe0.1Mn1.1Si	250±1	292±1	8.1±0.2	12.8±1.1
1.7Fe1.2Mn1.1Si	203±1	252±3	6.5±0.9	10.2±1.8
Ref.6016	243±1	288±3	9.6±0.4	15.1±1.3

Alloy in T6 (slow solidification)	**$R_{p0.2}$ [Mpa]**	**R_m [Mpa]**	**A_u [%]**	**A_{30} [%]**
0.8Fe0.1Mn1.5Si	253±2	302±2	9.5±0.2	14.3±0.3
0.8Fe0.5Mn1.6Si	272±1	323±1	9.3±0.2	13.9±0.3
1.5Fe0.1Mn2.0Si	263±4	315±2	8.7±0.2	12.7±0.8
1.7Fe1.2Mn2.3Si	288±4	338±6	6.8±0.6	8.2±0.9
0.8Fe0.1Mn1.1Si	244±2	284±4	8.1±0.9	12.8±0.8
0.8Fe0.5Mn1.1Si	243±5	284±6	8.2±0.1	12.9±1.8
1.5Fe0.1Mn1.1Si	242±5	280±5	7.2±0.2	11.1±1.3
1.7Fe1.2Mn1.1Si	187±8	225±7	4.9±0.4	6.8±1.1

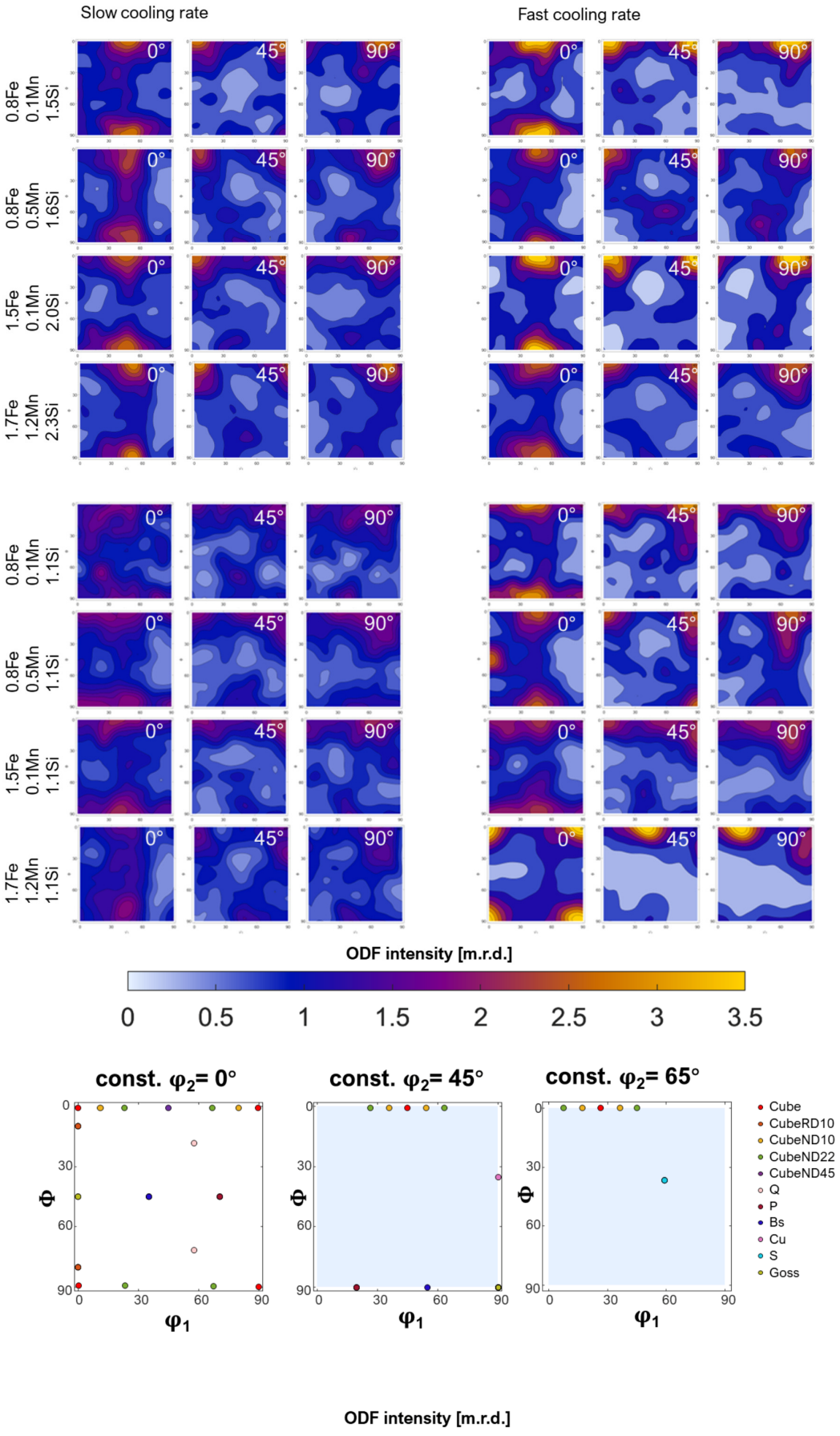

Figure 5-13: ODF maps of the test alloys after slow and fast solidification in T4 condition.

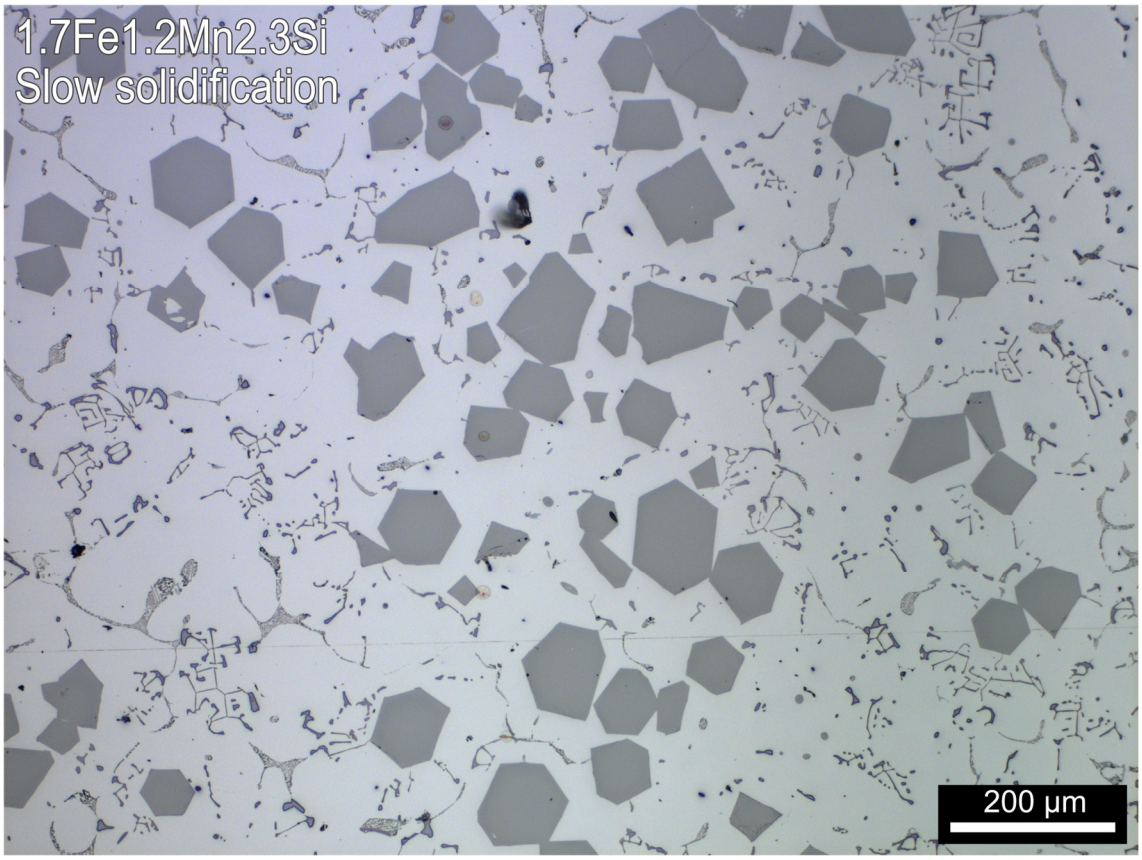

Figure 5-14: Sedimentation of sludge phases for alloy 1.7Fe1.2Mn2.3Si after slow solidification.

5.7 References

[1] F. Ostermann, Anwendungstechnologie Aluminium, 3rd ed., Springer Vieweg, Berlin, 2014.

[2] R. Prillhofer, G. Rank, J. Berneder, H. Antrekowitsch, P.J. Uggowitzer, S. Pogatscher, Materials (Basel, Switzerland) 7 (2014) 5047–5068.

[3] R. Prillhofer, J. Berneder, G. Rank, H. Antrekowitsch, S. Pogatscher, P.J. Uggowitzer, in: J. Grandfield (Ed.), Light Metals 2014, Springer International Publishing; Imprint; Springer, Cham, 2016, pp. 227–232.

[4] R.A. Antunes, M.C.L. de Oliveira, Materials & Design 63 (2014) 247–256.

[5] F. Grabner, B. Gruber, C. Schlögl, C. Chimani, Aluminium Alloys - Their Physical and Mechanical Properties 941 (2018) 1397–1403.

[6] L. Stemper, M.A. Tunes, R. Tosone, P.J. Uggowitzer, S. Pogatscher, Progress in Materials Science (2021) 100873.

[7] B. Trink, I. Weißensteiner, P.J. Uggowitzer, K. Strobel, S. Pogatscher, Scripta Materialia 215 (2022) 114701.

[8] M. Lentz, G. Laptyeva, O. Engler, Journal of Alloys and Compounds 660 (2016) 276–288.

[9] L. Pan, K. Liu, F. Breton, X. -Grant Chen, J. of Materi Eng and Perform 25 (2016) 5201–5208.

[10] O. Engler, J. Aegerter, D. Calmer, Materials Science and Engineering: A 775 (2020) 138965.

[11] J. Sarkar, T. Kutty, D. Wilkinson, J. Embury, D. Lloyd, Materials Science and Engineering: A 369 (2004) 258–266.

[12] W.B. Lievers, A.K. Pilkey, D.J. Lloyd, Materials Science and Engineering: A 361 (2003) 312–320.

[13] K. Suzuki, S. Kumai, Y. Saito, T. Haga, Mater. Trans. 46 (2005) 2602–2608.

[14] F. Andreatta, A. Lanzutti, L. Fedrizzi, Surf. Interface Anal. 48 (2016) 789–797.

[15] L.F. Mondolfo, Aluminium alloys: Structure and properties, Butterworth, London, Boston, 1979.

[16] L. Zhang, J. Gao, L.N.W. Damoah, D.G. Robertson, Mineral Processing and Extractive Metallurgy Review 33 (2012) 99–157.

[17] D. Raabe, D. Ponge, P.J. Uggowitzer, M. Roscher, M. Paolantonio, C. Liu, H. Antrekowitsch, E. Kozeschnik, D. Seidmann, B. Gault, F. de Geuser, A. Deschamps, C. Hutchinson, C. Liu, Z. Li, P. Prangnell, J. Robson, P. Shanthraj, S. Vakili, C. Sinclair, L. Bourgeois, S. Pogatscher, Progress in Materials Science 128 (2022) 100947.

[18] J.A.S. Green, Aluminum Recycling and Processing for Engergy Conservation and Sustainability, A S M International, Materials Park, 2007.

[19] A. Bjurenstedt, E. Ghassemali, S. Seifeddine, A.K. Dahle, Materials Science and Engineering: A 756 (2019) 502–507.

[20] D. Broek, Engineering Fracture Mechanics 5 (1973) 55–66.

[21] C.M. Dinnis, J.A. Taylor, A.K. Dahle, Scripta Materialia 53 (2005) 955–958.

[22] L. Lu, A.K. Dahle, Metall Mater Trans A 36 (2005) 819–835.

[23] M. Cooper, Acta Cryst 23 (1967) 1106–1107.

[24] P. Skjerpe, MTA 18 (1987) 189–200.

[25] S. Ji, W. Yang, F. Gao, D. Watson, Z. Fan, Materials Science and Engineering: A 564 (2013) 130–139.

[26] N. Kuijpers, F.J. Vermolen, C. Vuik, P. Koenis, K.E. Nilsen, S. van der Zwaag, Materials Science and Engineering: A 394 (2005) 9–19.

[27] M.S. Remøe, K. Marthinsen, I. Westermann, K. Pedersen, J. Røyset, C. Marioara, Materials Science and Engineering: A 693 (2017) 60–72.

[28] S. Zajac, B. Hutchinson, A. Johansson, L.-O. Gullman, Materials Science and Technology 10 (1994) 323–333.

[29] Y. Wang, Y. Deng, Q. Dai, K. Jiang, J. Chen, X. Guo, Materials Science and Engineering: A 803 (2021) 140477.

[30] S. Belmares-Perales, Met. Mater. Int. 14 (2008) 307–314.

[31] S.G. Shabestari, M. Ghanbari, Journal of Alloys and Compounds 508 (2010) 315–319.

[32] F. Alvarez-Antolin, J. Asensio-Lozano, A. Cofiño-Villar, A. Gonzalez-Pociño, Metals 10 (2020) 620.

[33] N. Kuijpers, C. , W, F. Vermolen, J, K. Vuik, S. Zwaag, van , der, Mater. Trans. 44 (2003) 1448–1456.

[34] G.N. Haidemenopoulos, H. Kamoutsi, A.D. Zervaki, Journal of Materials Processing Technology 212 (2012) 2255–2260.

[35] F.Schmid, L. Stemper, T. Ebner, Walter Leitner, S. Pogatscher, in: Proceedings of the EMC (2019) 639-652.

[36] R. Hielscher, H. Schaeben, J Appl Crystallogr 41 (2008) 1024–1037.

[37] Z. Que, Y. Wang, Z. Fan, Metall Mater Trans A 49 (2018) 2173–2181.

[38] M. KRAL, Scripta Materialia 51 (2004) 215–219.

[39] N. Kuijpers, W.H. Kool, P. Koenis, K.E. Nilsen, I. Todd, S. van der Zwaag, Materials Characterization 49 (2002) 409–420.

[40] O. Engler, G. Laptyeva, N. Wang, Materials Characterization 79 (2013) 60–75.

[41] A. Arnoldt, L. Semmelrock, D. Soukup, J.A. Österreicher, Materials Characterization 191 (2022) 112138.

[42] N. Bayat, T. Carlberg, M. Cieslar, Journal of Alloys and Compounds 725 (2017) 504–509.

[43] H. Tanihata, T. Sugawara, K. Matsuda, S. Ikeno, Journal of Materials Science 34 (1999) 1205–1210.

[44] J. Grasserbauer, I. Weißensteiner, G. Falkinger, T.M. Kremmer, P.J. Uggowitzer, S. Pogatscher, Materials (Basel, Switzerland) 14 (2021) 3204.

[45] D. Wang, H. Zhang, H. Nagaumi, X. Li, J. Cui, Adv. Eng. Mater. 22 (2020) 2000517.

[46] Y.J. Li, A. Muggerud, A. Olsen, T. Furu, Acta Materialia 60 (2012) 1004–1014.

[47] F.J. Humphreys, Journal of Materials Science 36 (2001) 3833–3854.

[48] J. Grasserbauer, I. Weißensteiner, G. Falkinger, S. Mitsche, P.J. Uggowitzer, S. Pogatscher, Materials (Basel, Switzerland) 13 (2020).

[49] O. Engler, C.D. Marioara, Y. Aruga, M. Kozuka, O.R. Myhr, Materials Science and Engineering: A 759 (2019) 520–529.

[50] H. Merchant, J. Morris, D. Hodgson, Materials Characterization 25 (1990) 339–373.

[51] E. Aryshenskii, J. Hirsch, S. Konovalov, Metals 11 (2021) 507.

[52] M.X. Guo, J. Zhu, Y. Zhang, G.J. Li, T. Lin, J.S. Zhang, L.Z. Zhuang, Materials Characterization 132 (2017) 248–259.

[53] R. Hamerton, H. Cama, M.W. Meredith, Aluminium Alloys - Their Physical and Mechanical Properties 331-337 (2000) 143–154.

[54] E. Taghaddos, M.M. Hejazi, R. Taghiabadi, S.G. Shabestari, Journal of Alloys and Compounds 468 (2009) 539–545.

[55] D. Bösch, S. Pogatscher, M. Hummel, W. Fragner, P.J. Uggowitzer, M. Göken, H.W. Höppel, Metall Mater Trans A 46 (2015) 1035–1045.

[56] F.J. Humphreys, Acta Metallurgica 25 (1977) 1323–1344.

[57] O. Engler, J. Hirsch, Materials Science and Engineering: A 336 (2002) 249–262.

[58] F.J. Humphreys, M. Hatherly, Recrystallization and related annealing phenomena, 2nd ed., Elsevier, Amsterdam, 2004.

[59] D. Kim, J. Kim, J.-Y. Jeon, Y.-W. Kim, E. Kobayashi, Materials Letters 309 (2022) 131337.

[60] L. Yu, L. Chen, H. Wang, X. Wang, W. Peng, Y. Wang, L. Zhuang, Metall. Res. Technol. 117 (2020) 508.

[61] L. Yuan, M. Guo, K. Yu, J. Zhang, L. Zhuang, Philosophical Magazine 101 (2021) 1417–1442.

[62] T.A. Bennett, R.H. Petrov, L. Kestens, Scripta Materialia 62 (2010) 78–81.

[63] J.M. Howe, Interfaces in materials: Atomic structure, thermodynamics and kinetics of solid-vapor, solid-liquid and solid-solid interfaces, Wiley, New York, 1997.

[64] Lijun Zhang, Mingjun Yang, Kai Li, Shuhong Liu, Pizhi Zhao, Yong Du, International Journal of Materials Research (1584) 91–98.

[65] S.C. Wang, Z. Zhu, M.J. Starink, Journal of Microscopy 217 (2005) 174–178.

[66] Y. Zhu, Metall Mater Trans A 52 (2021) 4715–4726.

[67] P. Ebenberger, P.J. Uggowitzer, S. Kirnstötter, B. Gerold, S. Zaefferer, S. Pogatscher, Scripta Materialia 166 (2019) 64–67.

[68] W.J. Poole, X. Wang, J.D. Embury, D.J. Lloyd, Materials Science and Engineering: A 755 (2019) 307–317.

[69] C.W. Corti, P. Cotterill, G.A. Fitzpatrick, International Metallurgical Reviews 19 (1974) 77–88.

[70] M.F. Ashby, The Philosophical Magazine: A Journal of Theoretical Experimental and Applied Physics 21 (1970) 399–424.

[71] D. Ma, Journal of Applied Physics 124 (2018) 85109.

[72] G. Taylor, Proc. R. Soc. Lond. A 145 (1934) 362–387.

[73] H. Mughrabi, Current Opinion in Solid State and Materials Science 20 (2016) 411–420.

[74] L. Lu, X. Wu, I.J. Beyerlein, Scripta Materialia 187 (2020) 307–308.

[75] O. Myhr, Acta Materialia 49 (2001) 65–75.

[76] S. Jiang, R. Wang, Journal of Materials Science & Technology 35 (2019) 1354–1363.

[77] H. Yamamoto, Conditions for shear localization in the ductile fracture of void-containing materials, Office of Scientific and Technical Information (OSTI), 1977.

[78] N. Wang, Y. Chen, G. Wu, Q. Zhao, Z. Zhang, L. Zhu, J. Luo, Materials Science and Engineering: A 836 (2022) 142728.

[79] H. Zhi, C. Zhang, S. Antonov, H. Yu, T. Guo, Y. Su, Acta Materialia 195 (2020) 371–382.

[80] A.S. Krausz, K. Krausz, Unified Constitutive Laws of Plastic Deformation, Elsevier, Burlington, 1996.

[81] U.F. Kocks, H. Mecking, Progress in Materials Science 48 (2003) 171–273.

6 AL-MG-SI-FE CROSSOVER ALLOYS FOR SHEET FORMING

The basis for the chosen crossover approach is the composition of alloy 6016, which is the preferred Al material for body panels in the European automotive industry because it allows flat hems even on parts with local pre-deformation. As the alloy design presented here is also intended for use in this sector, the bendability of these new alloys needs to be evaluated. Based on the preliminary investigations, a systematic study was conducted to evaluate the bendability and hemming properties after different processing routes. Emphasis was placed on microstructural and damage analysis. The most promising results have been submitted to "Acta Materialia" and are presented in the following section.

Further assessment of formability, i.e. evaluation of plastic anisotropy and stretch formability, of Al-Mg-Si-Fe crossover alloys processed at laboratory scale was not feasible as it requires larger sample sizes. For this reason, testing of the industrial implementation began during this stage.

Mechanisms determining bendability in Al-Mg-Si-Fe crossover alloys [6]

Authors contributions

Bernhard Trink:	Conceptualization, Methodology, Investigation, Visualization, Writing – Original Draft.
Irmgard Weißensteiner:	Investigation, Visualization, Writing – Review & Editing.
Sebastian Samberger:	Investigation, Writing – Review & Editing.
Diego S.R. Coradini:	Investigation, Writing – Review & Editing.
Katharina Strobel:	Writing – Review & Editing.
Georg Falkinger:	Writing – Review & Editing.
Peter J. Uggowitzer:	Conceptualization, Writing – Review & Editing.
Stefan Pogatscher:	Project Administration, Conceptualization, Supervision, Writing – Review & Editing.

Acknowledgements

The authors wish to express their sincere thanks to AMAG Rolling GmbH for providing the material and for the valuable discussions. This work was funded by the Christian Doppler Research Association within the framework of the Christian Doppler Laboratory for Advanced Aluminum Alloys. Financial support from the Austrian Federal Ministry for Digital and Economic Affairs, the National Foundation for Research, Technology and Development and the Christian Doppler Research Association is gratefully acknowledged.

Abstract

Al-Mg-Si-Fe crossover alloys combine the microstructure-controlling effect of iron-rich intermetallic primary phases with the age-hardening properties of Al-Mg-Si alloys. This study investigates the mechanisms which determine bendability in these alloys. The commercial alloy 6016 was heavily doped with Fe and Si to conceptionally mimic some of the effects of increased end-of-life scrap input. The Si content was adjusted to compensate for the Si trapped in iron-rich phases. Various processing routes, from casting to cold-rolled sheet metal, were also considered. The study concluded that the bendability of Al-Mg-Si-Fe crossover alloys does not correlate strictly with the addition of Fe, but is effected mainly by the composition of the aluminum matrix and the processing conditions. The investigation provides detailed insights into the effects of the type and density of intermetallic particles, the overall strength of the alloy, its strain hardening and the development of porosity due

[6] B. Trink, I. Weißensteiner, P.J. Uggowitzer, K. Strobel, S. Samberger, D. Coradini, G. Falkinger, S. Pogatscher, Acta Materialia (submitted and under review)

to particle cracking and the dissolution of phases leading to Kirkendall pores. It shows that bending is limited by damage and further void formation near the surface. It links the fracture of iron-rich primary phases which degrade bending performance itself to aluminum matrix strength and strain hardening. It also reveals that Kirkendall pores have a strong negative effect on bending because (similarly to fractured primary phase particles) these pores promote the formation of narrow shear bands which cause early bending failure. Finally, the study demonstrates that pore formation itself is triggered by slow cooling steps during manufacturing, but that the pores can be healed by adjusting the solution treatment time as the Ostwald ripening of the pores can restore bending capacity in all the alloys and conditions investigated.

6.1 Introduction

Wrought Al-Mg-Si (i.e. 6xxx) alloys have attracted considerable attention in recent years due to their exceptional combination of mechanical properties and corrosion resistance, making them indispensable in a wide range of industrial applications. [1,2]. These alloys are extensively utilized in the aerospace, automotive, and structural engineering sectors owing to their lightweight nature and high strength upon artificial aging [2,3]. Al-Mg-Si alloys used in automotive applications are typically supplied in the T4 condition, which involves solution annealing and natural aging. Subsequent to sheet forming, precipitation hardening is accomplished during the paint bake cycle to enhance the final strength [4]. Nevertheless challenges persist, particularly concerning the alloys' strain hardening capabilities and stretch formability, which impact their manufacturability and performance [5,6].

Iron (Fe) is one of the most common tramp elements in secondary Al alloys. It accumulates through the recycling of aluminum and is challenging to remove by metallurgical means [7]. Owing to the low equilibrium solid solubility of Fe in Al (<0.05 wt.%) it tends to form primary intermetallic phases (hereinafter "IMPs") during the casting process [2]. Traditionally, brittle Fe-rich IMPs have been reported to reduce ductility and to negatively affect formability in wrought alloys, and therefore strict Fe limits are common [7,8]. However, a high Fe content is characteristic of 8xxx foil stock alloys, which consist of mainly pure Al alongside large amounts of Fe (0.7-1.3 wt.% Fe for alloy AA 8079) [9]. The function of Fe in 8xxx alloys is to ensure the grain refinement required to maintain formability at low foil thickness [10,11].

Al-Mg-Si-Fe crossover alloys combine the grain refining effect found in 8xxx foil materials with the inherent age-hardening potential of Al-Mg-Si alloys. When Fe is alloyed into the Al-Mg-Si automotive alloy 6016, a network of Fe-rich primary phases is formed during casting which undergoes extensive fragmentation during thermomechanical processing. This results in fine particles that are capable of significant grain refinement due to particle-stimulated nucleation upon recrystallisation [12]. During plastic deformation, this fine-grained microstructure, with its high volume fractions of well-dispersed Al-Fe-Si particles, promotes the formation of additional geometrically necessary dislocations around

the rigid particles [13]. Adding Fe to a 6xxx series alloy in this way significantly improves strain hardening, bringing it up to the level of the 5xxx series, while maintaining the age hardening potential.

Bending is a common strain path frequently witnessed in sheet metal forming operations [14]. Therefore, bendability is an essential forming attribute, particularly in the automotive industry, where it is required for joining the outer sheet to the inner panel to create an aesthetically pleasing joint. The bendability of age-hardenable aluminum alloys is not yet well understood, due to their complex microstructure which is a result of various processing and compositional aspects, and can have a major impact. However, several studies have correlated the bendability of a material with its ductility [15,16]. Datsko and Yang [16] proposed that bendability improves with increasing reduction in area (i.e. true fracture strain) measured via tensile tests, and it was reported that bendability decreases with increasing hardness during natural aging [17,18]. Bendability can also be affected by grain boundary precipitates (grain boundary debonding in the early stages of bending due to weak grain adhesion) [19], the shape, size and fraction of Fe-rich IMPs [20,21], grain size [22,23] and crystallographic texture [24–26].

Damage during bending in Al-Mg-Si alloys usually occurs via two main mechanisms: (i) Transgranular fracture, resulting from strain localization and intense shearing [19]. In this regard Fe-rich primary IMPs are generally considered harmful, especially those with high aspect ratios. Their fracture and/or separation from the matrix creates voids, which soften the matrix material and contribute decisively to the formation of shear bands. The resulting localized deformation ultimately leads to damage formation, which is also reflected in reduced bending ability [20,27–30]. (ii) Intergranular failure due to a reduction in the local cohesive stress caused by the presence of heterogeneously nucleated grain boundary precipitates and the localization of deformation in soft precipitation-free zones adjacent to the grain boundaries, which is primarily the result of improperly applied heat treatment [19]. Therefore the formation of grain boundary precipitates (Mg_2Si and Si), e.g. due to slow cooling after solution annealing, has been observed to degrade the bending performance of Al-Mg-Si alloys [17]. Coarse grains or bands of similar oriented grains can promote the formation of surface inhomogeneities after pre-strain and during bending, thereby facilitating easier surface strain localization and shear banding [18,20,22]. Finer grain size is typically associated with better fracture resistance [14] and a less pronounced surface roughness [31] after deformation (orange peeling [32] i.e. the development of surface undulations [25]).

We recently demonstrated that Fe-rich IMPs in Al-Mg-Si-Fe crossover alloys can be optimized in their size and morphology via thermomechanical processing, to achieve very attractive levels of strength and ductility [12]. Even coarse IMPs resulting from slow solidification rates typically applied during direct chill casting can be tuned in this manner, making this strategy extremely interesting for industrial mass production. EN-AW 6016 forms the basis for this crossover approach; it is the preferred Al material for autobody sheets in Europe as it allows flat hems even on parts with local pre-deformation [33].

In this study we address the bending performance of Al-Mg-Si-Fe crossover alloys, which are capable of massive Fe uptake from recycling, under four different process conditions.

6.2 Experimental

The alloys used in this study were synthesized by remelting EN-AW 6016 sheet material. Iron (75% Fe and 25% Al reagent) and silicon (100% Si reagent) were added (contents in wt.%). The chemical compositions of the experimental alloys, as determined by optical emission spectrometry, are given in Table 6-1.

Table 6-1: Chemical compositions of the sample alloys (contents in wt.%).

Alloy	Si [%]	Fe [%]	Mn [%]	Mg [%]	Description
Ref.6016	1.07	0.18	0.06	0.33	Reference alloy
Si constant at 1.1%					
0.8Fe1.1Si	1.09	0.78	0.07	0.35	↑Fe
1.5Fe1.1Si	1.12	1.49	0.08	0.35	↑↑Fe
Si-adapted					
0.8Fe1.5Si	1.48	0.81	0.07	0.35	↑Fe-↑Si
1.5Fe1.9Si	1.90	1.50	0.08	0.34	↑↑Fe-↑↑Si

Formation of intermetallic AlFeSi primary phases consumes a significant amount of Si. To account for this and to ensure that equivalent amounts of magnesium and silicon were in solid solution at the solution treatment temperature, the silicon content was deliberately raised alongside the increase in iron for alloys 0.8Fe1.5Si and 1.5Fe1.9Si (calculated using FactSage 8.3 database FTlite 2023).

To achieve fast solidification conditions (cooling rate ≈ 60 °C/s) an INDUTHERM MC100V induction furnace was used to synthesize the test alloys, which were poured (casting temperature 760 °C) into a rectangular copper mold (capacity 100 g) at room temperature (RT). To vary casting conditions, a resistance-heated tilt furnace (Nabertherm K20/13/S) was used in combination with a mold coupled to a heat exchanger to mimic the solidification rate inherent in industrial direct chill casting processes (described in [34]). Argon-degassing was performed to remove dissolved gases and oxide inclusions. AlTi5B1 served as an inoculant to improve the solidification condition. At a casting temperature of 760 °C, the molten metal was poured into a preheated (~250 °C) steel mold, producing ingots of around 8 kg. An ionic liquid heat exchanger was used as the cooling medium. A cooling rate of about 3 °C/s, similar to that of a continuous casting process, was achieved. After casting, the alloys were subjected to a homogenization treatment at 560 °C with a heating time of 8

h (average heating rate of 1.125 °C/h), followed by a holding time of 11 hours. The rolling process involved hot-rolling at approximately 550 °C with a laboratory rolling mill from 12 mm to 7.3 mm. After hot rolling, the sheets were cooled either fast (cooling period ≈ 10 min) or slow (cooling period ≈ 45 h), whereby the slow cooling was intended to reflect the situation during industrial cooling in the coil. Subsequent cold rolling was carried out up to a sheet thickness of 1.2 mm, with intermediate annealing at 550 °C for 1 h, followed by fast (≈ 10 min) or slow cooling (≈ 45 h) at a thickness of 3.1 mm. Afterwards, sheets were solution annealed at 560 °C in a contact press (fast heating rate of ~ 70 °C/s), quenched in water at RT, and naturally aged at 25 °C for 14 days. In total the final sheets underwent four different thermal paths during processing. These are described in Table 6-2.

Table 6-2: Process routes applied for the test alloys.

Abbr.	Process routes and explanation of abbreviations
FFF	Fast (**F**) solidification (≈ 60 °C/s) → hot rolling and fast (**.F**) cooling to RT in ~ 10 min → cold rolling with intermediate annealing (fast (**..F**) cooling to RT in ~ 10 min) → solution annealing 2 min
SFF	Slow (**S**) solidification (≈ 3 °C/s) → hot rolling and fast (**.F**) cooling to RT in ~ 10 min → cold rolling with intermediate annealing (fast (**..F**) cooling to RT in ~ 10 min) → solution annealing 2 min
SSS	Slow (**S**) solidification (≈ 3 °C/s) → hot rolling and slow (**.S**) cooling to RT in ~ 45 h → cold rolling with intermediate annealing (slow (**..S**) cooling to RT in ~ 45 h) → solution annealing 2 min
SSS+1h	Slow (**S**) solidification (≈ 3 °C/s) → hot rolling and slow (**.S**) cooling to RT in ~ 45 h → cold rolling with intermediate annealing (slow (**..S**) cooling to RT in ~ 45 h) → solution annealing 1 h (**+1h**)

For mechanical characterization three-point bending tests were performed in accordance with VDA 238-100 [35] using a Zwick/Roell Z 100 model testing machine to evaluate bendability after 14 days of natural aging (T4) at RT. Prior to bending, 10% plastic strain was applied in the rolling direction (RD), reducing the sheet thickness from 1.2 mm to ~ 1.15 mm. The bending punch (radius 0.2 mm) was oriented perpendicular to the RD. For process conditions SSS and SSS+1h bendability was also evaluated by a bending punch setup oriented parallel to the RD, but the direction of the pre-strain was the RD (equal to that of the other test set). The samples were supported by two cylinders (cylinder spacing 2.8 mm) that could rotate freely and were bent until a force drop of 30 N (associated with

crack formation) was measured. A goniometer was utilized to manually measure the plastic component of the maximum bending angle. Bending tests to a 180 ° angle using different bending punch radii (i.e. hemming) were also performed according to [36] for process route SFF perpendicular to the RD in T4 condition. The purpose of this was to evaluate the $\frac{r_{min}}{t}$ ratio, where r_{min} represents the minimum punch radius over which the sheet can be bent without crack formation and t is the sheet thickness. For this setup the gap between the cylinders was kept at $2r + 2t$. Tensile tests were carried out after 14 days of natural aging at RT using a Zwick/Roell Z 100 model testing machine. A strain rate of 0.0032 s^{-1} with a gauge length of 45 mm in the rolling direction was set.

For microstructural analysis, cross-section planes of the sheet material which included rolling (RD) and normal (ND) directions were prepared using standard metallographic procedures. A scanning electron microscope of type JEOL-7200F was utilized for examination. The size and area fractions of primary phases and pores were assessed by feature analysis, an automated EDX analysis based on backscattered electron (BSE) threshold micrographs implemented in Oxford Aztec software, and an ImageJ software package. Secondary electron (SE) contrast was used to observe the fracture surfaces. Electron backscatter diffraction (EBSD) was carried out to create inverse pole figure (IPF-Z) orientation maps using a Symmetry S2 detector from Oxford Instruments at an acceleration voltage of 20 KV. Data analysis was performed with the Aztec Crystal software package and the mtex toolbox [37].

6.3 Results

6.3.1 Bendability after thermomechanical processing

Figure 6-1 shows the results of the three-point bending tests on the experimental alloys after 14 days of natural aging and 10% plastic strain. First, we consider alloys according to the FFF process. The highest bending angles were obtained for the reference 6016. Interestingly, the alloys with low Si content and high Fe content show surprisingly good bendability. Even 1.5% Fe did not result in a deterioration of the maximum bending angle when comparing alloy 0.8Fe1.1Si (150 °) with 1.5Fe1.1Si (151 °) under process condition FFF. However, if the Si content is increased along with the Fe content (to account for its incorporation into AlFeSi-phases), a drop in the maximum bending angle is observed for 0.8Fe1.5Si (134 °) and especially for 1.5Fe1.9Si (107 °).

By changing the process condition from fast (FFF) to slow (SFF) solidification conditions, a slight drop in bendability can also be recognized, except for alloy 1.5Fe1.1Si, where a slight increase can actually be observed. Processing by SSS (slow solidification, slow cooling after hot rolling and slow cooling after intermediate annealing) caused a serious reduction in bendability for all alloy compositions. However, when extending the solution annealing treatment at 560 °C to 1 h (SSS+1h), the bending performance could be restored to values comparable to those of SFF or FFF processes.

Bending capacity parallel to the RD was also evaluated for the SSS and SSS+1h conditions, which are associated with a reduction in bending angle for all alloys, as shown in Figure 6-1 (white outline color in the bar graphs).

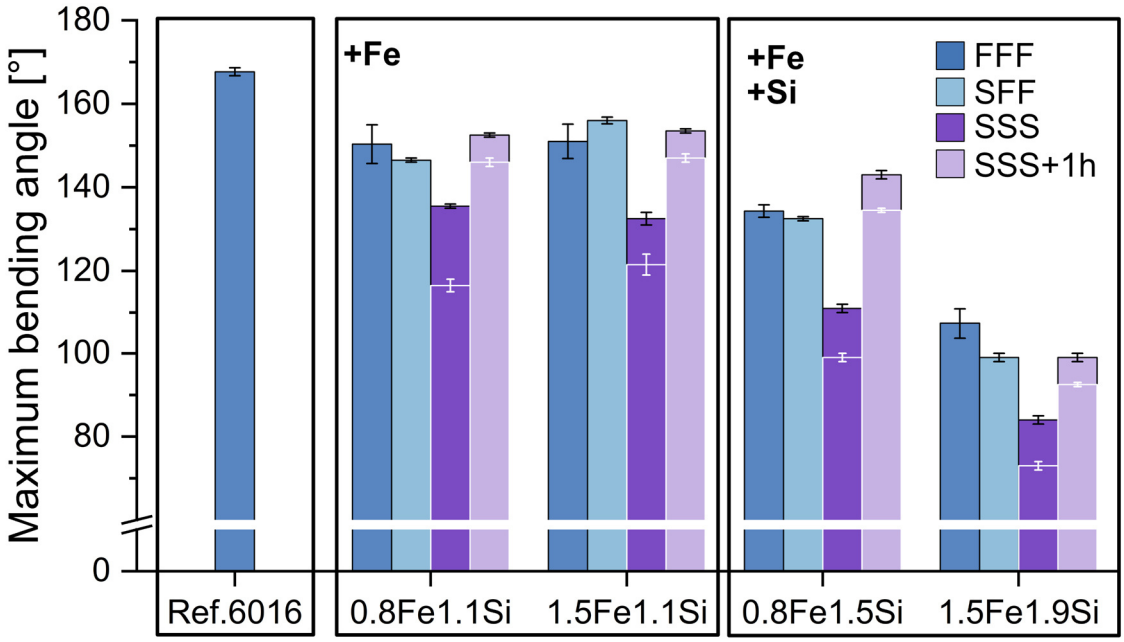

Figure 6-1: Maximum bending angle (punch axis parallel to transverse direction) for process conditions FFF, SFF, SSS and SSS+1h perpendicular to the RD. For the SSS and SSS+1h process conditions, the bending angle was also measured using a bending punch setup oriented parallel to the RD. This setup is associated with the lower values in the bar graphs (white outlines).

Table 6-3 presents the results of 180 ° bending (i.e. hemming) tests evaluated for the SFF process condition after 14 days of natural aging and 10% plastic pre-strain. Performance (lower $\frac{r_{min}}{t}$ ratio) is superior for alloys without additional Si.

Table 6-3: Results of 180 ° bending tests for the SFF process condition after 14 days of natural aging and 10% plastic pre-strain.

Alloy	**Sheet thickness t [mm]**	**Minimum bending punch radius r_{min} [mm]**	**$\frac{r_{min}}{t}$ ratio [-]**
0.8Fe1.1Si	1.13	0.6	0.53
1.5Fe1.1Si	1.13	0.6	0.53
0.8Fe1.5Si	1.15	0.8	0.70
1.5Fe1.9Si	1.16	1.2	1.03
Ref.6016	1.11	0.2	0.18

6.3.2 Microstructure analysis

Figure 6-2 illustrates the microstructural characteristics associated with process FFF (fast solidification and cooling conditions). Prior to bending, the BSE micrographs display the morphology, size, and distribution of IMPs, while the IPF-z orientation maps depict grain size and structure. During thermomechanical processing, the iron-rich intermetallic primary phases, identified as Al(Fe,Mn)Si-phases [12,13], fragmented significantly, resulting in finely dispersed particles with a mean equivalent circular diameter (ECD) of approximately 1.0 μm. The effect of particle fragmentation and their control in size and morphology, as well as the positive effects of Fe-rich IMPs on grain size and mechanical properties, was described in our prior work in [12]. These particles are aligned along the rolling direction and exhibit an elongated or blocky morphology with rounded edges. An increase in IMP content (Table 6-4) leads to a reduction in grain size, which can be attributed to an enhanced nucleation rate during recrystallization due to particle stimulated nucleation [12,38,39]. During cold rolling an increased dislocation density is generated near the interfaces of iron-rich IMPs, which act as favorable locations for newly formed grains [38–40]. After bending to failure, BSE micrographs were taken approximately 100 μm from the outer bending surface, revealing dark spots close to or in IMPs. These dark areas are cavities, which typically occur due to cracking of coarse Fe-rich IMPs, in particular those with a high aspect ratio [41], or through matrix decohesion of IMPs caused by dislocation pile-up stresses at the particle-matrix interface [42]. Their development can be clearly seen by comparing the inserts in the BSE micrographs before and after bending. Elongated IMPs usually break in the center of their longitudinal axes.

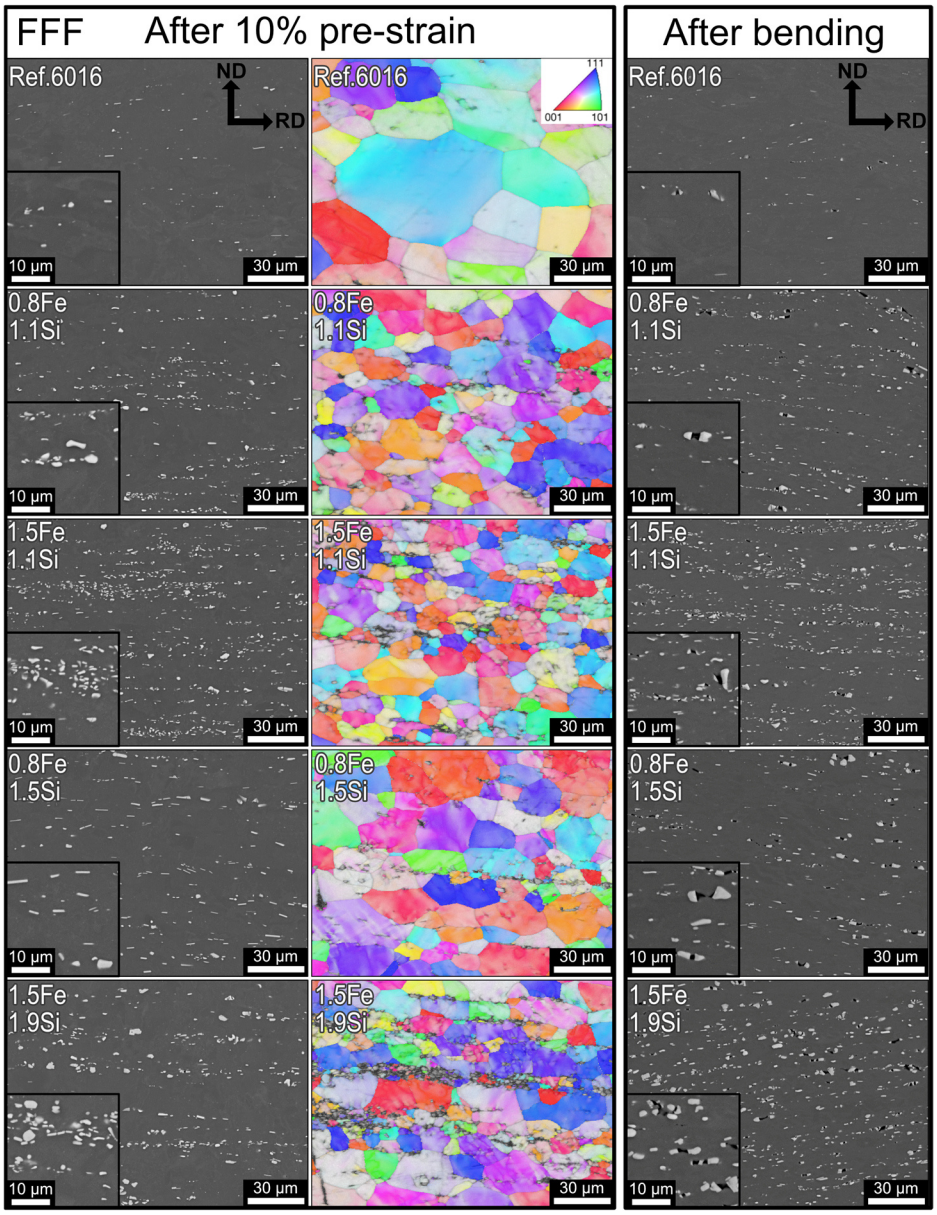

Figure 6-2: BSE micrographs and IPF-z maps after 10% of pre-strain (before bending) for process route FFF (fast solidification and cooling conditions). The corresponding BSE micrographs after bending were captured at ~100 µm distance from the outer bending surface. Bottom left corner shows magnified image of area of interest.

Figure 6-3 depicts the microstructure associated with process SFF (slow solidification and fast cooling conditions). Prior to bending, BSE micrographs and EBSD data were used to evaluate IMPs and grain size. When comparing the SFF with the FFF process route, the main microstructural difference is an increase in the size of the fragmented primary phase particles from ~1 µm to ~1.6 µm and a coarser grain structure (see Table 6-4). After bending, the BSE micrographs show dark areas between and next to IMPs, which can be classified as voids resulting from IMP fracture. Counting the voids created by IMP fracture, the two variants FFF and SFF provide roughly comparable values.

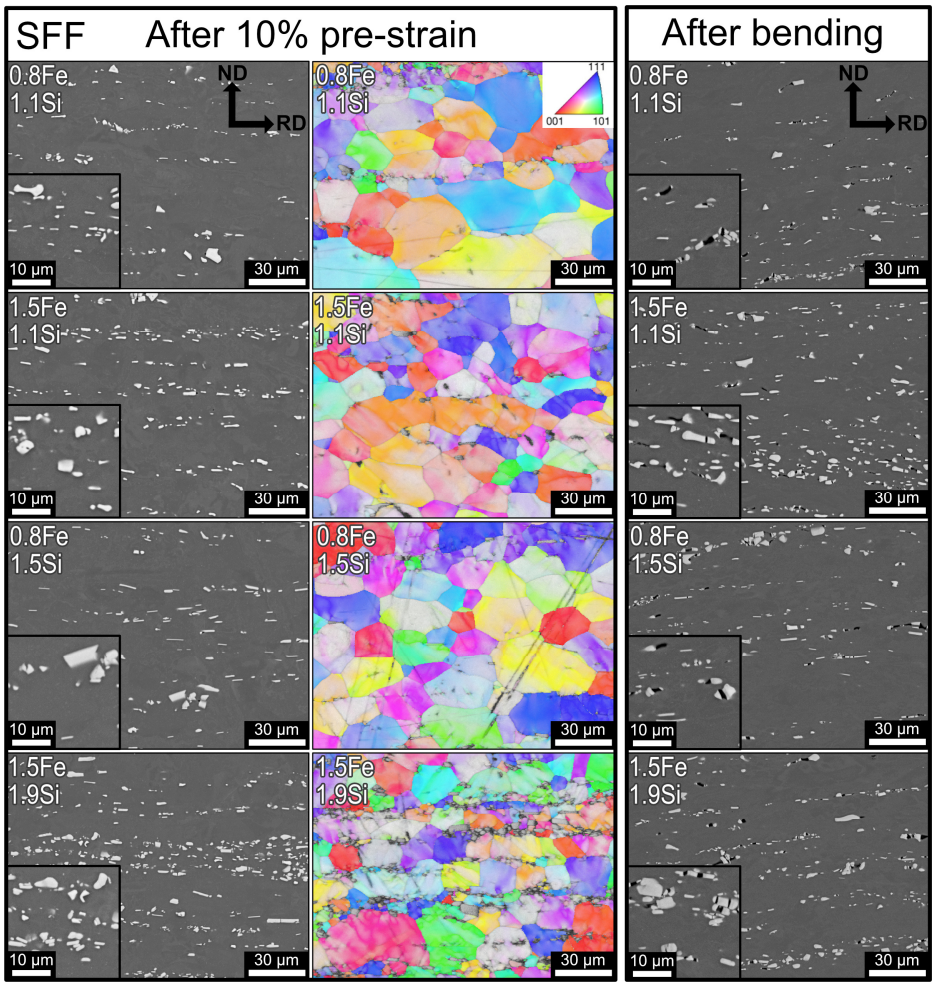

Figure 6-3: BSE micrographs and IPF-z maps after 10% of pre-strain (before bending) for process route SFF (slow solidification and fast cooling conditions). The corresponding BSE micrographs after bending were captured at ~100 µm distance from the outer bending surface. Bottom left corner shows magnified image of area of interest.

Figure 6-4 now compares the microstructural characteristics after 10% pre-strain and after bending to failure (approximately 100 µm from the outer bending surface) for SSS (slow solidification and cooling conditions, 2 min solution annealing) and SSS+1h (slow solidification and cooling conditions, 1 h solution annealing). The microstructures of process SSS and SSS+1h are similar to those seen in the SFF thermal history in terms of grain size, ECD, distribution and area fraction of IMPs (see Table 6-4). In contrast to the process routes FFF and SFF, dark spots are now visible in the BSE micrographs even prior to bending, with a spherical morphology for processes SSS and SSS+1h. These areas represent either pores or phases with a lower atomic number than the aluminum matrix, probably formed during slow cooling after intermediate annealing. EDX map analysis revealed that, on average, only ~2% of the analyzed dark spots are Mg_2Si, while the rest are pores. Additionally, no significant grain growth was observed after the one-hour solution annealing treatment at 560 °C, except in alloy 1.5Fe1.9Si, which exhibited a slight increase in ECD compared to the SSS condition (Table 6-4). After bending, additional microvoids form, mainly due to the fracture of IMPs in the outer layer, which are exposed to high strains.

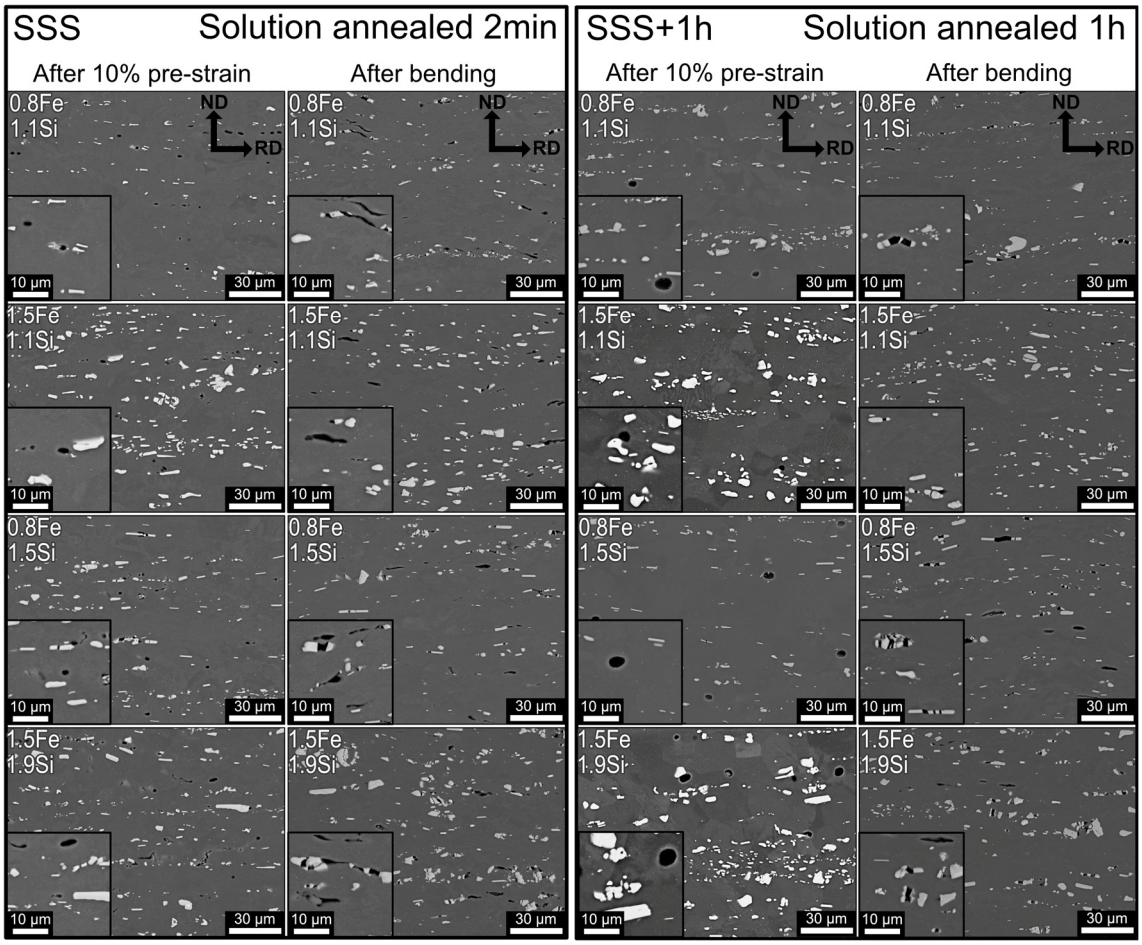

Figure 6-4: BSE micrographs after 10% of pre-strain (before bending) for process routes SSS (slow solidification and cooling conditions, 2 min solution annealing) and SSS+1h (slow solidification and cooling condition and 1h solution annealing), with the corresponding BSE micrographs after bending captured at ~100 µm distance from the outer bending surface. Bottom left corner shows magnified image of area of interest.

Figure 6-5a shows the area fraction and size of pores for the slow-cooled material after 2 min solution annealing (SSS) and 1 h solution annealing (SSS+1h) before bending. The Si-adapted alloys (0.8Fe1.5Si and 1.5Fe1.9Si) exhibit a much higher porosity than their Fe equivalents (0.8Fe1.1Si and 1.5Fe1.1Si). One hour of solution annealing also generates a significant decrease in the area fraction of the pores, while at the same time the average pore diameter increases (in particular the large pores grew significantly: see the upper value of the standard deviation). Figure 6-5b shows an example of the pore size distribution after the SSS and SSS+1h processes for the 0.8Fe1.5Si alloy. A severe decrease in the number of pores and a shift to larger diameters is evident for SSS+1h.

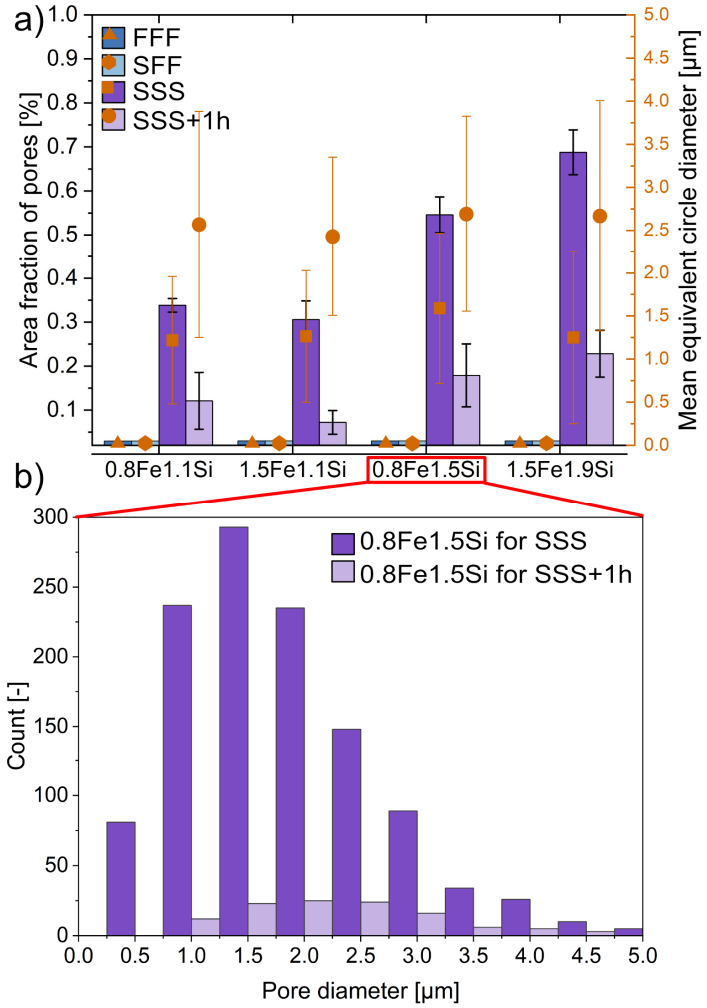

Figure 6-5: (a) Pore size and area fraction of pores under process conditions SSS (2 min solution annealing at 560 °C) and SSS+1h (1 h solution annealing at 560 °C) for alloys 0.8Fe1.1Si, 1.5Fe1.1Si, 0.8Fe1.5Si and 1.5Fe1.9Si (Area surveyed ~0.6 mm2, error bars indicate the standard deviation) and (b) illustration of the size distribution of pores following processes SSS and SSS+1h for alloy 0.8Fe1.5Si.

Table 6-4: Grain size, mean ECD and area fraction of IMPs for the test alloys for process routes FFF, SFF, SSS and SSS+1h. The area surveyed for grain size and particle size was ~0.8 mm2 (± refers to the standard deviation)

Process route	Mean ECD of grains [µm]	Mean ECD of IMPs [µm]	Area fraction of IMPs [%]
Ref.6016	23.8 ± 12.3	0.6 ± 0.3	0.3 ± 0.1
FFF			
0.8Fe1.1Si	11.1 ± 7.9	1.0 ± 0.6	2.1 ± 0.4
1.5Fe1.1Si	8.0 ± 4.6	1.0 ± 0.5	4.0 ± 0.4
0.8Fe1.5Si	11.6 ± 7.5	1.1 ± 0.7	2.2 ± 0.3
1.5Fe1.9Si	8.7 ± 6.2	1.1 ± 0.7	5.0 ± 0.6
SFF			
0.8Fe1.1Si	16.8 ± 9.3	1.5 ± 1.0	2.5 ± 0.3
1.5Fe1.1Si	13.3 ± 6.7	1.7 ± 1.1	4.1 ± 0.1
0.8Fe1.5Si	16.0 ± 8.2	1.6 ± 0.9	2.7 ± 0.1
1.5Fe1.9Si	12.8 ± 7.3	1.4 ± 0.9	5.1 ± 0.5
SSS			
0.8Fe1.1Si	15.3 ± 8.1	1.3 ± 0.9	2.2 ± 0.3
1.5Fe1.1Si	13.1 ± 6.5	1.6 ± 1.1	4.1 ± 0.2
0.8Fe1.5Si	17.6 ± 9.2	1.5 ± 1.0	2.5 ± 0.5
1.5Fe1.9Si	13.8 ± 6.9	1.7 ± 1.3	4.9 ± 0.3
SSS+1h			
0.8Fe1.1Si	15.3 ± 10.3	1.3 ± 0.9	2.5 ± 0.3
1.5Fe1.1Si	14.1 ± 8.1	1.6 ± 1.1	3.9 ± 0.3
0.8Fe1.5Si	17.2 ± 10.7	1.6 ± 1.1	2.7 ± 0.3
1.5Fe1.9Si	16.0 ± 8.6	1.7 ± 1.2	4.9 ± 0.7

6.3.3 Results of tensile tests

Figure 6-6 displays the technical stress-strain curves of the test alloys in RD for process route SFF after 14 days of natural aging. The silicon-adapted alloys (0.8Fe1.5Si and 1.5Fe1.9Si) exhibit increased strength, paired with high total elongation – despite their high content of brittle IMPs. Alloys without additional Si displayed comparable yield and tensile strengths. In both groups, the Fe-rich alloys demonstrated greater work hardening, which is even more pronounced for the Si-adapted variants. The key aspects for the higher strength, the improved work hardening and the high elongation measured in the tensile tests are grain refinement and the intensified formation of geometrically necessary dislocations around Fe-rich IMPs during plastic deformation, detailed explanations are given in our prior work [12]. Since bending tests were performed after 10% of plastic pre-strain, it is

important to note that the difference in strength between the alloys is equal to their yield strength plus the corresponding amount of work hardening of the material. Accordingly, the decisive strengths of the Si-corrected alloys 0.8Fe1.5Si and 1.5Fe1.9Si are significantly higher than those of the alloys with 1.1Si.

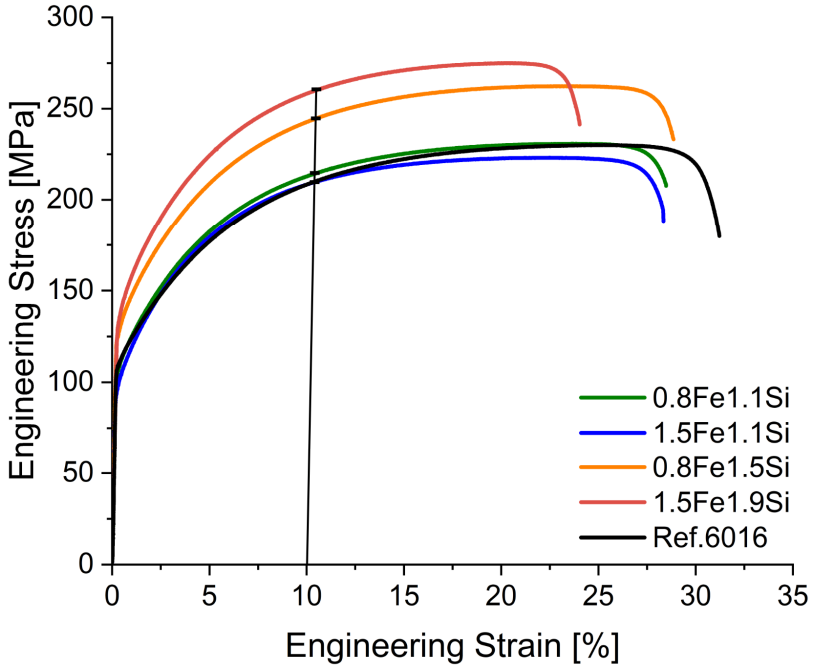

Figure 6-6: Technical stress-strain curves of the test alloys in (RD = tensile direction) for process route SFF after 14 days of natural aging indicating 10% pre-straining prior to bending.

6.3.4 Bending defect analysis

Figure 6-7 depicts microstructural features of the alloys 0.8Fe1.1Si and 1.5Fe1.9Si following the FFF process after bending to failure. Figure 6-7 shows (a) shear bands formed during bending visualized by EBSD band contrast, superimposed with EDX (IMPs shown in red, detected by high Fe content), (b) BSE micrographs of the crack and (c) the fracture surfaces by using SE contrast. In this state, the alloys show a considerable difference in the bending angle, 150 ° and 107 ° respectively. In all alloys and conditions shear bands are oriented ~45 ° to the outer surface and the direction of max. strain. The softer alloy FFF 0.8Fe1.1Si exhibits a wide agglomerate of parallel narrow shear bands associated with a high density of lattice defects in its vicinity (shown by lower band contrasts in darker grey values). In contrast, the alloy FFF 1.5Fe1.9Si with higher flow stress exhibits a sharp, pronounced shear band with fewer signs of plastic deformation in its neighborhood, which indicates a lower energy fracture progress. For the 0.8Fe1.1Si alloy a wider opening angle of the crack can be observed, and also a more blunt crack tip. The penetration depth is, at 160 µm, about 25% lower than the 210 µm of the 1.5Fe1.9Si alloy (starting point on the surface not shown in Figure 6-7). At this point it is also worth noting, that the failure criterion and therefore the end of loading was in all experiments at a Force drop of 30 N. In both examples, the cracks do not appear to follow the Fe-rich IMPs, initially

aligned along the RD (see Figure 6-7b). The fracture surfaces in Figure 6-7c for alloys 0.8Fe1.1Si and 1.5Fe1.9Si both exhibit clear dimple formation, indicating a transgranular ductile fracture mechanism via void growth and coalescence. The dimensions of the dimples in 0.8Fe1.1Si are slightly larger and appear deeper than those in alloy 1.5Fe1.9Si. The difference is probably due to the different nucleation density of cavities, which is linked to the interparticle spacing [43] and the number of IMPs present. The characteristics of crack formation shown are representative of all alloys produced under the process routes described in Table 6-2.

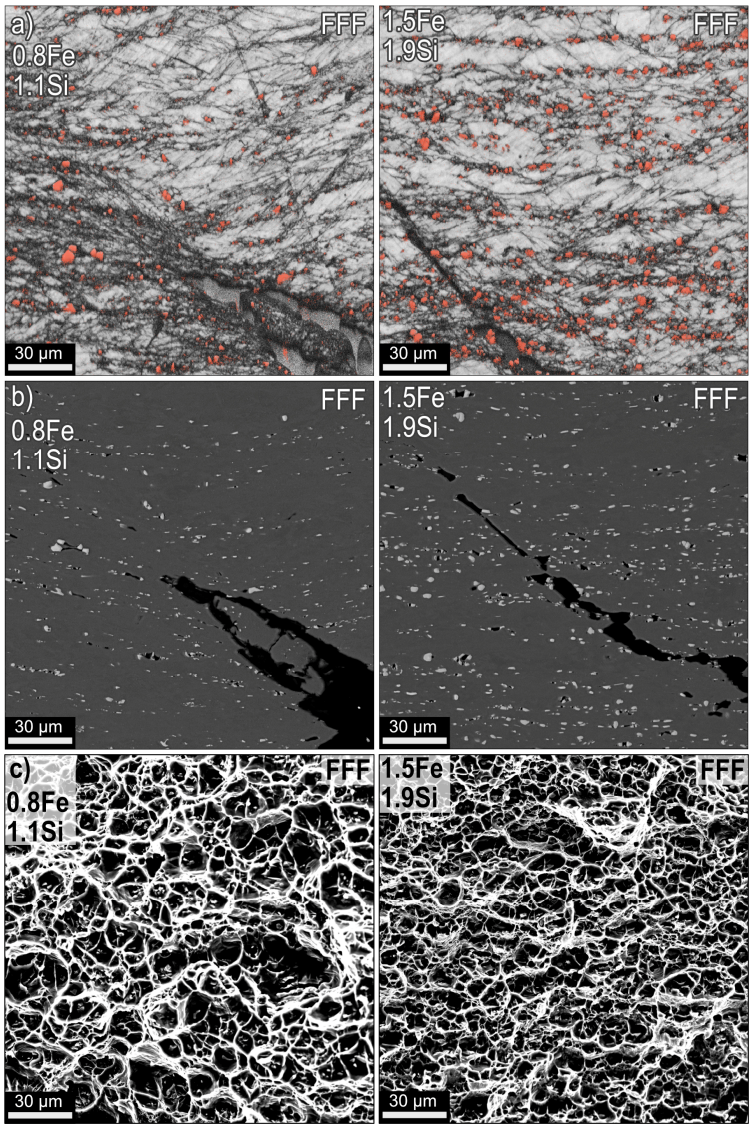

Figure 6-7: After process FFF for alloys 0.8Fe1.1Si and 1.5Fe1.9Si: (a) Shear band visible using EBSD band contrast overlaid with EDX (IMPs are shown in red); (b) BSE micrographs showing the macroscopic crack; and (c) SE micrographs of the fracture surface.

6.4 Discussion

Iron is commonly considered an impurity element in aluminum alloys, and is therefore subject to limitations [2,7]. Exceeding these limits is usually reported to result in a decrease in ductility and formability [2,7]. Traditionally an increase in iron content is accompanied by a deterioration of bending properties [15,20,44]. However, Lievers' work [20] shows only a very moderate decrease; and also in [44] no degradation in bendability was observed for soft annealed AA5754, at low and high Fe content.

Both the effect of Fe and Fe+Si and the influence of the process routes investigated in this study are graphically summarized in Figure 6-8. The outline color of the micrographs indicates a rating of their bendability (red: <130 °, yellow: 130–145 °, green: >145 °). Surprisingly, alloys 0.8Fe1.1Si and 1.5Fe1.1Si achieved high bending angles despite their high content of brittle IMPs, while adding Si (0.8Fe1.5Si and 1.5Fe1.9Si) resulted in a significant reduction in bendability. For slow solidification conditions (SFF processing route), the IMPs were generally larger in size, which did not cause a significant decrease in bendability. If pores are present (process SSS) a severe degradation in bending capacity was observed for all alloys. One hour of solution annealing generated an almost restored bendability, comparable to that associated with the FSS and FFF process conditions. The discussion below addresses the effects of various process and microstructure conditions on the bendability of Al-Mg-Si-Fe crossover alloys based on the overview presented in Figure 6-8.

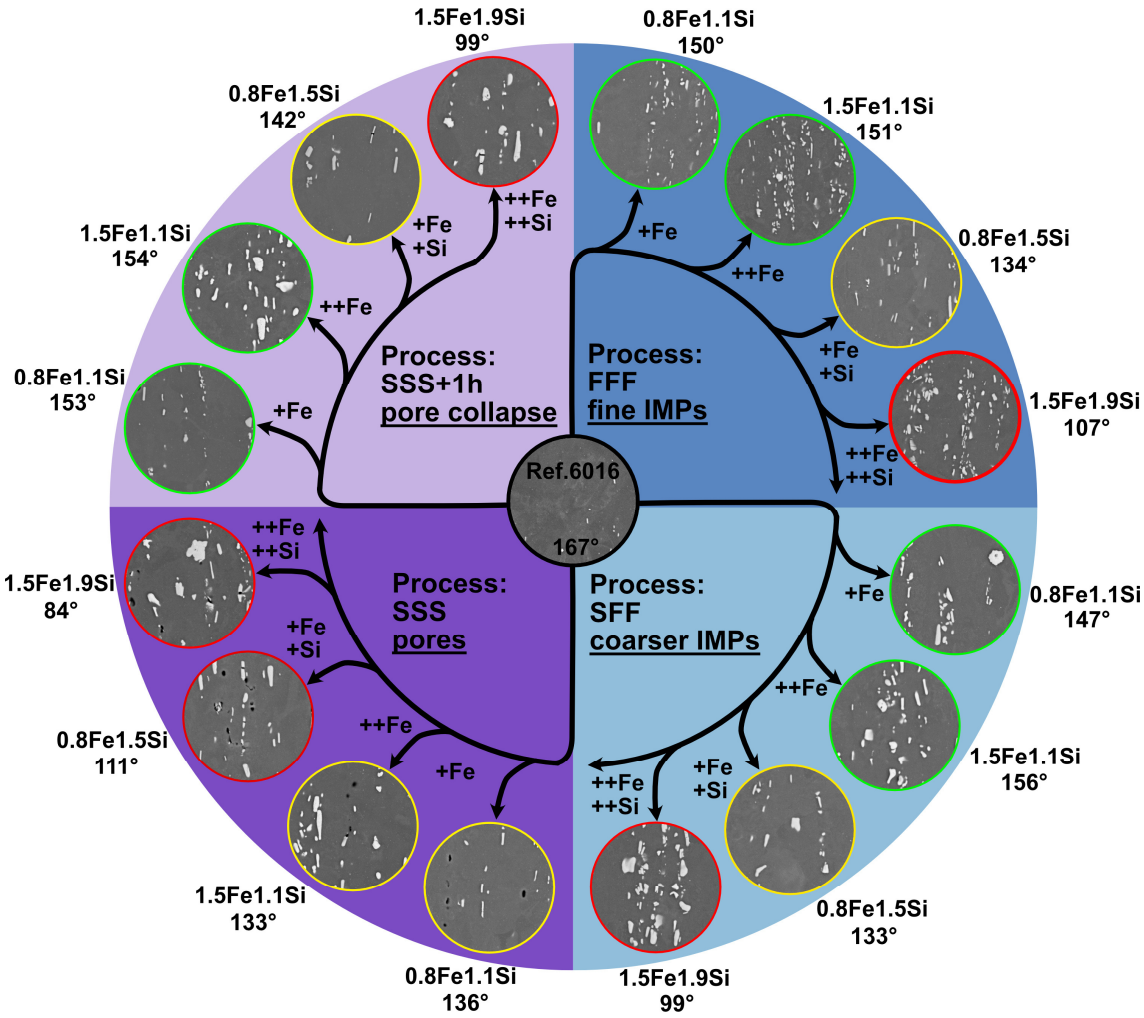

Figure 6-8: The effects of extensive addition of alloying elements (Fe, Si) and the applied process conditions (expressed in varying IMP sizes and pore content) on bendability in alloy base 6016 (red: <130 °, yellow: 130–145 °, green: >145 °).

6.4.1 Effect of primary phase content and matrix strength on bendability

When discussing the bendability of Al-Mg-Si-Fe crossover alloys based on the results displayed in Figure 6-1 and Table 6-3 (hemming experiments), two notable effects emerge: Firstly, there was no deterioration in the maximum bending angles and the $\frac{r_{min}}{t}$ ratios when comparing alloys 0.8Fe1.1Si and 1.5Fe1.1Si, despite a significantly increased content of Fe-rich IMPs. This was observed for all process conditions tested.

Secondly, despite the (initially) identical appearing microstructures obtained for Fe-equivalent alloys, a significant reduction in bendability is observed, particularly when comparing alloy 1.5Fe1.1Si with 1.5Fe1.9Si. Therefore, silicon in solid solution, which as Figure 6-6 shows is associated with higher strength and strain hardening, must be considered a critical factor. The grain size, size, morphology and IMP content of the 0.8Fe1.1Si and 1.5Fe1.1Si alloys are considered equivalent when compared to the Fe-equivalent 0.8Fe1.5Si and 1.5Fe1.9Si alloys (Table 6-4). Both fast (FFF) and slow (SFF)

solidification conditions demonstrate this equivalence. The material processing, including intermediate annealing, and the increased number of IMPs result in a weak texture overall. The dominant texture component is the rotated cube (45 ° in ND, {001]<110>), which was analyzed in previous work [12]. The J-index of the computed Orientation Distribution Functions, with a kernel halfwidth of 7 °, consistently exhibits values below 1.32 across all instances. This means that a significant texture influence on the bendability of the tested alloys can be largely ruled out in the case investigated here.

Many forming procedures are constrained by plastic instability caused by neck formation. However, certain sheet forming operations, such as bending, encounter limitations due to damage as necking tendencies are mitigated [20]. Crack initiation and propagation during bending are affected by second phase particles, micro-voids and shear-bands [15]. The beginning of inhomogeneous deformation of grains, due to different grain orientations during bending, causes the formation of grain-level surface undulations [25]. Therefore, grain size is also an important factor to consider as it influences the development of surface roughness and controls strain localization and formation of a shear band originating from one of the deepest valleys formed [20,22]. In the region of progressive localized deformation, Al(Fe,Mn)Si constituent particles fracture under increasing stress, leaving micro-voids, which facilitates the propagation of a shear band and ultimate failure [20,25]. This agrees well with the damage shown in Figure 6-7. These voids continue to grow and coalesce, resulting in a transgranular ductile damage mechanism that is seen clearly in Figure 6-7c.

The true fracture strain measured by tensile tests can provide a good estimate of ductility [45], which can be correlated with bendability of the material [15]. In Figure 6-9 the true stress is plotted against the true strain for the test alloys after process SFF in T4 condition. Necking and fracture strain are marked by the square and circle symbols respectively. True fracture strain is slightly lower for the Si-adapted variants 0.8Fe1.5Si and 1.5Fe1.9Si compared to their Fe equivalents 0.8Fe1.1Si and 1.5Fe1.1Si, the latter featuring identical fracture strain values.

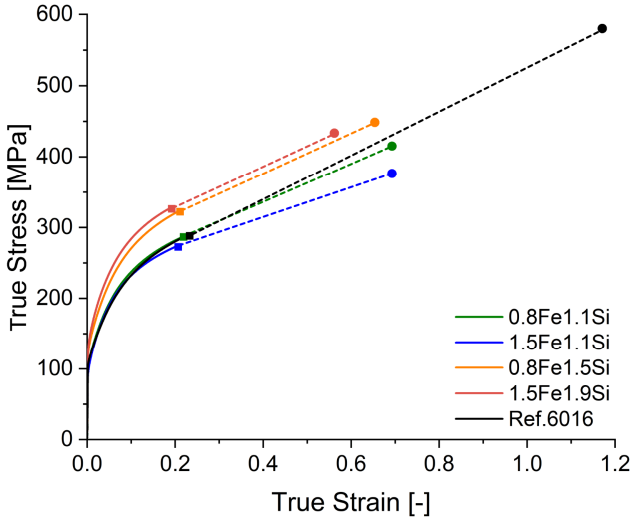

Figure 6-9: True stress - true strain of the test alloys after the SFF process in T4-condition. Necking and fracture strain are indicated by squares and circles respectively.

Bendability can commonly be quantified by the $\frac{r_{min}}{t}$ ratio [14], where r_{min} represents the minimum bending punch radius around which the sample can be bent without cracking, and t is the sheet thickness. A smaller $\frac{r_{min}}{t}$ ratio is equivalent to better bendability of the material. Datsko and Yang proposed an relation for ductile materials in which $\frac{r_{min}}{t}$ is linked with the reduction in area, RA, measured in tensile test [16,25]:

$$\frac{r_{min}}{t} = \frac{C}{RA} - 1 \qquad \text{(Eq. 6-1)}$$

with C as a constant, which is found empirically to be 0.6–0.7 for aluminum alloys [16,25]. With $\varepsilon_f = ln\frac{A_i}{A_f}$ and $RA = 1 - \frac{A_f}{A_i}$ the reduction in area RA can be linked to the true fracture strain ε_f:

$$RA = 1 - \frac{1}{exp\,(\varepsilon_f)} \qquad \text{(Eq. 6-2)}$$

According to Li [25], because 10% of pre-strain was applied in tension prior to bending, we need to subtract the pre-strain from the true fracture strain. The final sheet bendability increases with increasing true fracture strain:

$$\frac{r_{min}}{t} = \frac{C}{1 - \frac{1}{exp\,(\varepsilon_f - 0.1)}} - 1 \qquad \text{(Eq. 6-3)}$$

To test the alloy variations for the relation proposed by Datsko and Yang [16], Figure 6-10 plots the $\frac{r_{min}}{t}$ ratio against the true fracture strain. The graph indicates bendability based on equation 5 (C=0.7), which accords well with the experimentally determined data obtained from tensile and 180 ° bending (i.e. hemming) tests for process route SFF. Alloys 0.8Fe1.1Si and 1.5Fe1.1Si demonstrate equal true fracture strains as well as the same $\frac{r_{min}}{t}$ ratios at given process conditions.

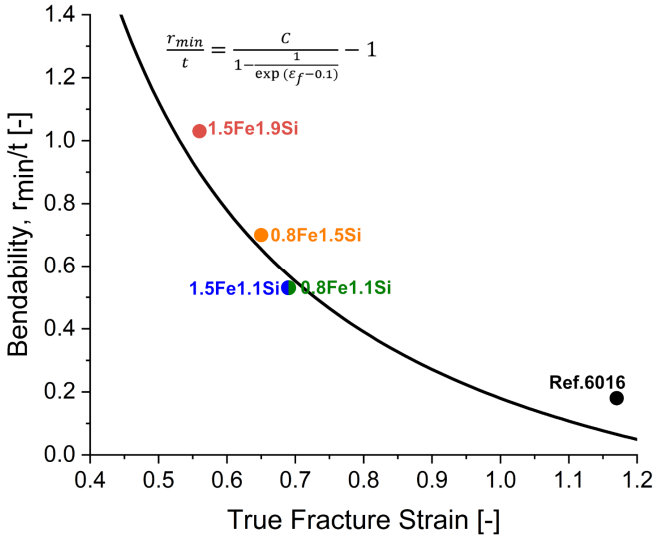

Figure 6-10: Correlation between bendability and true fracture strain for alloys after the SFF process route in T4 condition. The graph simulates bendability according to equation 3 (C=0.7).

Silicon in solid solution contributes to enhanced strength and strain hardening in alloys 0.8Fe1.5Si and 1.5Fe1.9Si, both of which feature the same amount of dissolved Si at solution annealing temperature. Their increased strength can be attributed to higher solid solution strengthening and more pronounced natural aging [12] compared to the Fe equivalents with lower Si, 0.8Fe1.1Si and 1.5Fe1.1Si. Additionally, strain hardening is more pronounced for alloys with adapted Si content, which can be explained by an increase in strain-induced clustering [46], because higher Si content facilitates the formation of more clusters [47]. Strain hardening is also more pronounced in alloys with higher numbers of IMPs due to the formation of geometrically necessary dislocations [12].

Due to the greater strength of the matrix and increased strain hardening (see stress level at 10% plastic pre-strain in Figure 6-6), dislocation pile-up stresses at IMPs can reach a critical value faster, causing brittle IMPs with an unfavorable orientation and morphology to fracture and to form microvoids. According to Lievers et al. [20,27], when many voids are generated by particle cracking the critical zone with the highest strains (located in the surface region); the initial surface inhomogeneity, combined with the softening effect of the evolving porosity, can facilitate the formation of shear bands. Increased Fe content, i.e. area fraction of IMPs, is not necessarily considered critical for bendability (compare alloy 0.8Fe1.1Si with 1.5Fe1.1Si), if the alloy matrix is soft. At lower yield strength, more plastic deformation is required for crack initiation at IMPs. Additionally, both a wide shear band and crack tip blunting can be observed in alloy 0.8Fe1.1Si in Figure 6-7, which inhibits crack growth. In contrast, the Si-corrected alloy 1.5Fe1.9Si, which exhibits greater strength and work hardening, demonstrates a sharply defined shear band and weak bendability.

A more uniform distribution of IMPs can help achieve more isotropic material properties during bending. As mentioned above, damage is also initiated via the growth of surface defects by localized shear [44]. In surface regions consisting of a high density of larger IMPs arranged in a chain-like structure in the RD, voids formed at IMPs located at or near the sheet surface can be considered as surface defects and aids to the development of shear bands. It can therefore be assumed that the probability of triggering a shear band through near-surface particle cracking is increased, which agrees well with the drop in bendability seen in all experimental alloys evaluated by a bending punch setup oriented parallel to the RD (Figure 6-1).

6.4.2 Effect of annealing pores on bendability

Figure 6-4 illustrates pores formed under process condition SSS prior to bending; Figure 6-5 shows the associated metallographic evaluation of area fraction and size. Obviously, the duration of solution annealing (2 min for SSS and 60 min for SSS+1h) has a major influence on the volume and diameter of the pores. The area fraction of voids is significantly lower after 1 h annealing at 560 °C. On the other hand, the pores' mean ECD is higher after a long annealing time. The following section

discusses the origin of pores, their effect on bendability and their change in volume and size during annealing treatment.

Figure 6-11 shows the predicted equilibrium phase fractions calculated using the FactSage 8.3 FTlite 2023 database for the 1.5Fe1.1Si and 1.5Fe1.9Si alloys as examples. The graphs correspond to the mass fractions of phases precipitated in thermodynamic equilibrium at a given temperature. Both 1.5Fe1.1Si and 1.5Fe1.9Si are Si-surplus alloys with the same amount of Mg_2Si (blue line) but differ in their Si phase fractions (red lines). In the SSS processing route, intermediate annealing is followed by very slow cooling to RT (~45 h), resulting in precipitation of Mg_2Si and Si. During the solution annealing treatment (2 min at 560 °C), Si and Mg_2Si dissolve and pores remain. Pore formation can be related to the Kirkendall effect, which has already been reported in Al alloys containing Mg_2Si [48] or Si [49]. Note that at 560 °C the diffusion coefficient of Mg and Si is significantly higher than that of the self-diffusion of Al (factor 23 for Mg and 6.6 for Si, calculated with mean values for D_0 and Q according to [50]), so that a net flow of vacancies at the location of the dissolved phases condenses to pores. Pores, which are formed by the dissolution of soluble phases in Al-Mg-Si-Cu-Zn-Fe alloys and which are responsible for reduced bendability, were also reported in [51].

Observations indicate that pores in a material negatively affect its bendability (see Figure 6-1). One existing explanation for this is that pores and/or voids promote the formation of shear bands [52,53]. It can be assumed that shear band formation and thus bending failure will occur earlier if the density of pores is greater. In fact, as illustrated in Figures 6-4 and 6-5, the Si-corrected alloys (0.8Fe1.5Si and 1.5Fe1.9Si), which exhibit a lower bending angle, exhibit a much higher area fraction of pores. Assuming a homogeneous distribution of spherical pores with diameter d, the porosity in terms of the distance between two pores can be estimated by using the measured area fractions, a_f, given in Figure 6-5. For the alloys with 1.1Si ($d \approx 1.25$ µm, $a_f \approx 0.3\%$) the average pore distance results in ≈ 19 µm and for the alloys with 1.5Si/1.9Si ($d \approx 1.5$ µm, $a_f \approx 0.62\%$) in ≈ 17 µm. Interestingly, these values roughly match the order of magnitude of the grain size, which is addressed later. After the one-hour annealing treatment, the mean pore spacing increases significantly, on average to 80 µm for the alloys with 1.1Si and to 45 µm for the alloys with 1.5Si/1.9Si, becoming significantly greater than the average grain size. Note that in addition to the increased number of pores, the greater strength and strain hardening of Si-corrected alloys forces the IMPs to fail earlier, creating additional voids which eventually generate sharp shear bands. This illustrates the negative effects of the adjusted Si content on bendability.

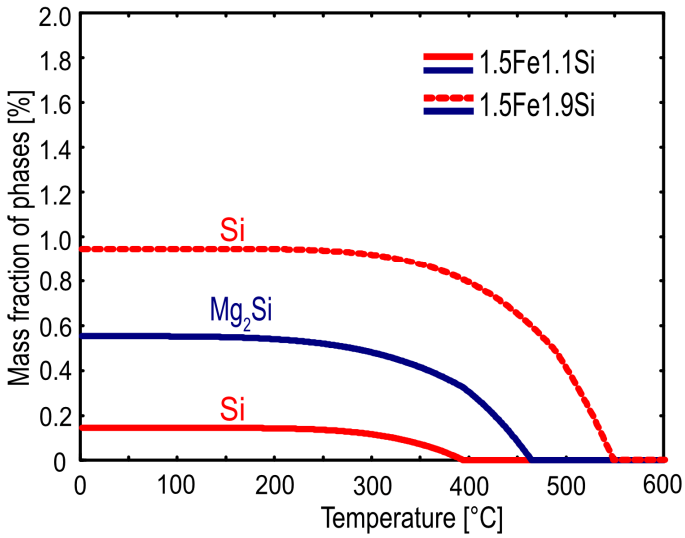

Figure 6-11: Predicted equilibrium phase fractions calculated using FactSage 8.3 database FTlite 2023 for alloys 1.5Fe1.1Si and 1.5Fe1.9Si.

As illustrated in Figure 6-5, a clear drop in the area fraction of pores can be observed after 1 h solution annealing (process SSS+1h), accompanied by an increase in bendability to the level of the SFF values. It is important to note that solution annealing for 1 h at 560 °C did not cause any changes to the size or area fraction of the IMPs. Neither, as Table 6-4 shows, was any significant grain growth observed. Thus, the increase in bendability can be attributed solely to the reduction in pore density caused by a decrease in pore volume (area fraction) and the simultaneous increase in the average size of the remaining pores. This in turn means that slow cooling after hot rolling has no direct influence on bending capacity, as SFF and SSS provide approximately the same bending angles after the pores have been mostly eliminated.

We will now take a closer look at the effect of the long solution heat treatment on the pore population. Here we observe a drastic decrease in the area fraction, but also an increase in the mean pore size. A change in pore size and its distribution after annealing treatment has been described in literature [54,55]. Ostwald ripening is assumed to be the dominant mechanism. This is also probably true in our case: the increase in average pore diameter can be considered a strong indication. Assuming two neighboring spherical pores with different radii r_1 and r_2, with $r_1 < r_2$ and thus different chemical potential $\mu(r_1) < \mu(r_2)$, atoms will migrate from the surface of the larger pore to the surface of the smaller. This results in the growth of the large pore at the expense of the small one, which finally disappears. However, the total pore volume remains unchanged.

In our case, such a process may take place at the beginning of the annealing treatment, namely when the pores are close to each other. However, if some pores disappear, it may be the case that the remaining pores are no longer located within the same grain but are separated by grain boundaries (note that, as mentioned above, the pore distance at the start of annealing is on the same order of magnitude as the grain size). In that case, as outlined by J. Sun [56], pore shrinkage results from the diffusion of atoms between the void surface and the adjacent grain boundary interface, which can act

as both a source or a sink for vacancies or atoms. It is important to note that in the case of atomic transport from the grain boundary to the pores, in contrast to Ostwald ripening, the pore volume decreases.

Sun [56] describes a model in which a pore of radius r is located in the center of an approximately spherical grain of radius R. Since $R > r$ the grain boundary interface has a higher chemical potential than the spherical void surface. Thus, the pore will shrink at the following rate:

$$\frac{dr}{dt} = \frac{2D\Omega}{kT} \frac{\frac{2\gamma_{gb}}{R} + \frac{2\gamma_s}{r}}{3R^2 - r^2 - \frac{2R^3}{r}} \left(r - \frac{R^3}{r^2} \right) \qquad \text{(Eq. 6-4)}$$

with D =1.11·10^{-13} m^2/s (self-diffusion coefficient of Al at 560 °C; D_0 = 6.6x10^{-6} m^2/s, Q = 124 kJ/mol [50]), Ω = 1.66·10^{-29} m^3 (atomic volume of Al), k = 1.38·10^{-23} J/K (Boltzmann constant), γ_{gb} = 0.32 J/m^2 (grain boundary interfacial energy of Al [57]), γ_s = 0.87 J/m^2 (surface energy of Al [58]) and R = 7·10^{-6} m (grain radius; see Table 6-4).

Figure 6-12 displays the pore shrinkage at T = 560 °C as a function of the pore radius r. According to this, small pores shrink orders of magnitude faster than large ones.

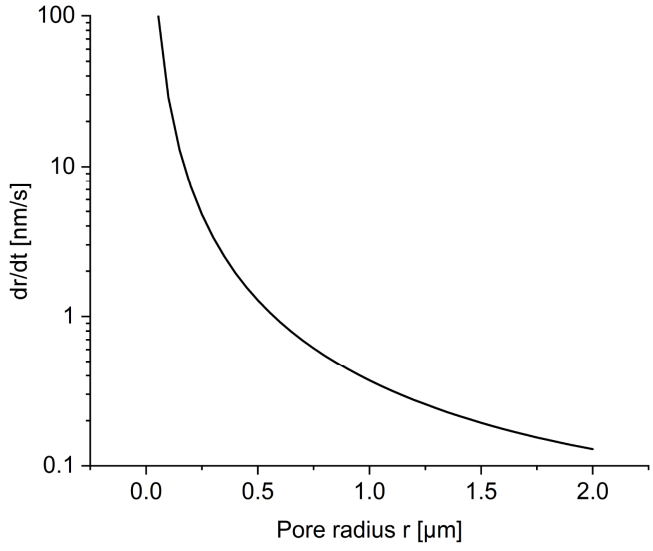

Figure 6-12: Rate of pore shrinkage at 560 °C as a function of the pore radius, calculated for a grain radius of µm.

We will now sketch the following possible scenario for our pore behavior during solution annealing for 1 h. In the early annealing phase, when pores are still present in large numbers and are located in the same grain, Ostwald ripening causes the large pores to grow at the expense of the small ones. The small pores disappear and at the same time the pore spacing of the enlarged pores increases, leading to separation of the pores by grain boundaries. Now pore shrinkage occurs due to atomic transport from the grain boundary. Since large pores shrink significantly more slowly than small pores it takes a few hours for pores with a diameter of 4 µm to shrink to half their size, but pores with a diameter of 1 to 2 µm shrink to half their size in just a few minutes. For our extended solution

annealing time of 1 h, this means that a large proportion of the pores are eliminated and the area fraction is correspondingly lower, but also that the large pores have survived (see Figure 6-5b). To prove the pore shrinkage hypothesis, however, even the largest pores must disappear after a certain time. Figure 6-13 of the appendix shows a BSE micrograph for alloy 1.5Fe1.9Si after an additional SSS+50h condition and confirms that no pores remain after 50 h of annealing at 560 °C.

6.5 Conclusions

The bendability of Al-Mg-Si-Fe crossover alloys is not necessarily impaired either by Fe-rich IMPs, or by adding Fe. Rather, it depends on the overall matrix composition and the processing conditions. In the latter context, the effect of pores on bendability is considered to be very important. The following conclusions can be drawn:

- Bendability can be retained within low-Si variants (0.8Fe1.1Si and 1.5Fe1.1Si) despite a large increase in Fe content. In contrast to the Si-corrected alloys (0.8Fe1.5Si and 1.5Fe1.9Si), the former feature a significantly softer matrix after pre-straining the material to 10%. When brittle second phases, such as Fe-rich IMPs, are present in the microstructure, high strength and strain hardening can have a negative effect. This phenomenon arises due to a critical stress level among the IMPs, which is reached earlier in high-strength and high strain-hardening materials, leading to earlier fracture of IMPs and consequent void formation. Damage to near-surface IMPs and the softening effect of developing porosity promote the formation of narrow shear bands that require less plastic deformation to form a crack.

- If annealing upon cold rolling is conducted above the solvus temperature of Mg_2Si and Si and this is followed by slow cooling, large remaining precipitates will leave pores behind while they dissolve. Such porosity in Al-Mg-Si-Fe crossover alloys significantly reduces bendability. Voids nucleated at IMPs and pre-existing pores together contribute to the formation of shear bands and thus to bend failure, which is more likely to occur at higher pore densities. To suppress pore formation, it is necessary to avoid excessive precipitation of coarse Mg_2Si and Si after high-temperature processing steps, such as cooling in a coil after hot-rolling or intermediate annealing treatments. In this study, applying rapid cooling conditions after the relevant process steps prevented pore formation and improved bendability.

- A long-term solution annealing treatment for 1 h at 560 °C can be applied to heal the microstructural damage induced by pores and/or voids and restore the bending capacity close to the pore-free condition. It may be concluded that this observed increase in bendability is caused solely by the reduction in pore density. While the average pore diameter increases, there is a significant decrease in their area fraction. Ostwald ripening is suggested as the dominant mechanism, resulting in the growth of large pores at the expense of small

ones, which eventually disappear. The reduction in area fraction, i.e. the shrinkage and collapse of pores, can be explained by the difference in chemical potential induced by different grain R and void r radii ($R > r$) and the diffusion of atoms between the void surface and the adjacent grain boundary interface.

In conclusion, this study provides a deep insight into the mechanisms affecting the bendability in Al-Mg-Si alloys heavily loaded with scrap-related elemental additions such as Fe and Si for different processing conditions.

6.6 Appendix VI

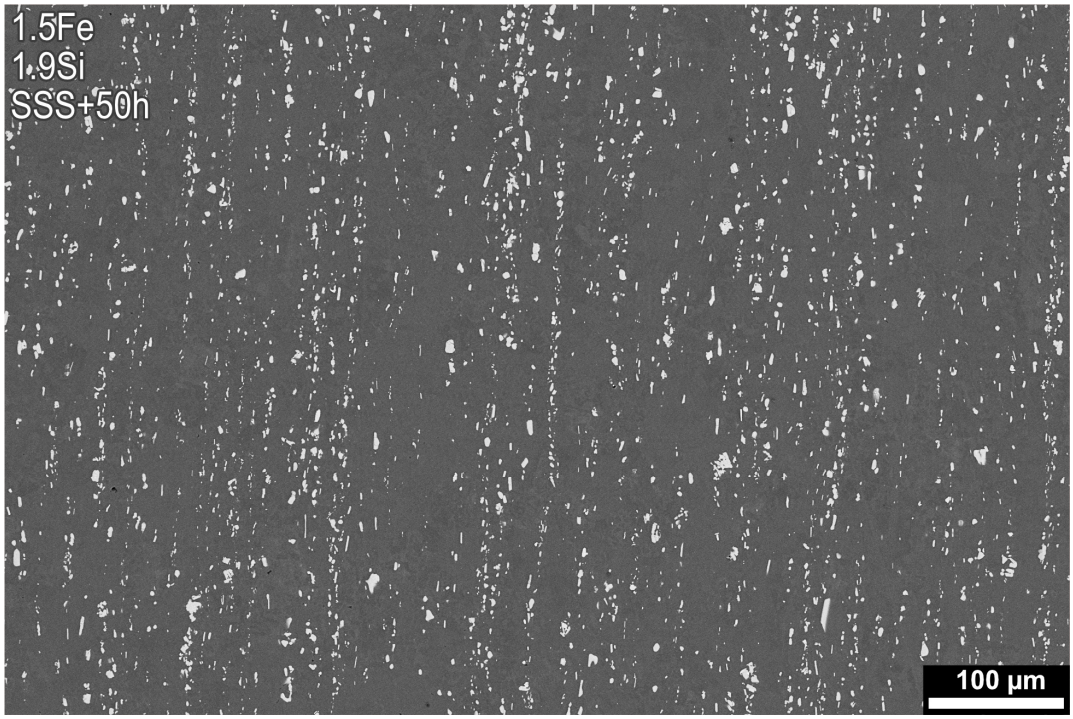

Figure 6-13: BSE micrograph for alloy 1.5Fe1.9Si after an additional SSS+50h condition (no pores remain after 50 h of annealing at 560 °C).

6.7 References

[1] R. Prillhofer, G. Rank, J. Berneder, H. Antrekowitsch, P.J. Uggowitzer, S. Pogatscher, Materials 7 (2014) 5047–5068.

[2] F. Ostermann, Anwendungstechnologie Aluminium, 3rd ed., Springer Vieweg, Berlin, 2014.

[3] S. Pogatscher, H. Antrekowitsch, H. Leitner, T. Ebner, P.J. Uggowitzer, Acta Materialia 59 (2011) 3352–3363.

[4] Y. Zi, L. Zeqin, D. Leyvraz, J. Banhart, Materialia 7 (2019) 100413.

[5] F. Grabner, B. Gruber, C. Schlögl, C. Chimani, Materials Science Forum 941 (2018) 1397–1403.

[6] R.A. Antunes, M.C.L. de Oliveira, Materials & Design 63 (2014) 247–256.

[7] L. Zhang, J. Gao, L.N.W. Damoah, D.G. Robertson, Mineral Processing and Extractive Metallurgy Review 33 (2012) 99–157.

[8] L.F. Mondolfo, Aluminum alloys: Structure and properties, Butterworth & Co (Publishers) Ltd, London, 1976.

[9] M. Lentz, G. Laptyeva, O. Engler, Journal of Alloys and Compounds 660 (2016) 276–288.

[10] O. Engler, J. Aegerter, D. Calmer, Materials Science and Engineering: A 775 (2020) 138965.

[11] L. Pan, K. Liu, F. Breton, X. -Grant Chen, J. of Materi Eng and Perform 25 (2016) 5201–5208.

[12] B. Trink, I. Weißensteiner, P.J. Uggowitzer, K. Strobel, A. Hofer-Roblyek, S. Pogatscher, Acta Materialia 257 (2023) 119160.

[13] B. Trink, I. Weißensteiner, P.J. Uggowitzer, K. Strobel, S. Pogatscher, Scripta Materialia 215 (2022) 114701.

[14] W. Muhammad, J. Kang, A.P. Brahme, U. Ali, J. Hirsch, H.-J. Brinkman, O. Engler, R.K. Mishra, K. Inal, Materials Science and Engineering: A 753 (2019) 179–191.

[15] J. Sarkar, T. Kutty, D. Wilkinson, J. Embury, D. Lloyd, Materials Science and Engineering: A 369 (2004) 258–266.

[16] J. Datsko, C.T. Yang, Journal of Engineering for Industry 82 (1960) 309–313.

[17] Z. Fan, X. Lei, L. Wang, X. Yang, R.E. Sanders, Materials Science and Engineering: A 730 (2018) 317–327.

[18] A. Davidkov, R.H. Petrov, V. Bliznuk, P. Ratchev, P. de Smet, B. Schepers, L. Kestens, KEM 465 (2011) 451–454.

[19] A. Davidkov, R.H. Petrov, P. de Smet, B. Schepers, L.A. Kestens, Materials Science and Engineering: A 528 (2011) 7068–7076.

[20] W.B. Lievers, A.K. Pilkey, D.J. Lloyd, Materials Science and Engineering: A 361 (2003) 312–320.

[21] S. Das, M. Heyen, R. Kamat, R. Hamerton, in: M. Oliver (Ed.), Light Metals 2018, Springer, Cham, 2018, pp. 325–331.

[22] L. Mattei, D. Daniel, G. Guiglionda, H. Klöcker, J. Driver, Materials Science and Engineering: A 559 (2013) 812–821.

[23] G. Lu, J. Wang, Y. Liu, C. Liu, Materials Science and Engineering: A 791 (2020) 139604.

[24] J. Hirsch, T. Al-Samman, Acta Materialia 61 (2013) 818–843.

[25] Z. Li, Z. Zhang, G. Zhou, P. Zhao, Z. Jia, W.J. Poole, Materials Science and Engineering: A 814 (2021) 141199.

[26] S. Ikawa, M. Asano, M. Kuroda, K. Yoshida, Materials Science and Engineering: A 528 (2011) 4050–4054.

[27] W.B. Lievers, A.K. Pilkey, M.J. Worswick, Mechanics of Materials 35 (2003) 661–674.

[28] A.L. Gurson, J. Eng. Mater. Technol 99 (1977) 2–15.

[29] V. Tvergaard, A. Needleman, Acta Metallurgica 32 (1984) 157–169.

[30] V. Tvergaard, Int J Fract 17 (1981) 389–407.

[31] D. Raabe, M. Sachtleber, H. Weiland, G. Scheele, Z. Zhao, Acta Materialia 51 (2003) 1539–1560.

[32] M.T. Ma, J.P. Zhang, J. Zhou, H.Z. Lu, Materials Science Forum 913 (2018) 18–29.

[33] J. Hirsch, Transactions of Nonferrous Metals Society of China 24 (2014) 1995–2002.

[34] F. Schmid, L. Stemper, T. Ebner, W. Leitner, S. Pogatscher, in: Proceedings of the EMC 2019 639-652.

[35] R. Neuhaus, M. Borsutzki, Materials Testing 55 (2013) 654–659.

[36] General Motors, Three-Point Bend Test for Hemming Performance Evaluation, 2018.

[37] R. Hielscher, H. Schaeben, J Appl Cryst 41 (2008) 1024–1037.

[38] E. Aryshenskii, J. Hirsch, S. Konovalov, Metals 11 (2021) 507.

[39] F.J. Humphreys, Acta Metallurgica 25 (1977) 1323–1344.

[40] O. Engler, J. Hirsch, Materials Science and Engineering: A 336 (2002) 249–262.

[41] A. Bjurenstedt, E. Ghassemali, S. Seifeddine, A.K. Dahle, Materials Science and Engineering: A 756 (2019) 502–507.

[42] D. Broek, Engineering Fracture Mechanics 5 (1973) 55–66.

[43] P. Castany, F. Diologent, A. Rossoll, J.-F. Despois, C. Bezençon, A. Mortensen, Materials Science and Engineering: A 559 (2013) 558–565.

[44] J. Sarkar, T. Kutty, K.T. Conlon, D.S. Wilkinson, J.D. Embury, D.J. Lloyd, Materials Science and Engineering: A 316 (2001) 52–59.

[45] W.J. Poole, X. Wang, J.D. Embury, D.J. Lloyd, Materials Science and Engineering: A 755 (2019) 307–317.

[46] P. Aster, P. Dumitraschkewitz, P.J. Uggowitzer, F. Schmid, G. Falkinger, K. Strobel, P. Kutlesa, M. Tkadletz, S. Pogatscher, Materialia 32 (2023) 101964.

[47] M. Werinos, H. Antrekowitsch, T. Ebner, R. Prillhofer, P.J. Uggowitzer, S. Pogatscher, Materials & Design 107 (2016) 257–268.

[48] Y. Wang, P.B. Prangnell, Materials Characterization 134 (2017) 84–95.

[49] J. Bajer, S. Zaunschirm, B. Plank, M. Šlapáková, L. Bajtošová, M. Cieslar, J. Kastner, Crystals 12 (2022) 607.

[50] F. Czerwinski, Materials 13 (2020) 3441.

[51] J. Du, M. Guo, J. Zhi, X. Chen, L. Zhuang, L.A. Kestens, Materials Chemistry and Physics (2024) 129471.

[52] W. Lievers, Effect of void damage and shear band development on the bendability of AA6111 automotive aluminum alloy sheet, Carleton University Ottawa, Ontario, 2001.

[53] J.G. Cowie, F.R. Tuler, Materials Science and Engineering 95 (1987) 93–99.

[54] H. Toda, T. Hidaka, M. Kobayashi, K. Uesugi, A. Takeuchi, K. Horikawa, Acta Materialia 57 (2009) 2277–2290.

[55] H. Toda, K. Minami, K. Koyama, K. Ichitani, M. Kobayashi, K. Uesugi, Y. Suzuki, Acta Materialia 57 (2009) 4391–4403.

[56] J. Sun, J. of Materi Eng and Perform 11 (2002) 322–331.

[57] J.M. Howe, Interfaces in materials: Atomic structure, termodynamics and kinetics of solid-vapor, solid-liquid and solid-solid interfaces, J. Wiley, New York, 1997.

[58] I.F. Bainbridge, J.A. Taylor, Metall Mater Trans A 44 (2013) 3901–3909.

7 SUMMARY AND OUTLOOK

In this work novel highly Fe-tolerant Al-Mg-Si alloys are introduced. By applying a crossover approach, the microstructure controlling effect of primary Fe-rich IMPs during thermomechanical processing seen in foil materials (i.e. 8xxx alloys) is combined with the age hardening capability of the 6xxx series. The effects of adding high amounts of Fe and Mn to alloy EN-AW 6016 were examined, while the Si consumed in primary phases was partly adjusted to maintain age-hardening potential.

The effect of microstructure control is described as follows: By applying thermomechanical treatment, the as-cast structure of brittle Fe-rich primary phases, which are normally responsible for early material failure, were modified to achieve finely dispersed particles of about 1 to 2 µm in diameter. The high area fraction of morphologically transformed IMPs resulted in significant grain refinement and uniform texture, which can be attributed to an enhanced nucleation rate during recrystallization because of the effect of particle stimulated nucleation. In the vicinity of fragmented IMPs, an increased dislocation density is formed during rolling, creating favorable sites for the formation of new recrystallization nuclei. Even coarse IMPs resulting from slow solidification rates typically applied during direct chill casting can be tuned in this manner, making this strategy extremely interesting for industrial mass production.

This improvements in microstructure compared to alloy 6016 resulted in unique mechanical properties: In addition to higher strengths, it was possible to significantly increase strain hardening, while keeping age-hardening potential and total elongation comparable to those seen in commercial alloy 6016. During deformation, additional geometrically necessary dislocations are generated around the morphologically modified Fe-rich IMPs, which are the source of the improved work-hardening capability. The high ductility of the Al-Mg-Si-Fe crossover alloys can be attributed to three key factors: The small size and rounded appearance of the IMPs, the small matrix grain size, and the GND forest surrounding the particles. This offers significant potential for broadening the property profile of Al-Mg-Si alloys to include greater work hardening capability and reduction of alloy complexity in the automotive sector, which also aids recycling by design.

As the design approach was to develop a wrought alloy dedicated to automotive sheet, bendability had to be evaluated, as this is an important forming attribute in this field of industry. The investigations of this thesis offered detailed insights into the effects of the type and density of intermetallic particles, the overall strength of the alloy, its strain hardening and the development of porosity due to particle cracking and the dissolution of phases leading to Kirkendall pores. It has been shown that a high Fe-content is not necessarily considered detrimental for bendability in Al-Mg-Si-Fe crossover alloys, if the alloys matrix is soft. Dislocation pile-up stresses at IMPs will reach a critical value earlier in alloys featuring high strength and strain hardening, resulting in particle

fracture and void formation. Voids formed either by particle fracture or by the dissolution of other phases (Kirkendall pores) promote the formation of narrow shear bands, leading to premature bending failure.

The concept of microstructure control using Fe-rich IMPs has also been successfully demonstrated on an industrial scale. Since Al-Mg-Si-Fe crossover alloys have a very weak texture, the determination of plastic anisotropy could provide further useful insight into material behavior. Initial tests have been carried out on industrially produced samples and are shown in the Appendix.

Despite the promising results already obtained during the course of this thesis, there are still many aspects regarding formability that require further investigation and detailed examination. The high strain hardenability of some of the alloys presented here reaches values far beyond those of Al-Mg (5xxx) alloys. Therefore, evaluation of stretch formability is of great interest. Furthermore, fracture toughness analyses are reasonable since a microstructure with a very high proportion of morphologically optimized IMPs could contribute to crack deflection and thus might have a beneficial effect. Overall, the alloying concept presented raises questions about the use of other "impure" alloy compositions for their use in wrought alloys. After all, the basic principles of microstructure control demonstrated in this study are not limited to AlFeSi-phases.

8 APPENDIX

Table 8-1: Reference to the use of AI-based tools

Subject	Share of KI [%]	Tool / Version	Comment
Improving readability	35	DeepL	n.a.
Improving readability	5	ChatGPT / V4	n.a.